



UNIVERSITÀ
DEGLI STUDI
FIRENZE

Facoltà di Scienze Matematiche Fisiche e Naturali
Corso di Laurea Magistrale in Scienze Fisiche e Astrofisiche

TESI DI LAUREA MAGISTRALE
19 APRILE 2018

**Sea ice underside three-dimensional
topography and draft measurements with
an upward-looking multibeam sonar
mounted on a remotely operated vehicle**

Relatore:

Prof. Francesco Marin

Candidato:

Veronica Coppolaro

Correlatore:

Dott. Christian Katlein

ANNO ACCADEMICO 2016/2017

Contents

1	Abstract	3
2	Introduction	5
2.1	Short overview on sea ice	5
2.2	Sea ice in the Arctic and its importance in the climate system . .	7
2.3	Sea ice thickness measurement methods and modeling	13
2.4	Thesis objectives	15
2.5	Thesis structure outline	16
3	Theoretical background	19
3.1	Sea ice vertical terminology	19
3.2	Basics of hydroacoustics	20
3.2.1	Acoustic waves in the Arctic Ocean	20
3.2.2	Introduction to sonar and principles of multibeam echosounder . . .	27
3.3	Electromagnetic induction sounding	33
3.4	Snow depth measurements	38
3.5	Draft calculation from thickness measurements	39
3.6	Modeling sea ice growth	40
3.6.1	Sea ice formation and growth processes	40
3.6.2	Freezing-degree days model	43
4	Methods	53
4.1	Data collection	53
4.1.1	Area of study	53
4.1.2	Instrumentation and survey logistics	54
4.1.3	The remotely operated vehicle	58
4.1.4	Multibeam sonar specifics	59
4.1.5	Navigation and multibeam sonar dedicated software	61
4.2	Sea ice draft retrieval from multibeam sonar: workflow implementation	64
4.2.1	Processing workflow	66
4.2.2	Use of the tide tool as an escamotage for draft measurements	70
4.3	Multibeam sonar spatial resolution calculation	71
4.4	Sea ice draft and snow depth measurements from GEM-2 datasets	74
5	Results	77
5.1	Multibeam sonar resolution	77
5.1.1	Across and along-track resolution	77

5.1.2	Vertical resolution and ice thickness uncertainty	78
5.1.3	Maximising the multibeam sonar resolution	79
5.1.4	Trade-offs	81
5.1.5	Pulse repetition frequency limitations	83
5.2	Sea ice underside three-dimensional topographic maps	85
5.3	Sea ice draft distribution maps	89
5.3.1	Sea ice draft distribution maps from multibeam sonar	90
5.3.2	Sea ice draft distribution maps from GEM-2	92
5.4	Histograms of sea ice draft distribution	98
5.4.1	Histograms of MBS sea ice draft datasets	99
5.4.2	Histograms of GEM-2 sea ice draft datasets	101
5.5	Comparison of the two methods for sea ice draft measurements . .	103
5.6	Snow depth distribution analysis	105
5.7	Sea ice growth model results	109
6	Discussion	117
6.1	Considerations regarding the multibeam sonar resolution	117
6.2	Analysis of the sea ice underside topographic maps	118
6.3	Comparison between MBS and GEM-2 sea ice draft distributions	120
6.4	Sea ice growth model validation	125
6.5	Operational recommendations:	
	Advancements in approach and methods	127
7	Conclusions and outlook	129
	Bibliography	132
	Acknowledgements	143
	Appendix A DT101 Specification sheet	147
	Appendix B CARIS Hips brief manual for sea ice draft measurements with DT101	153
	Appendix C Snow depth-sea ice thickness regression plots	171

Chapter 1

Abstract

Sea ice plays a major role in the global climate as it represents the interface between the ocean and the atmosphere and thus is of great importance for the energy budget of the whole planet. Climate change has caused a significant rise in air temperature during the last decades that has led to a rapid sea ice decline. Until now, sea ice retreat and thinning are underestimated and poorly represented by climate models as many processes are not well understood yet. Further observations of sea ice thickness and extent are required in order to understand the key processes that lead to sea ice transformations in both space and time. In this thesis the sea ice thickness and underside topography of three different areas northeast of the Svalbard archipelago are investigated during the freeze-up period of September and October 2016. In this pilot project, sea ice draft measurements are conducted using an upward-looking multibeam sonar mounted on a remotely operated vehicle for under ice surveys. The data collected are processed using the hydrographic processing system “CARIS Hips”. A new processing workflow has been developed to measure sea ice draft from underneath the ice. It allows the analysis of the data collected by the upward-looking sonar and the pressure sensor, together with many other sensors mounted on the underwater vehicle, in order to directly compute sea ice draft. Sea ice thickness can be calculated from draft measurements assuming isostatic equilibrium. Three-dimensional topographic images of the underside of the sea ice are produced and correlated with the respective sea ice thickness maps. The spatial and vertical resolution of the multibeam sonar is also calculated. Moreover, multibeam sonar derived sea ice thickness datasets are compared to sea ice thickness data collected by an electromagnetic induction sounding

device during the same surveys. Finally, the “Freezing-degree days” model is used to assess sea ice thermodynamic growth of the data collected during the field campaign. Snow cover is taken into account in the model thanks to snow depth measurements conducted on the areas with a Magna Probe. It is found that the two instruments for sea ice thickness measurements are in good agreement and have the same vertical resolution. However, the multibeam sonar is found to have a better lateral resolution and to be more accurate than the electromagnetic device when measuring sea ice ridges. The assessment of sea ice thermodynamic growth is hindered by the high spatial variability of the three areas of this campaign. Nonetheless the model predictions are found to be consistent with the formation from open water of a few centimeters of new ice during a survey period of four weeks. This thesis also suggests some improvements to the navigation of the underwater vehicle for sea ice draft measurement purposes and to the multibeam sonar renavigation script. The results of this thesis prove that the new processing workflow implemented in CARIS Hips allows for a reliable, efficient, and high resolution retrieval of sea ice draft measurements collected by an upward-looking sonar mounted on a remotely operated vehicle. The methods presented in this thesis can be adopted for a future year-round spatial and temporal study of sea ice thickness and underside morphology, necessary to fill the existing data gap during winter time in the Arctic. The use of the multibeam sonar together with the many interdisciplinary sensors mounted on the remotely operated vehicle empowers a complete overview of the sea ice underside environment and contributes to the improvement of climate models.

Chapter 2

Introduction

2.1 Short overview on sea ice

Sea ice is the floating ice that forms from frozen ocean water. Its content in salt differentiates it from fresh water ice, like icebergs and glaciers.

Sea ice forms both in the Arctic and the Antarctic during the local winter time when the ocean surface cools down to $-1.8\text{ }^{\circ}\text{C}$ ([97]). Sea ice covers 15% of the oceans of the globe during some parts of the year ([92]): about 25 million square kilometers of the Earth, an area larger than double the size of Canada.

Sea ice can show a wide variety of features, thickness, and extent (see for example figure 2.1). This thesis will focus on the study of Arctic sea ice thickness and underside morphology.



Figure 2.1: View of sea ice formations northeast of Svalbard

In the northern hemisphere the sea ice extent reaches its maximum

in March, close to the end of the polar winter in this region. Although it is primarily confined in the Arctic Ocean, Arctic sea ice has been known to form as far south as 38° N in Bohai Bay, China, ([3]) the same latitude as Palermo, Italy. Arctic sea ice extent averaged for the entire month of March 2016 was 14.43 million square kilometers (see figure 2.2). In winter most of the Arctic is generally covered by 2 to 3 m thick sea ice, but it can reach 4 to 5 m in some Arctic regions ([3]). With the approach of the summer months temperature rises and the sea ice starts to melt during the so-called “melting season”. This season results in a maximum sea ice melt from the middle of July to the middle of September, when the summer sea ice extent in the Arctic reaches its minimum ([81]). Arctic sea ice extent during September 2016 averaged 4.72 million square kilometers (see figure 2.2), while the sea ice thickness mean value was around 1.8 m ([16]).

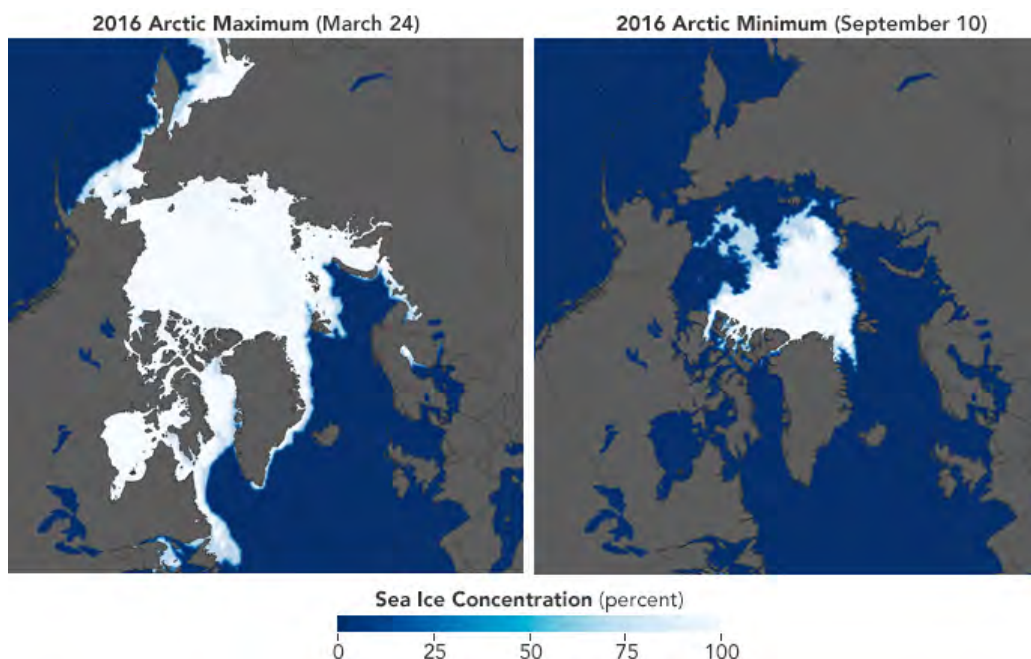


Figure 2.2: View of Arctic sea ice maximum and minimum extent in 2016. NASA Earth Observatory maps by Joshua Stevens, based on AMSR2-E data from NSIDC.

Sea ice thickness in the Arctic varies depending on the season and on many other factors, like the age of the ice and the dynamical phenomena that it experiences ([92]).

Referring to a classification based on the age of sea ice two main cate-

gories can be identified: multi-year ice (MYI) and first-year ice (FYI) ([103]).

Multi-year ice indicates sea ice that has survived at least one melt season: this old ice did not melt completely during the preceding summer and generally grows thicker every winter.

First-year ice is instead the ice that forms during one winter and melts completely every summer. The lower thickness makes FYI more prone to complete melting during summer and as a result of this brief melt cycle first year sea ice grows generally thinner than old ice.

Thermodynamics drives sea ice growth and ablation. An important process linked to ice melt is melt pond formation. During summer melt ponds form on the surface of the sea ice therefore sea ice thickness decreases by absorbing a higher amount of solar radiation ([91]). FYI can decrease to few centimeters or melt completely and be replaced by open water.

On the other hand, events linked to sea ice dynamics can create more rapid changes in sea ice thickness than thermodynamic driven ones. Divergent or convergent movements between ice floes create leads and pressure ridges. The first ones are long fractures of open water between ice floes, while ridges are ice conformations that protrude from the ice floe surface both in the water and above the ice, and can reach a maximum thickness up to 30 m ([31]).

2.2 Sea ice in the Arctic and its importance in the climate system

Sea ice plays a major role in the Arctic. It represents the ideal habitat for lots of local species; it breaks the waves coming from the Atlantic Ocean; it reflects part of the solar radiation keeping the water temperature cool below the ice and influencing the global climate via the under-ice oceanic currents ([62], [89]). These and many other features make the presence of sea ice necessary to preserve the physical and biological stability of polar regions and of the whole global climate ([3]). Hence why the drastic changes that sea ice is experiencing during the last few decades are of great concern.

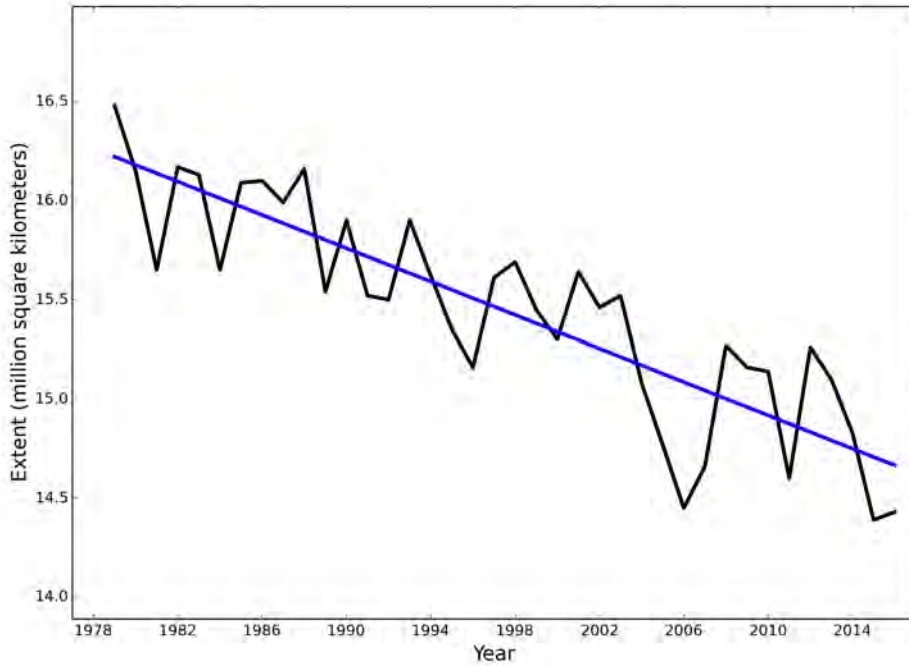


Figure 2.3: Average March Arctic sea ice extent for 1979 to 2016 shows a decline of 2.7% per decade (NSIDC)

The Arctic is indeed one of the regions on Earth that has been warming up at the highest rate during the last decades, experiencing an air temperature change as extreme as twice as fast as the global average ([3]). This characteristic of both poles to experience more drastic temperature changes than the rest of the planet is known as “polar amplification” ([79]).

One of the most striking consequences of this ongoing warming process is the decline of sea ice cover extent and thickness, that have both decreased drastically in the last 50 years.

During the last three decades both sea ice maximum and minimum extent experienced a drastic decrease. Figures 2.3 and 2.4 show respectively the maximum sea ice extent trend in March and the minimum in September, between 1978 and 2016. The decline per decade is as high as 2.7% and 13.3% respectively ([3]). The year 2012 marked a record September minimum since 1979, as the graph in figure 2.5 shows ([3]). Sea ice thickness is also declining. In 1999 Rothrock and collaborators used sea ice thickness data collected during submarine cruises. They found that the submerged part of the sea ice decreased

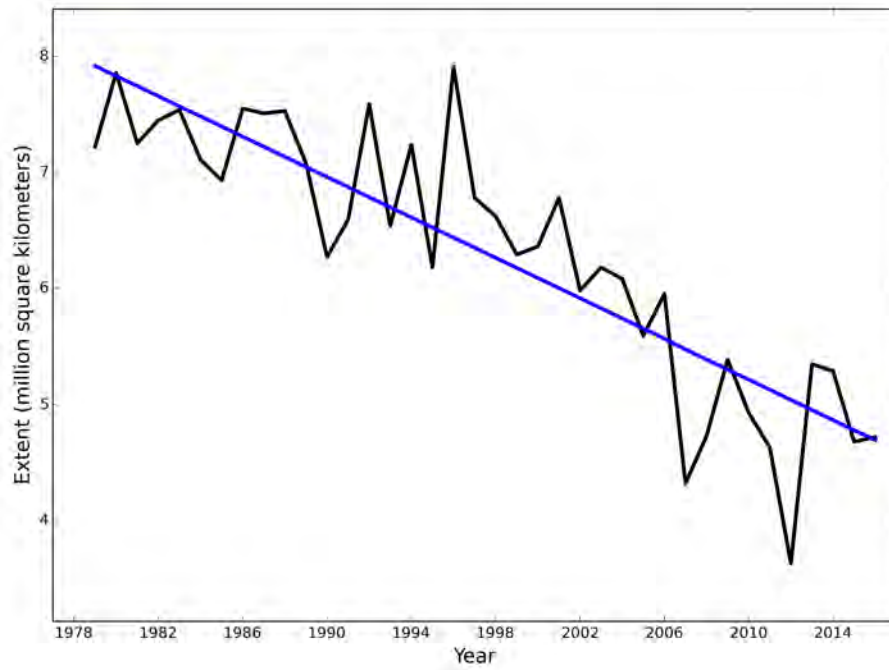


Figure 2.4: Average September Arctic sea ice extent for 1979 to 2016 shows a decline of 13.3% per decade (NSIDC)

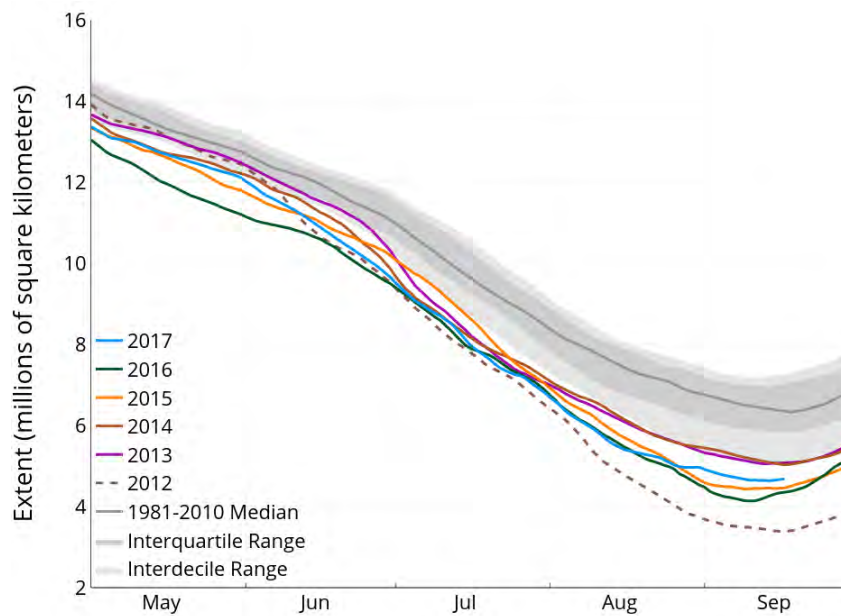


Figure 2.5: Minimum Arctic sea ice extent (NSIDC)

by about 1.3 meters between the 1950s and the 1990s ([75]).

A new study published ten years later shows how the Arctic mean winter sea ice thickness declined from 3.64 meters in 1980 to 1.89 meters in 2008: a decline of 1.75 meters in only 20 years ([46]).

Also, while the mean thickness for summer ice in the Arctic during the 1960s used to be around 3 m, during the last 5 years it has decreased to a mean value of less than 1 m ([3]).

Another rapid change that sea ice is experiencing during the last decades is the variation in relative abundance of MYI and FYI ([47]). As discussed in [88], for example, because of the new dynamics and environmental changes that are taking place in the Arctic the net thinning of thick ice is usually much larger than for thin ice, for any given warming; this is because thin ice gains its summer ice loss again during the following winter as it grows faster than thick ice.

As a consequence, MYI in the Arctic does not predominate on FYI anymore, and FYI can now also be found to be thicker than MYI. This process contributes to the ongoing decrease of sea-ice thickness and extent ([88]).

According to scientists the current sea ice decrease rate could lead to an ice-free Arctic summer in less than half a century ([95]). This will lead to a habitat loss for a big part of the Arctic fauna, will likely lead to a more rapid coastal erosion due to wind-driven waves and to a potential general global weather and ocean circulation change ([10] and [25]).

An example of the important role of sea ice and the strong impact that changes in its conditions have on the Arctic and the entire globe follows here.

The Arctic used to be characterised by the prevalence of old, multi-year sea ice. As already mentioned, the current amount of multi-year ice has decreased drastically, especially during the last two decades ([3]). First-year tends now to replace multi-year ice changing the under-ice environment because of different physical and optical properties of the two ice types ([88]).

FYI is generally thinner and in summer it is covered in wider and more shallow melt ponds than MYI ([68]). Melt ponds create areas



Figure 2.6: Melt ponds formations northeast of Svalbard

characterised by lower albedo compared to bare ice, causing less light reflection towards the atmosphere and more radiation transmission to the ice and the water below it. A high concentration of melt ponds and the fact that FYI is more vulnerable to summer melt as less energy is needed to melt it cause a higher melting rate for the thin sea ice and a higher amount of solar heat absorbed by the sea water below it ([69] and [65]). A summer melt pond distribution is shown in figure 2.6. Thin ice also transmits more light to the water underneath than thick ice. The amount of light that penetrates the sea ice changes the under-ice biological habitat, for example by increasing the amount of algae that live attached to the sea ice bottom (figure 2.7). An algal bloom provides for more nutrition for the animals that feed on them, including pelagic and benthic species ([84] and [44]). In the long run declines in sea ice have been associated with a major ecosystem shift ([37]), loss of habitat and negative impacts on sea ice associated organisms ([27]).

Light effects on algae influence the deep water environment as well. Dead algae represent an important source of food for benthic microorganisms. These decompose the dead algae that reach the bottom of the ocean while consuming oxygen, changing considerably the chemistry composition of the deep sea under sea ice ([58]).

Moreover, sea ice affects and is affected by the movements of ocean water. One of the consequences of sea ice thinning is that it is more subject to wind and currents that can move the sea ice and transport it around the Arctic ([48]). Moreover, changes in Arctic currents and in the mixing of the water layers make the Arctic ocean more and more similar to the Atlantic Ocean, leading to a progressive process called “Atlantification” ([72]).



Figure 2.7: **Algae detached from the underside of the sea ice northeast of Svalbard**

Sea ice is also a main driver of the oceanic global circulation. Two main water layers can be found under the Arctic sea ice: the Polar water and the Atlantic water. The Polar water is found directly under the ice and it is composed of fresh and cold water; the Atlantic water lays under the layer of Polar water and it is warm and more salty. When sea ice forms, it releases most of the salt so that the water under the sea ice that receives it has a higher concentration of salt compared to the surroundings. As salt water is more dense than fresh water, it tends to sink. Once the cold, dense Polar water reaches the bottom, it moves towards the equator, while pushing the warm Atlantic water towards the poles. This circulation is called the thermohaline or “conveyor-belt” circulation and it streams around the globe. Changes in the amount of sea ice can then affect the whole

global climate ([92], [13]).

Changes in sea ice extent and thickness also affect communities living and working in polar regions. Arctic native people often depend on the presence of sea ice so that its retreat poses a set of new challenges to their life style ([62]). On the other hand, sea ice melting would lead to the opening of new shipping routes in the Arctic and fishing opportunities ([39]). This may affect the global maritime traffic, with possible negative consequences on the environment.

The impact of climate change on the Arctic poses great challenges to this delicate environment; a complex interplay between atmosphere, ocean, and land depends on the presence of sea ice. For these reasons studying sea ice is fundamental and an interdisciplinary study is required to thoroughly understand on a wider scale the extreme changes that are taking place in the polar regions and are affecting the Earth's climate system ([26]).

2.3 Sea ice thickness measurement methods and modeling

Given the role of sea ice both regionally and on a global scale it is important to model and predict sea ice changes.

Modeling sea ice has lots of applications in numerous fields, from climate change to marine navigation, to safety of working on the ice. One of the most important features to predict is sea ice thickness as a result of the influence that it has on many other parameters, such as light transmittance, temperature, ocean circulation, primary productivity and biomass. A study of sea ice thickness is therefore of high interest and interdisciplinary use.

Observations based on satellite data from 1979 to 2013 showed that the Arctic-wide sea ice cover extent is declining at -14% per decade ([87]). This trend is more rapid than what any climate models of the Intergovernmental Panel for Climate Change (IPCC) has predicted ([92]).

The disagreement between models and observations demonstrate the actual knowledge deficiencies of the processes experienced by sea ice.

For a better understanding of sea ice dynamics and thermodynamic processes and in order to be able to improve predictive models of its evolution a more detailed investigation of sea ice physics and its properties is necessary.

In particular, whilst sea ice extent has been monitored for years by satellites and represents now a well known parameter, sea ice thickness is instead still poorly documented because it is more challenging to measure ([3]). Additional measurements of sea ice thickness must be collected to make up for this deficiency applying one of the different techniques available.

Ice drilling is the oldest technique used to measure ice thickness. This direct method is the most accurate of all the methods, but it is time consuming and it is also limited to the local point measurements of the cores. This restriction to point-like measurements does not allow for a generalization of the measures to the surrounding area; the values obtained by drilling cannot represent an area bigger than the sampled one, due to the high spatial variability of sea ice ([92]).

Upward-looking sonar (ULS) can be mounted on oceanographic moorings to measure sea ice thickness ([63]). This technique provides long time series of measurements, but it is restricted to the study of the single location where the sonar is attached, a similar to the ice core drilling one ([92]). ULS have also been mounted on submarines to collect sea ice vertical profiles over large areas of the Arctic Ocean for several decades ([98]). Although the spatial footprint is relatively small, such observations are limited by cost and vehicle availability.

On the other end of the scale, satellites measurements have been used for more than 30 years in order to regularly monitor polar regions and retrieve sea ice extent measurements ([23]). They can also be used to measure sea ice thickness with laser and radar altimeters ([93]). This method is very efficient, as it covers large regions in a small amount of time and measurements are continuously repeated without any need for field work or dedicated campaigns. However satellite footprints are wide compared to ground based instruments, and the respective algo-

rithms were just recently developed, causing various reliability issues.

Measuring sea ice thickness using ULS and satellites is nevertheless an indirect method of measure: ULS measure the submerged part of the ice, while lasers and radars the ice elevation from the sea surface. To retrieve sea ice total thickness an analytical method based on the isostasy principle must be applied. Several assumptions for snow thickness and density are assumed in this method and introduce additional uncertainties to satellite altimetry. Other limitations are the fact that satellites cannot cover the pole regions and that rely on the presence of open water as a reference for the model.

Midway between the large scale satellites measurements and the local point ice drilling measurements stand the electromagnetic induction sounding (EMI) [70]) and the multibeam sonar system (MBS). Both techniques for sea ice thickness measurements will be explained in more detail in their dedicated sections (3.3 and 3.2).

These two methods are both more efficient than ice coring and ULS, can cover large areas in few hours similar to satellite techniques, their accuracy can be tested during their operation, they have good spatial resolution, and are generally in good agreement with the results of the direct coring technique ([92], [71], [43]).

2.4 Thesis objectives

The main objective of this thesis is the implementation of a new processing workflow for measuring sea ice draft using an upward-looking multibeam sonar mounted on a remotely operated underwater vehicle. To achieve this, the data collected are handled using the hydrographic processing system “CARIS Hips”. This software has been developed for bathymetric surveys, so that in order to use it for measuring sea ice draft the standard workflow has to be modified.

Another objective is the production of three-dimensional topographic maps of the underside of the sea ice using the same multibeam sonar. The topographic maps will then be compared to real images of the morphology of the ice underside.

To test the processing workflow and assess the outcome of this method, the resultant sea ice draft datasets are compared to the measurements collected by an electromagnetic induction sounding device operated during the same surveys. This instrument measures sea ice thickness on the same area sampled by the multibeam sonar but it is operated above the ice.

Finally, using the values of sea ice draft retrieved with the newly implemented processing flow, sea ice thermodynamic growth is investigated using the “Freezing-degree days” model.

A secondary objective of this thesis work is to optimise the handling and collection of navigation data from the underwater vehicle, improve the multibeam sonar renavigation script, and determine the spatial and vertical resolution of the multibeam sonar used in this pilot project.

The results of this project aim to test the newly implemented workflow for sea ice draft retrieval, to assess potential changes that sea ice experiences during the growth season, and investigate the spatial variability of sea ice structures.

2.5 Thesis structure outline

This thesis focuses on the investigation of sea ice thickness measurements using an upward-looking multibeam profiling sonar that is mounted on a remotely operated underwater vehicle (ROV). The data have been collected during a pilot project that took place during the 101st expedition of the German research vessel “Polarstern” (figure 2.8) to the Central Arctic in late summer 2016 and are here processed and analyzed. This thesis is composed of the following chapters: Chapter “Theoretical background” introduces some background knowledge about the physics of sea ice; the devices involved in sea ice thickness measurements—multibeam sonar, electromagnetic device, and snow probe; the isostasy model for calculating ice thickness; and about sea ice growth models.



Figure 2.8: **View of the German research vessel “Polarstern” breaking through the sea ice around Svalbard.**

Chapter “Methods” contains a description of the multibeam sonar data collection and handling processes, including a section about the description of the newly implemented working flow.

The “Results” chapter is dedicated to the presentation of the results of this study. A calculation of the multibeam sonar resolution; sea ice underside three-dimensional topography; sea ice draft distribution maps obtained by the use of the multibeam sonar and by the electromagnetic device; histograms of sea ice draft and of snow depth distributions; a comparison of the two methods of sea ice thickness measurements and a final section focused on the thin sea ice growth “Freezing-degree days” model and aspects of other empirical models are discussed here. The “Discussion” chapter presents the analysis of the results of this thesis, including sea ice thickness distribution comparison between sampling methods and stations. A separate section is dedicated to sea ice growth model validation. The “Operational recommendations” section presents final suggestions and recommendations for future surveys.

Finally, the “Conclusions and outlook” chapter summarizes the thesis achievements and gives an outlook on the possible future of this study.

Chapter 3

Theoretical background

3.1 Sea ice vertical terminology

Sea ice can be divided in different vertical components that are defined depending on their position relative to the sea surface.

The ice slab is composed of three parts: sea ice draft h_d , sea ice freeboard h_f , and sea ice thickness H ; if snow is present, another layer h_s on top of the ice is introduced. A schematic representation of sea ice vertical components is shown in figure 3.1.

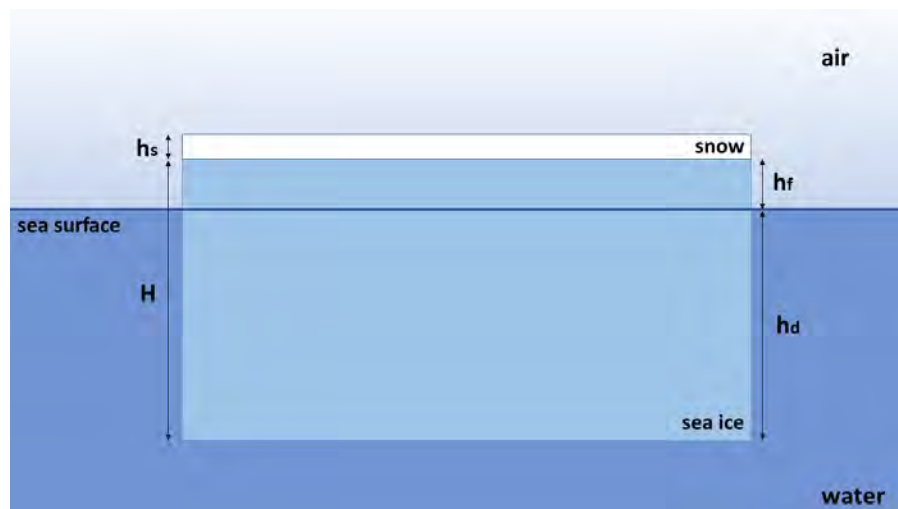


Figure 3.1: Schematic representation of sea ice vertical components

Draft is defined as the sea ice partial thickness measured from the underside of the ice up to the sea surface; freeboard is the part of the sea ice thickness between the sea surface and the upper surface of the ice; while total ice thickness is found by summing together the values for draft and freeboard.

It is worth stressing the importance of using the correct name for the different features. The reason is that in sea ice physics there are many different methods for ice thickness measurements. Some of them only collect draft or freeboard and retrieve the total thickness using mathematical models. However the common use of generally referring to h_d or h_f as “thickness” can generate confusion between the different sea ice components.

3.2 Basics of hydroacoustics

Hydroacoustics, or Underwater Acoustics, is the study of sound propagation in water. Underwater acoustic waves are widely used to transmit signals, detect and locate obstacles and targets, and to measure characteristics of objects ([56]).

Sonars are hydroacoustic based devices. The word sonar is an acronym that stands for “SOund Navigation And Ranging” and, as the name suggests, it is used to navigate and detect target distances underwater using sound.

In this pilot project a multibeam sonar is mounted on top of an ROV pointing towards the underside of the sea ice and the measurement results from three different areas are analysed in this work.

The following sections present therefore a brief description of sound properties in the Arctic Ocean and of sonar operation with particular focus on the multibeam sonar.

3.2.1 Acoustic waves in the Arctic Ocean

Sound propagation in sea water is affected by attenuation, perturbation, deformation, and noise (see [56]). A description of some of those properties that relate sea water and ice to underwater acoustics for sonar use in the Arctic will follow. Of particular interest for this study are: the variation of sound speed as a function of depth; the effects of sound reflection at the water-sea ice interface; and the refraction of sound during propagation in sea water.

To begin with, sound speed in the ocean depends mainly on temperature, pressure, and salinity. It increases with an increment in any of these variables, with a rule of thumb of: 1.4 m/s for every 1 psu increase in salinity; 4 m/s for every 1°C increase in temperature; and 34 m/s for every 2000 dbar increase in pressure ([104], [4]).

While pressure always increases with depth, salinity and temperature profiles depend on latitude, region, and season.

In the Arctic, salt concentration and temperature of the ocean upper layer are influenced by the presence of the sea ice cover ([21]), for example by the phenomenon of brine rejection during sea ice formation ([81], [92]). This process, together with other processes characteristic of the Arctic, such as river runoff, result in a salinity-stratified Arctic Ocean (figure 3.2).

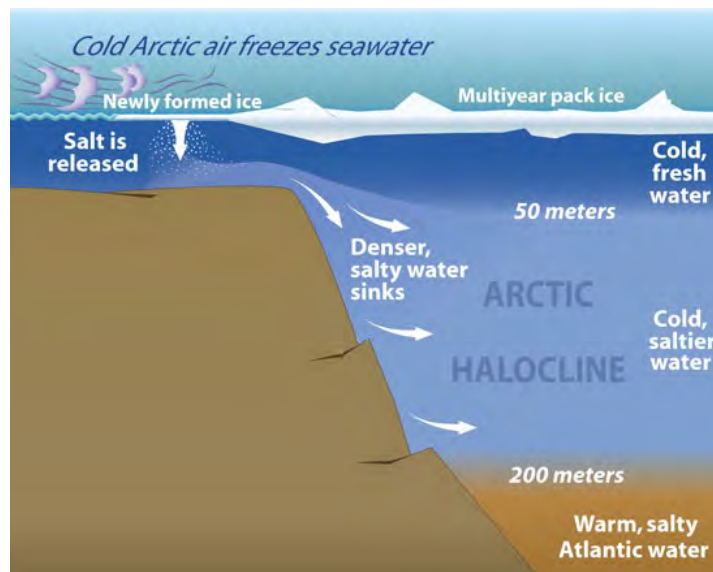


Figure 3.2: **Arctic Ocean stratification** Illustration by Jayne Doucette, Woods Hole Oceanographic Institution

The Arctic Ocean surface layer expands up to a depth of 50 m. It is characterised by cold water with homogeneous temperature around -1.8°C , the freezing temperature for sea water. The salinity of this layer is generally low compared to the mean ocean salinity, hence why this layer is referred to as “fresh water” in figure 3.2). However, regional and seasonal variability of sea ice cover can cause substantial fluctuations in local temperature and salinity ([21]).

Between 50 m and 200 m stands a layer of cold and dense water called

the “halocline”, where temperature is generally constant, while salinity increases with depth ([21], [76]).

The bottom layer of the Arctic Ocean is composed of Atlantic Water that is warmer and saltier than Arctic ocean water ([76], [67]).

The dependance of sound speed on temperature, salinity, and pressure is represented by the Arctic sound velocity profile as function of depth shown in figure 3.3.

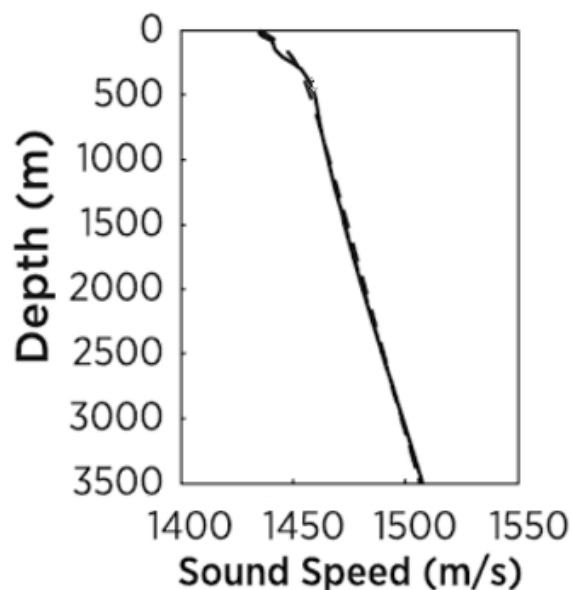


Figure 3.3: Sound speed depth profile in the Arctic. Image from [22]

In the first meters of water sound speed increases slowly due to an initial increasing pressure, while temperature and salinity stay almost constant. When reaching the halocline sound speed experiences a second increment due to a fast increase in salinity that adds to the action of pressure, while temperature does not generally vary. A final sound speed increase takes place in the Atlantic Water layer. Here salinity reaches a constant value while temperature only changes of a small amount (of the order of less than one degree in thousands of metres), hence sound velocity rapidly increases at greater depths due to its dependance on pressure (see [22]).

On account of what has just been stated, sound velocity corrections due to temperature, salinity, and pressure variation in water should be taken into account when using a sonar. This enables a correct mea-

surement of the time that takes to an echo to go from the sonar to the target and back, and therefore the correct calculation of the respective distance.

The maximum mean depth that the ROV reaches during the three surveys analysed in this study is 10 m, hence the multibeam sonar operates in the upper layer of the Arctic Ocean. As previously mentioned, this water layer is characterised by a constant value of salinity and temperature, while the pressure difference between 10 m and the surface is of only 1 atm. It is therefore expected to measure similar sound speed values for the three surveys, except for local variations of salinity and temperature.

Sound speed in sea water is generally calculated using collected CTD measurements in one of the models available (see for example [24] and [18]). CTD is a device that measures conductivity, temperature, and pressure of seawater.

In this work the values of sound speed between 0 and 10 m calculated using the onboard CTD measurements for the three surveys are found to differ by the 0.01%. This is due to the fact that the three survey areas are not too distant from each other, that the working depth of the multibeam sonar is the same, and that local variations of salinity and temperature are very similar. Hence in this work the sound speed in sea water will be set equal to the constant value of 1437 m/s that is calculated using the CTD measurements locally collected during the surveys.

Of particular interest for sea ice underside topography surveys is the effect of sound reflection at the water-sea ice interface. The Arctic Ocean surface during the freeze-up period is generally covered in sea ice, but leads of open water between ice sheets are not uncommon ([92]). Both the sea surface and the sea ice are reflective, scattering, and absorbing boundaries for sound waves. When sound waves reach a discontinuity between two media they are reflected and transmitted, depending on their relative characteristic specific acoustic impedance, Z_0 . This quantity represents the opposition of a medium to the flow of acoustic waves and it is defined as:

$$Z_0 = c \cdot \rho \tag{3.1}$$

where c represents the sound speed in the medium and ρ is the medium density.

The ratio between reflected and incident wave intensity is called “reflectance”, while the ratio between the transmitted and incident wave intensity is the “transmittance”.

The reflectance R and transmittance T for sound waves at the boundary interface between two media are given by formula 3.2. Both coefficients depend on the two media acoustic impedance difference, with a high difference resulting in a large reflected and a small transmitted intensity, as predicted by formula 3.3.

$$R = \frac{I_r}{I_i} = \left(\frac{\rho_2 c_2 \cos \theta_1 - \rho_1 c_1 \cos \theta_2}{\rho_2 c_2 \cos \theta_1 + \rho_1 c_1 \cos \theta_2} \right)^2 \quad (3.2)$$

$$R + T = 1 \quad (3.3)$$

Here I_r and I_i are the reflected and incident intensity of the acoustic wave, ρ_1 and ρ_2 are respectively the density of the initial and final media where the wave propagates, c_1 and c_2 the speed of sound in the two media, and θ_1 and θ_2 the incidence and refraction angle with respect to the normal to the two media boundary surface ([60], [14]).

In the simplified case of normal incidence and given the density values for sea water $\rho_w = 1025 \text{ kg/m}^3$, sea ice $\rho_i = 917 \text{ kg/m}^3$, and air at zero degrees temperature $\rho_a = 1.3 \text{ kg/m}^3$ ([2]) the resulting reflectance and transmittance for an acoustic wave going from water to air $R_{w/a}$ or from water to sea ice $R_{w/i}$ can be calculated. Examples of these values found in literature are:

$$R_{w/a} = 0.999 \quad T_{w/a} = 0.001 \quad (3.4)$$

$$R_{w/i} = 0.35 \quad T_{w/i} = 0.65 \quad (3.5)$$

where smooth level ice, that is the sea ice that has not been affected by deformation ([103]), has been used for the calculation of $R_{w/i}$, ([78], [85]). A large difference exists between the water-air and the

water-sea ice reflection coefficients, resulting in a large intensity reflected echo from open water. This is due to the higher impedance difference between water and air compared to that between water and sea ice ([34]). However, sea ice can be a strong reflector of sound, depending on its underside characteristics, as it is explained in the following ([102]).

Underwater acoustic interaction with ice is controlled by the underside topography ([32]).

The effectiveness of the ice-water interface in reflecting incoming acoustic energy has enabled the use of sonars to detect and map the underside of sea ice ([100]). The reflection of sound on the sea ice underside depends on its size, shape and thickness, signal frequency, angle of incidence, as well as the impedance of ice relative to that of water ([1], [56]). An appropriate description of sea ice to model sound reflection should take into account both physical, acoustic, and morphological properties of the ice and it is not part of this work (see for example [64]). In general, it is found that acoustic sound scattering is enhanced by the presence of deformed ice, while level ice creates echoes via specular reflection ([94], [17]).

Level-ice, that is the sea ice which has not been affected by deformation ([103]), shows a higher reflectance compared to ridges and rubble ice ([85], [94]). A reduction in level ice reflectivity has been observed due to the presence of the so called “skeletal layer”, the bottom part of the sea ice at the ice-water interface ([81]). This lower part of the sea ice features dendritic arms up to 10 mm that enhance the ice roughness and reduce the ice reflectance from 0.34 to 0.05 when compared to flat level ice ([35], [85]).

Scattering of acoustic waves on ridges is found to depend on the ridge draft, roughness (compared to the sound wavelength), and orientation ([15], [20]), with higher amplitude of scattered light for larger angles of incidence ([34], [61]) and increased surface roughness ([12]). Typical high scattered intensity from ridges facilitates their location using sonars. This is because deformed sea ice structures are generally non-normal to the incident wave and it would otherwise be difficult to locate them by only collecting their specular reflection ([56]).

Refraction also plays an important role in hydroacoustics. It causes the typical non-straight propagation of acoustic waves in sea water that affects sonar path measurements (see figure 3.4).

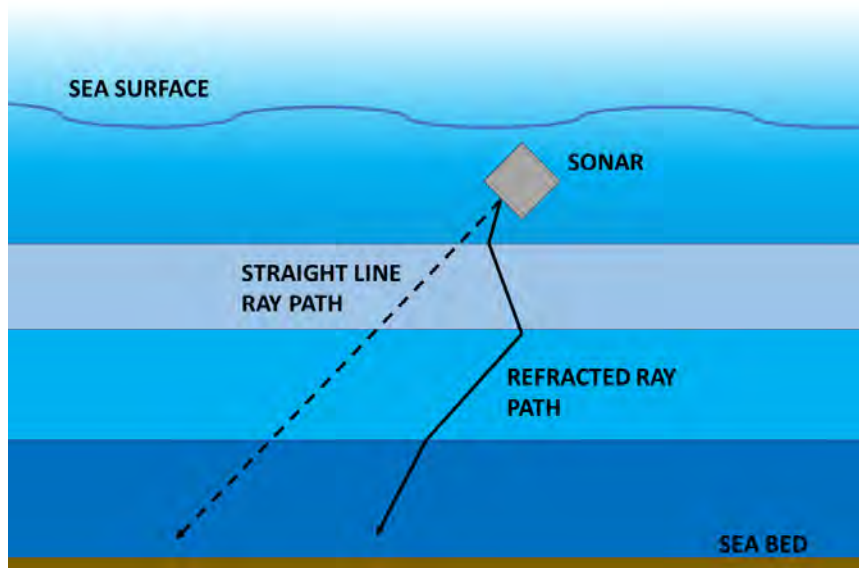


Figure 3.4: Schematic representation of acoustic wave refraction in the ocean

As previously mentioned, sound waves crossing the boundary between two layers of water characterised by different values of temperature, salinity, and pressure are affected by a variation in sound speed. Snell's law (formula 3.6) describes the relation between speed and angle of incidence for an acoustic wave entering a medium where sound propagates with a different speed ([61]). The result is that a variation in sound speed determines a change in the direction of propagation of the acoustic wave ([60]).

$$\frac{\sin\theta_1}{c_1} = \frac{\sin\theta_2}{c_2} \quad (3.6)$$

Here c_1 and c_2 are the sound speed, and θ_1 and θ_2 the incidence angles of the first and second medium respectively.

In this study refraction effects are not considered because of the homogeneity of the superficial water layer where the multibeam sonar operates. However, refraction should be taken into account for potential future studies using sonars working at greater depths, for example when mounted on an autonomous underwater vehicle (AUV), and in

general for more accurate distance measurements.

3.2.2 Introduction to sonar and principles of multibeam echosounder

There are two different operational modes for sonar: passive and active.

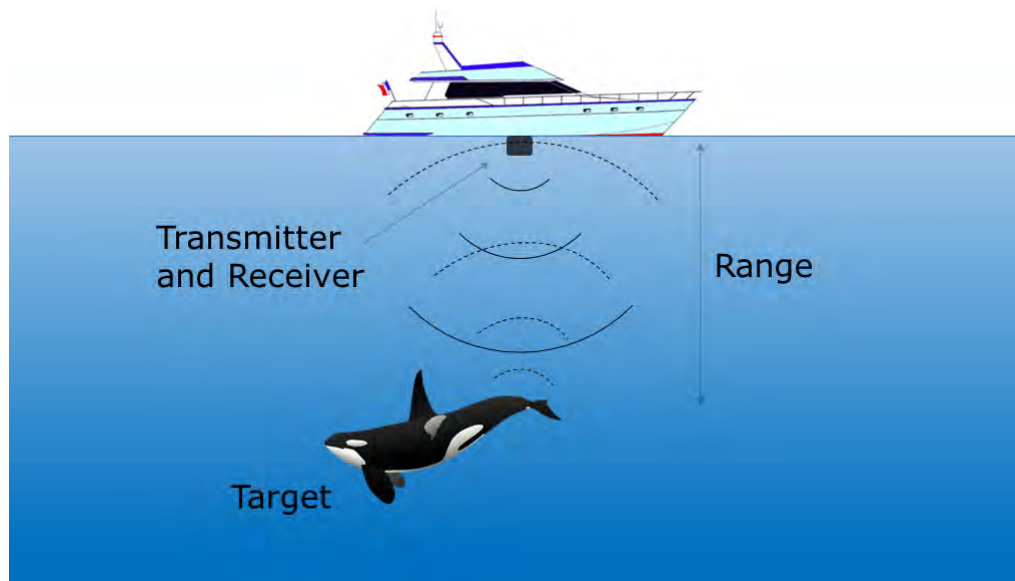


Figure 3.5: Active sonar

Passive sonar only receives an acoustic signal emitted by the target, while active sonar transmits and receives an acoustic signal that is therefore transmitted, reflected by a target, and transmitted back to the sonar (3.5).

The type of sonar used in this thesis is a multibeam sonar and it belongs to the category of active sonars whose basic principles of operation will be explained in the following.

An active sonar is composed of a transmitter, or projector, and a receiver. The projector creates and transmits an acoustic wave in the shape of a pulse of sound. This is generally created electronically and often called a “ping”. The receiver collects the echo that is produced by the reflection of the acoustic signal on the target. Finally, the signal is processed ([90]).

Once transmitted, a sound wave propagates in water travelling twice the distance between the sonar and the target, called “range”.

Range estimation is done by first measuring the time between the transmission of the signal towards the target and the reception of the respective echo, and then using the measured time to calculate the distance, as shown in formula 3.7:

$$R = \frac{c \cdot \tau}{2} \quad (3.7)$$

where R is the range, c is the local speed of sound, and τ is the time interval between signal transmission and echo collection.

The received signal contains information about both the target and the surrounding environment: sound is attenuated, deformed, and overlaid with noise along its path. An equation for energy conservation is commonly used to evaluate the sonar system performance and it is known as the “sonar equation” ([56]). Formula 3.8 and 3.9 describe logarithmic intensity in decibel respectively for noise and reverberation-limited conditions.

$$SL - 2TL + TS - NL + DI = DT \quad \text{noise-limited conditions} \quad (3.8)$$

$$SL - 2TL + TS - RL = DT \quad \text{reverberation-limited conditions} \quad (3.9)$$

Here SL is the source level; TL the transmission loss; TS the target strength; NL the noise level; DI the directivity index; DT the detection threshold; and RL the reverberation level.

In [56] and [57] an extensive description of each coefficient of the sonar equation can be found that is here reduced for brevity’s sake.

The source level for an active sonar is determined by the maximum intensity of the signal transmitted by the projector. The target reflects a replica of the transmitted signal and the echo level is proportional to the transmitted source level.

The transmission loss is taken into account twice in the equation because the acoustic waves travels back and forth between the sonar and the target. TL is mainly due to acoustic wave geometrical spreading

and to attenuation. Attenuation is caused by sea water absorption that limits the range at high frequency, and scattering loss linked to the presence of non-targets along the path, such as air bubbles and fish.

TS depends on the shape and size of the target, on the signal wavelength, and the angle of incidence.

NL consists of self noise and background noise. Self noise is the noise generated from the sonar reception platform, such as internal sonar noise due to the electronics. In this study the main source of self noise is the flow noise caused by the vehicle speed, typical for a sonar mounted on a ROV ([19]). Background noise includes noise due to oceanic, shipping, and animal sources.

In many applications sound is not transmitted homogeneously towards the target. Instead, narrow beams are used to increase sound intensity in a certain direction, as it is the case for this study. DI is the parameter that accounts for the directionality of the transducer in sonar performance studies by describing the spatial distribution of the transmitted intensity.

A signal threshold for detection is set in order to maximise the probability of receiving an echo from the target, while minimising at the same time potential misinterpretations of noise as a signal.

Finally, reverberation is another important factor that has to be considered in case of a strong presence of unwanted echoes, such as those created by sound scattering at the water surface and the sea ice underside. In ([63]) it is found that ridges create long reverberation echoes compared to level ice.

The sonar device used in this project is a multibeam sonar, or multibeam echosounder. This type of sonar was first developed during the 1980s for assisting the navigation of submarines and it is now commonly used for hydrographic surveys ([96]).

Like any other sonar, it uses sound waves for the detection of a target that, in our case, is the sea ice underside. In opposition to single beam sonars though, multibeam echosounders use an array of transducers to emit sound in the shape of a fan that is wide across-track and narrow along-track ([56]).

The technique of creating a certain beam pattern to achieve spatial se-

lectivity is called “beamforming”. Beamforming is used to concentrate the power of the beam along a chosen direction, therefore improving the directivity of the array. It is done by combining signals from different transducers in such a way that they superpose and experience constructive interference for a certain angle that establishes the travel direction of the beam. For different angles, the signal decreases due to destructive interference, inhibiting signal propagation towards other directions.

For a linear array in far field approximation, that is for distances between the transducers much smaller than the distance from the target, the signal amplitude can be plotted as a function of the angle that it creates with respect to the array perpendicular axis, creating the “beam pattern”. A typical beam pattern formed after the interference of a line array multiple-transducers signal consists of a main lobe that transports the bulk of the signal energy and some side lobes that spread the signal towards other directions. An example of such a beam pattern is shown in figure 3.6.

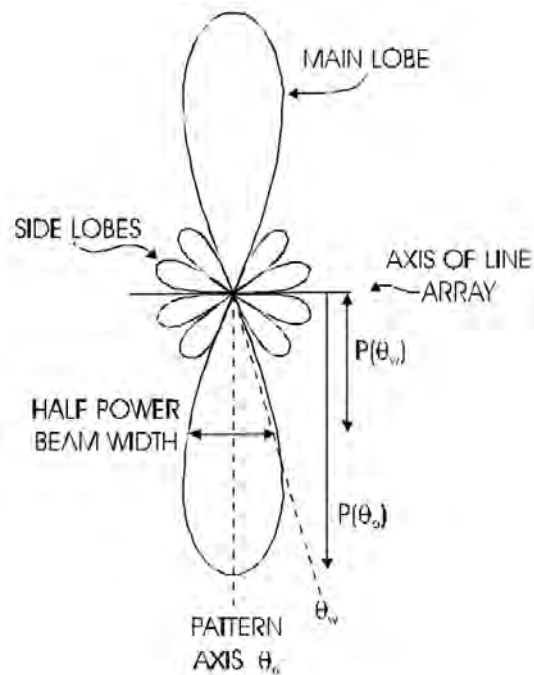


Figure 3.6: **Beam pattern of a multiple-element line array.** Image from [49]

Here θ_0 represents the direction of the peak energy projection, called

the “maximum response axis” or just “pattern axis” angle. This angle coincides with the centre of the main lobe, hence the maximum power value $P(\theta_0)$ is found along this axis.

θ_w is the angle between the pattern axis and the so called “half power point” of the beam pattern. This point is where the main lobe reaches a power $P(\theta_w)$ equal to half of the maximum value $P(\theta_0)$.

The width of the main lobe is a measure of the directivity of the pattern and it is generally measured at θ_w where the projector power reaches -3 dB (roughly half) that of the axis.

The half power beam width (*HPBW*) is a function of the dimension of the array and of the signal wavelength. A first approximation is given in formula 3.10:

$$HPBW = 50.6 \frac{\lambda}{D} \quad (3.10)$$

where the HPBW is given in degrees, λ is the wavelength of the signal, and D is the dimension of the array.

For high resolution surveys it is necessary to use a narrow beam. The HPBW can be reduced by either choosing a high frequency signal or by building large arrays of numerous transducers. However both solutions present their own limitations and a compromise is necessary between high resolution surveys, the physical size of the instrument, and the level of absorption in water that the signal experiences ([49]). Side lobes appear because of partial interference. They disturb the measurements but are unavoidable, therefore techniques such as “shading” are applied to minimise their impact ([56]).

A fan can be formed by many beams, from tens to hundreds. For the multibeam echosounder transmitter, each set of beams ensonifies a strip of the target surface called a “swath” (see figure 3.7), built up by considering the beam pattern in figure 3.6 in a three-dimensional space ([49]).

The multibeam echosounder receiver is composed of an array of hydrophones that collect the reflected signal. The echo is received in the shape of a fan that is composed, like the transmitter, of a certain number of beams. The wave reflected from the target is collected combining delayed signals from each hydrophone at slightly different times,

so that the difference in their paths due to the angle is accounted for.

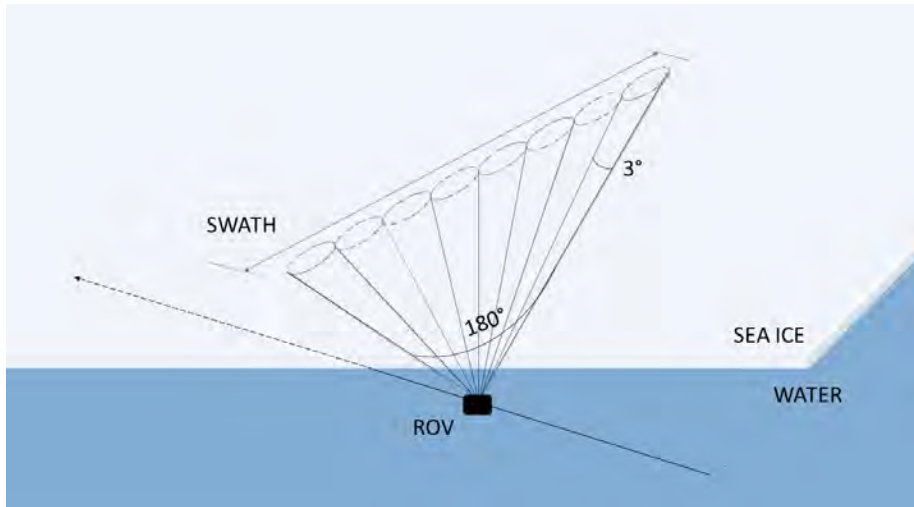


Figure 3.7: **Multibeam echosounder transmission swath for sea ice underside topography** Modified image from [49]

The most used array configuration for a multibeam sonar is called “Mill’s cross”, where transducer and receiver are mounted perpendicular to each other. This enables the study of a small area at a time, that represents the multibeam sonar footprint.

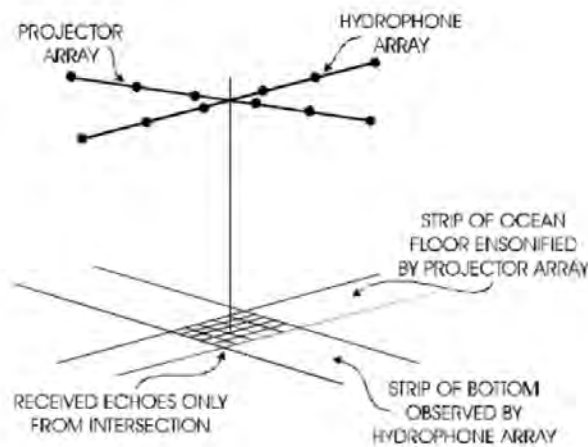


Figure 3.8: **Mill’s cross array configuration.** Image from [73]

The footprint is spatially defined by the intersection between the transmitter ensonified swath and the orthogonal swath observed by the receiving array (see figure 3.8). Dedicated transducers create a transmitter fan that is narrow in along track and much wider in across track, as shown in figure 3.7), while the opposite is true for the receiv-

ing fan. This creates a typical multibeam sonar footprint around 1° wide on each side, improving the signal bearing estimation.

The transmitted fan scans the underside of the sea ice while the ROV is moving. The receiving fan instead can be steered by changing the relative phase between consecutive receiving transducers. This technique is called “beam steering” and it allows to steer a beam electronically without physically moving the array. With this method the receiver can collect echoes from the whole swath ensonified by the transmitter hence building up the under-ice topography.

The use of the Mill’s cross configuration together with the beam forming and beam steering techniques enable therefore the collection of a large number of measurements.

Furthermore, in order to determine the transmission and collection angle of each beam, a multibeam echosounder requires accurate measurements of the motion of the vehicle relative to a cartesian coordinate system, called measurement “motion compensation”. The typical measured ROV values are the velocity of propagation, the position, and the attitude, which includes heave, pitch, roll, yaw, and heading ([56]).

The use of MBS is preferred for large surveys where accurate measurements of the topography are required in a reasonably short time ([49]). The use of arrays of transducers that is motion compensated enables accurate location and measurement of distances compared to SBS. Also, the width of the swaths together with the beam handling techniques described above make MBS very time efficient on a large scale, enabling several depth measurements from a single ping with a high resolution estimate of the signal bearing.

3.3 Electromagnetic induction sounding

Electromagnetic induction sounding (EMI) is a method widely used in Geophysics to study the composition of the ground. In this technique the different electrical conductivities of the materials are used to recognise ground structures and can also be used to retrieve the

thickness of the sampled material layers.



Figure 3.9: Airborne electromagnetic induction sounding survey

EMI is often applied in Sea Ice Physics as a method to measure sea ice thickness (see for example [71]). Measurements can be collected during both airborne, figure 3.9, and ground-based operations, figure 3.10.



Figure 3.10: EMI device mounted on a sledge for transportation during ground-based surveys. Image credit to Marcel Nicolaus

The EMI method works by inducing a magnetic field into the ground and by measuring the secondary magnetic field that is produced as a response of the inspected materials.

The schematic of EMI operations is shown in figure 3.11. Two coils are used: the first is the transmitter coil T and it is used to produce the primary magnetic field H_p that is sent into the ground; the second coil R is the receiver, whose role is to receive the secondary magnetic field H_s that is produced in the ground as a response to the action of the primary one.

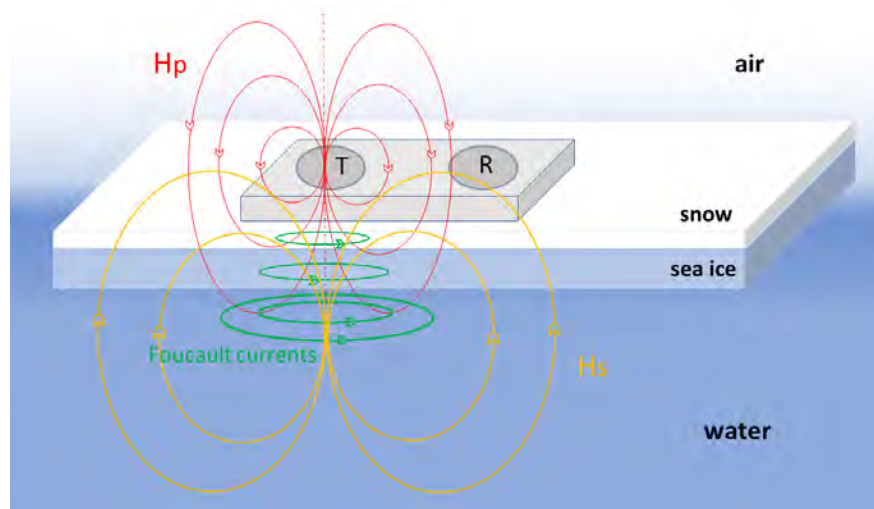


Figure 3.11: Schematic representation of EMI operations

When the primary magnetic field enters the ground the conductive materials in it react creating Foucault currents, according to Faraday's law of induction.

As induction depends on conductivity and the value for sea ice conductivity is at least two orders of magnitude less than the conductivity of sea water (10 mS m^{-1} against 10^3 mS m^{-1}), the Foucault currents are mainly induced directly under the bottom of the sea ice layer ([92]). These induced currents generate in turn a secondary magnetic field that opposes to the primary magnetic field that created it, as described by Lenz's law.

The secondary magnetic field is then received by the receiving coil and measured. Once that the secondary magnetic field has been measured, the ratio Z between the magnetic field strength of the secondary and the primary magnetic fields can be calculated.

When the EMI is operated in single frequency mode, the value for the apparent conductivity of the ground can be found and used to solve the Helmholtz equations for a vertical magnetic dipole using specific integral transformations ([71]). This process leads to the following equation for the ratio between the two magnetic fields:

$$Z = \frac{H_s}{H_p} = -r^3 \int_0^\infty R e^{-2kh} k^2 J_0(kr) dk \quad (3.11)$$

where r is the distance between the coils along the horizontal axis parallel to the ground; R is a function of both the frequency and the electromagnetic properties of the materials; k is the wavenumber; $J_0(kr)$ is the Bessel function of the first kind of order zero; and the parameter h denotes the distance between the receiver coil and the source of the secondary magnetic field.

The meaning of the parameter h differs in Geophysics and in Sea Ice Physics: in Geophysics it represents the height of the receiver coil above the ground; instead in Sea Ice Physics the layer that creates the secondary magnetic field is the sea water, hence h represents the distance between the receiver coil and the sea water below the sea ice. This is particularly important because the Foucault currents form very close to the underside of the sea ice layer, therefore the source of the secondary magnetic field, that coincides with the centre of the induced currents, stands at the bottom edge of the sea ice slab. Therefore, if the coils are in a configuration where they are in contact with the top surface of the ice, the quantity h is simply equal to the sea ice thickness.

Snow depth can be included in the total sea ice thickness value depending on the survey arrangement and on the environmental conditions.

Formula 3.11 shows the strong dependance of the secondary magnetic field on the spacing r between the two coils. This quantity also determines the footprint of the instrument, together with the distance h between coil and ice.

Inverting formula 3.11 enables the calculation of the sea ice thickness, h . This formula shows an inverse proportionality relation between the ice thickness and the strength of the secondary magnetic field: as the space between coils and sea water increases with increasing ice thickness, the strength of the magnetic field measured by the receiver decreases.

In this study the surveys are ground-based and the device used to perform electromagnetic induction sounding for sea ice thickness measurements is the Geophex electromagnetic sensor “GEM-2”. During a survey the instrument is positioned on a sledge for device transportation and dragged along the survey track together with a global positioning system (GPS), in order to record the coordinates of the survey simultaneously with the sea ice thickness distribution. The typical vertical resolution of the GEM-2 is 0.1 m, and the sampling rate is 10 Hz.

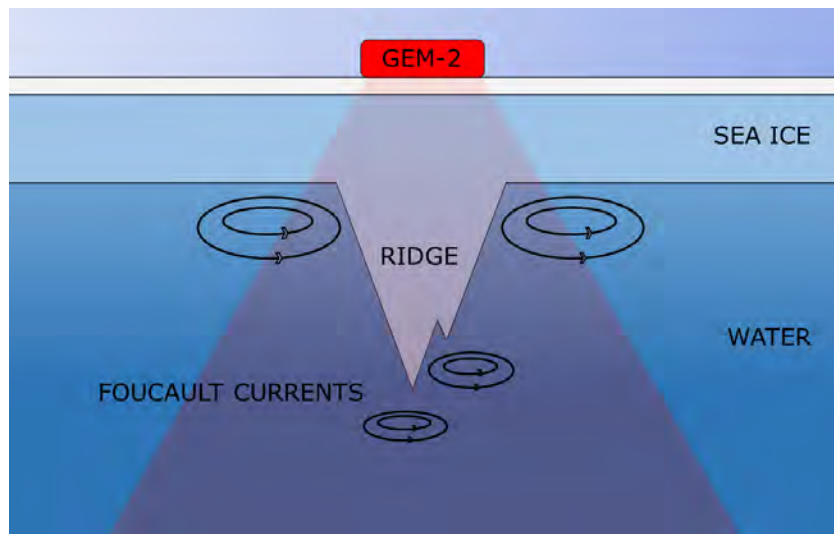


Figure 3.12: **GEM-2 induction of Foucault currents in deformed sea ice**

The footprint of the instrument is defined as the area where 90% of the induction process takes place ([54]). For ground-based surveys the footprint is around four times the thickness of the ice, depending on the instrument internal configuration and on the height of the coils above the ground ([38]).

The footprint is also found to be strongly dependent on the under-ice topography ([38]). Figure 3.12 shows the formation of Foucault currents when the GEM-2 is operated above a ridge: lateral currents form

in the water beside the ridge as well as below it.

In general, it is found that the EMI technique underestimates sea ice thickness for deformed ice ([74]). This can be explained by comparing the footprint of the instrument with the size of the sea ice deformation features.

Deformed sea ice thickness is generally highly variable within the footprint of the device, hence the measured mean sea ice thickness is less accurate because it is averaged over a wide area. In case of a large footprint comparable to the size of a ridge, for example, it is found that the GEM-2 receives a signal from the lateral currents beside the ridge that is stronger than that originating from the induced currents laying below the ridge edge. This is because, as previously explained, the strength of the secondary magnetic field is higher for those currents that lay closer to the receiver coil of the device, while fields originating from further are weaker and therefore are not registered.

Therefore in this case most of the secondary magnetic field originates from depths that are shallower than the real size of the ridge, consequently resulting in an underestimation of its thickness.

3.4 Snow depth measurements

In case the survey area is covered in snow the electromagnetic system does not measure sea ice thickness directly, but it measures the sum of sea ice thickness and snow depth. Thus, in order to retrieve sea ice thickness only, it is necessary to measure the snow depth with an independent instrument and then subtract it from the GEM-2 measurements. The snow depth of the areas investigated in this thesis has been measured using the instrument “Magna Probe” (Snow-Hydro, Fairbanks, Alaska, USA).

This tool consists of a pole around 1.7 m long and of a wide disk attached to the end of the pole. To measure snow depth the pole is vertically pushed into the snow; the disk then rises, remaining above the snowpack. The disk height above the ice is then equal to the snow depth, and this value is recorded by pressing a button situated on the rod. The electronics stores the data collected in a logger, from where they can be easily extracted in raw format and handled on a computer.



Figure 3.13: **Simultaneous operation of the GEM-2 and the Magna Probe** (Image credit to Marcel Nicolaus)

This instrument enables a quick collection of snow depth measurements, making the sampling procedure more efficient than manual recording. The vertical resolution of the Magna Probe is 0.01 m ([101]).

In this study the Magna Probe is used to sample snow depth along the same track of the GEM-2, as it can be seen in figure 3.13. The Magna Probe is provided with a GPS, hence combining the use of the GEM-2 with the Magna Probe enables simultaneous measurements of snow depth, sea ice thickness, and respective spatial coordinates for both instruments.

3.5 Draft calculation from thickness measurements

Multibeam sonar and electromagnetic induction sounding measure two different vertical components of sea ice thickness: the GEM-2 measures total ice thickness and snow depth, while the MBS measures the draft, that is only part of the total ice thickness. To be able to compare the two datasets it is then necessary to calculate draft values from thickness measurements, or the opposite.

For this study I have decided to calculate the draft from the thickness measurements collected by the GEM-2, therefore setting the MBS

as the instrument of reference. In order to do this I have chosen an isostasy based model that is commonly used for this purpose ([77] and [2]).

In this model sea ice is considered as a free floating medium and its components can be assumed to be in isostatic equilibrium.

Using the definitions of section 3.1 it is possible to write a relation between the different vertical parts of the sea ice structure as follows:

$$\rho_i H + \rho_s h_s = \rho_w h_d \quad (3.12)$$

where ρ_i represents the sea ice density, ρ_s the snow density, and ρ_w the sea water density.

Inverting formula 3.12 sea ice draft can be calculated as a function of sea ice thickness and snow depth, as shown in formula 3.13.

$$h_d = \left(\frac{\rho_i}{\rho_w}\right)H + \left(\frac{\rho_s}{\rho_w}\right)h_s \quad (3.13)$$

Using this equation I have converted each value of sea ice thickness measured by the GEM-2 into draft measurements for a future comparison with the MBS data.

3.6 Modeling sea ice growth

Modeling sea ice growth is important in climate science to understand the processes involved in sea ice changes and predict the future factors that lead to variations in sea ice thickness and extent, important parameters commonly taken as indicators for climate change ([92]).

This can improve our understanding of the temporal and spatial evolution of many other characteristic phenomena of the polar environments that are closely related to sea ice transformations (see for example [9]).

3.6.1 Sea ice formation and growth processes

Sea ice forms and starts to grow during the so-called “freeze-up” period that takes place in the Arctic around the month of September ([92]), at the end of the Arctic summer. It generally continues to

grow during winter and until early spring, when it begins to melt. The melting season in the Arctic takes place around March and the start of this period is also known as the “break-up” period. Precise definitions of starting and ending dates of freeze-up and break-up can be found in literature (see for example [41]).

Formation and growth of sea ice entails three major stages: initial formation with ice nucleation, lateral growth, and vertical growth ([81]). When sea water reaches the freezing temperature of -1.8°C it starts to nucleate small ice crystals that form and increase in size. The first stage of sea ice growth is called “lateral growth”. During this period ice crystals expand and coagulate together forming a first cover of thin ice on the water surface, called “grease ice”. Afterwards, the second step of growth called “vertical growth” follows. At this stage the ice sheet starts to grow vertically by following the direction of maximum heat flow between water and atmosphere ([81]).

The surveys analysed in this thesis took place during the September/early October freeze-up period, when sea ice starts to thicken. This section will therefore focus on the study of sea ice vertical growth.

The extent of vertical growth can depend on many factors and various dynamics. Its variability is an important parameter in sea ice modeling and one of the main features that has been strongly affected by climate change during the last decades ([87]).

A model for sea ice vertical growth, that from now on will be referred to simply as growth, are discussed in this section and the results of its implementation using this work datasets are later presented in chapter “Results”.

The ice crystal formation causes salt to be expelled from the crystal lattice. Part of the sea ice salt content is released in the water below, during the so-called “brine rejection” process and part is trapped between the ice crystals. The process of vertical growth is also known as “congelation”. It begins at the bottom of the already formed sea ice cover and leads to the creation of the “congelation layer” ([81]). These two parts of the ice can be distinguished by their texture originating from the different solidification processes experienced. The

grains in the sea ice cover are small as they experience turbulent mixing at the surface, and continuously undergo brine rejection while the heat is lost from the surface. Consequently the ice in the upper layer becomes more compact and shows a granular texture. Instead, the congelation layer grows away from the surface under layers of ice. The quiescent growth forms ice in a columnar shape. Ice at the bottom shows a lamellar growth that results in a brine channel system, where most of the salt is trapped within the ice ([50]).

Ice grows thermodynamically mainly as a result of temperature difference between the surface and the ocean, resulting in an increase of sea ice thickness in response to a negative energy budget between ocean and ice ([81]). However, mechanical growth also happens, especially in rough seas conditions due to wind and currents. Mechanical movements can lead to ridging and rafting processes, cracking of ice sheet, breaking ice floe edges during collisions, and piling up of ice blocks resulting in a dynamical growth. While thermodynamic growth leads to a regular trend in the evolution of sea ice thickness, dynamic growth can lead to sudden and abrupt changes. A schematic illustration and a real picture of a ridge formation are shown in figure 3.14.

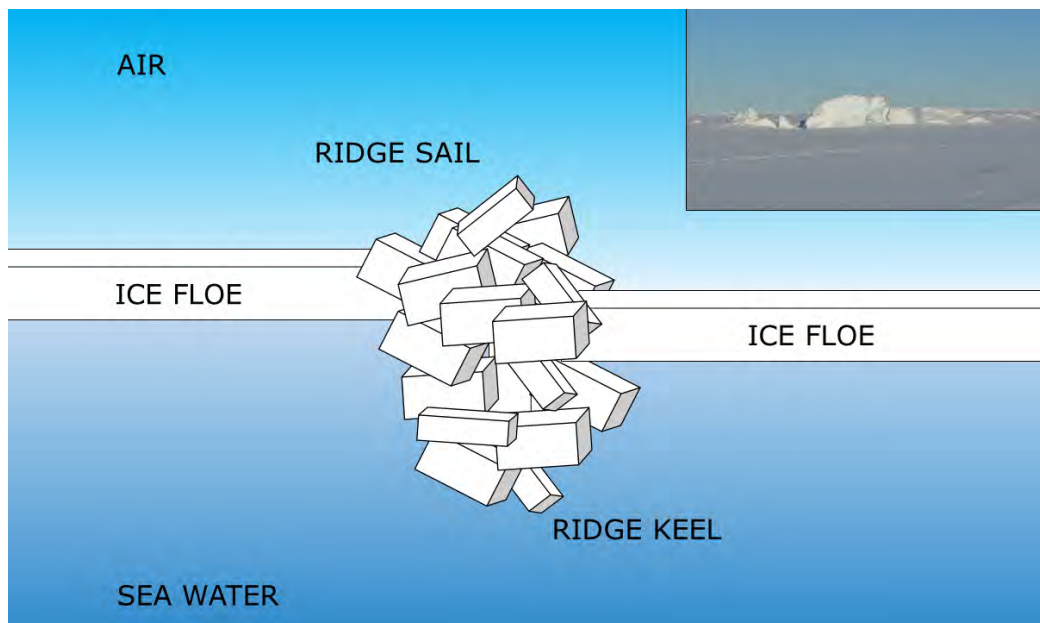


Figure 3.14: **Schematic of ridge components and view of ridge formations in the Arctic (upper-right corner)**

Concerning the surveys of this work, the main processes that drive

sea ice growth and that can be used for modeling sea ice thickness as a function of time belong to the thermodynamics. This study will therefore investigate the potential thermodynamic growth for the collected data time series.

Thermodynamic sea ice growth depends mainly on three parameters: air temperature, ice thickness and snow cover ([82]).

There are of course other quantities that influence sea ice growth and that can play a major role in some specific cases; among these are currents, wind conditions, snow albedo, snow density, and solar radiation. It is although more difficult to quantify these parameters and they are generally not taken into account in simple models for sea ice growth estimates.

Several different models can be found in literature which have been used during the last 60 years to model sea ice growth. The majority of these are analytical models, while some of them employ few empirical coefficients obtained by repeated measurements from a selected location. An example of these semi-empirical models is the one used by Anderson that is described in the following ([5]).

The next section is dedicated to the description of the so-called “Freezing-degree days model”, which is the model that is used in this work and one of the most popular models for sea ice growth prediction.

3.6.2 Freezing-degree days model

To achieve an estimate of the sea ice growth I have used in this work one of the mathematical models developed during the last decades. Exhaustive models are very elaborate because they require the knowledge of a high number of parameters.

In general, modeling sea ice growth is a long and complicated process. However it has been proved, first by Stefan in 1891 ([86]) followed by many other modelers (see for example [53]), that with some simplifications it is possible to achieve a model that is less sophisticated, but accurate enough to give a good estimate of sea ice growth ([53]).

The so-called “Freezing-Degree Days” model (FDD) enables simple modeling of sea ice growth and its use is very common in sea ice

physics. It generally applies to level ice, although it can be modified to take into account ridges and rubble ice ([53]). In this work no deformed ice growth is analysed using this model.

This model is purely based on thermodynamic effects and does not take into account any mechanical type of growth. It can apply to newly formed ice and remains valid for multi-year ice up to 5 m ([81]). Thermodynamic growth takes place each winter. It thickens the newly formed sea ice and increases the thickness of the remaining layer of an ice sheet that survived the melt season. Every growing season, if the ice sheet does not completely melt during the summer, sea ice experiences a new growth cycle, becoming multi-year ice. MYI shows therefore a vertical division in layers formed by the alternation of the different seasons and annual layers are visible in ice cores, similarly to what happens for tree growth rings (3.15).

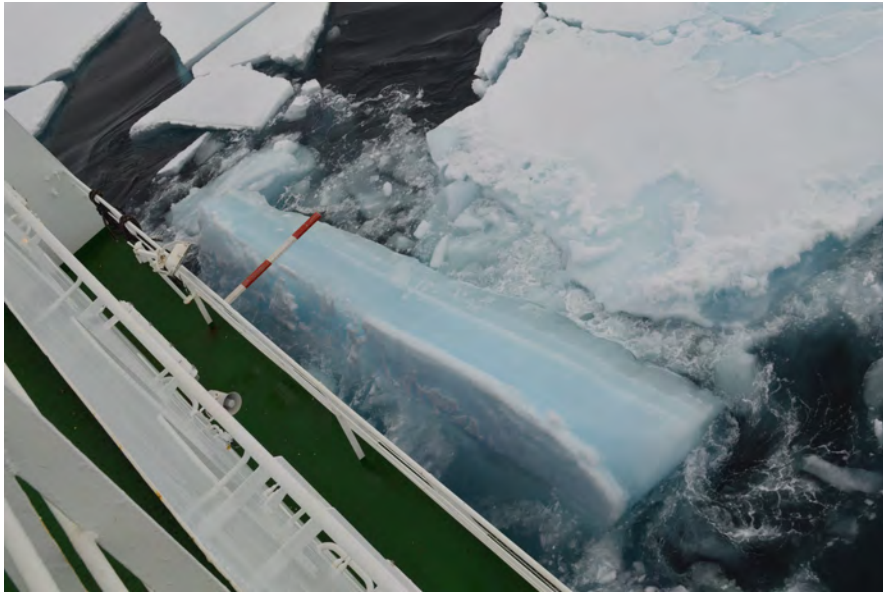


Figure 3.15: Multi-year ice sheet showing annual growth layers

The outcome of the FDD model gives sea ice thickness as a function of time for a certain observation period at sea ice freezing air temperatures.

The factors that control sea ice growth in the Freezing-degree days model are threefold ([81]):

- **Air temperature:** cold air at the sea ice surface determines a significant heat dispersion of energy transferred from the warm

ocean to the cold environment above the ice. Sea ice growth rate depends on the difference between water and air temperature and on the amount of days at freezing temperature;

- **Current sea ice thickness:** the rate at which sea ice thickness increases depends on the thickness of the existent ice sheet; ice growth rate decreases with the actual ice thickness due to limited conduction, consequently for thick ice the rate of thermodynamic growth is expected to be slower than for thin ice;
- **Snow cover depth:** the accumulation of snow on top of sea ice generally slows the ice growth down. The role of snow is one of the most studied phenomena concerning sea ice growth modeling and it is therefore explained in more detail in subsection 3.6.2.

Snow cover implications for sea ice growth

The presence of snow on top of the ice changes the dynamics of sea ice growth. Two main parameters influence the sea ice thickness growth rate: the snow heat transfer coefficient and the snow albedo.

First, snow thermal conductivity is around one order of magnitude smaller than that of the ice. As a consequence, a layer of snow acts like an insulator on the sea ice and diminishes the heat transfer through its surface. Snow thermal conductivity values vary depending on snow conditions: fresh snow is a good insulator because it contains lots of air, while compact snow allows the heat to escape from the ice towards the atmosphere. It follows that snow covered sea ice is less affected by cold air temperatures than bare ice, hence the temperature difference across the ice slab is smaller. As a result of this, the temperature of snow covered ice stays relatively warmer and the resulting ice growth is slower than for bare ice.

To give an idea of the magnitude of the insulation effect of snow presence it is useful knowing that 0.5 m of ice covered by 0.05 m of snow grows at half of the bare ice rate ([92]).

The other main snow property that affects ice growth is its albedo.

Snow albedo is higher than ice albedo, therefore snow reflects a higher amount of incident radiation, influencing the energy balance: short-wave sun radiation components are not transmitted to the ice and the temperature at the ice surface will keep warmer than for bare ice, slowing down the ice growth. In this study snow albedo does not consistently influence sea ice growth because the amount of sun radiation reaching the sea ice during the freeze-up period is neglectable ([81]).

In conclusion, a snow layer generally acts as a blanket on the sea ice. The presence of a snow cover significantly decreases sea ice growth rate, hence snow-covered ice generally grows to be thinner than snow-free ice. This is true until the snow load reaches a certain threshold, otherwise its weight causes the ice to sink. However this process rarely happens in the Arctic and it will not be discussed in this study (see for example [7]).

This brief explanation describes how even a thin snow cover can have drastic implications for the rate of sea ice growth. It also reveals the significant necessity to account for snow presence in sea ice growth models in order to achieve accurate predictions.

Freezing-degree days model: mathematical formulation

The FDD model is a simplified version of the more complicated models for energy balance and heat flux transfer between the ocean and the atmosphere through sea ice.

A complete model takes into account: the incoming oceanic heat flux F_w moving from the warm ocean and reaching the colder ice interface; the heat flux F_c created by the difference in temperature between the air and the ocean that is conducted through the ice towards the upper surface; and the heat released during freezing that can be calculated by multiplying the water latent heat L_i , the ice density ρ_i , and the growth rate dH/dt of sea ice thickness as a function of time ([81]). No component of heat flux coming from solar radiation is taken into account in this study because, as already mentioned, the measurements belong to the freeze-up period when the sea ice does not receive a significant amount of light from the sun ([92]).

Following the convention of positive fluxes in the upward direction entering the ice, the energy balance can be formulated as follows:

$$F_w - F_c + \rho_i L_i \left(\frac{dH}{dt} \right) = 0 \quad (3.14)$$

In order to determine the heat exchange, the temperature T_w of the water and the temperature of the sea ice surface must be known. The surface temperature is difficult to delimit and to measure, therefore in the FDD model a practical simplification that supposes the surface temperature to be equal to the air temperature T_a is generally used ([82], [11]).

A scheme of heat fluxes through an ice sheet of thickness H covered with a snow layer of depth h_s is shown in figure 3.16. dH/dt shows the direction of growth for sea ice.

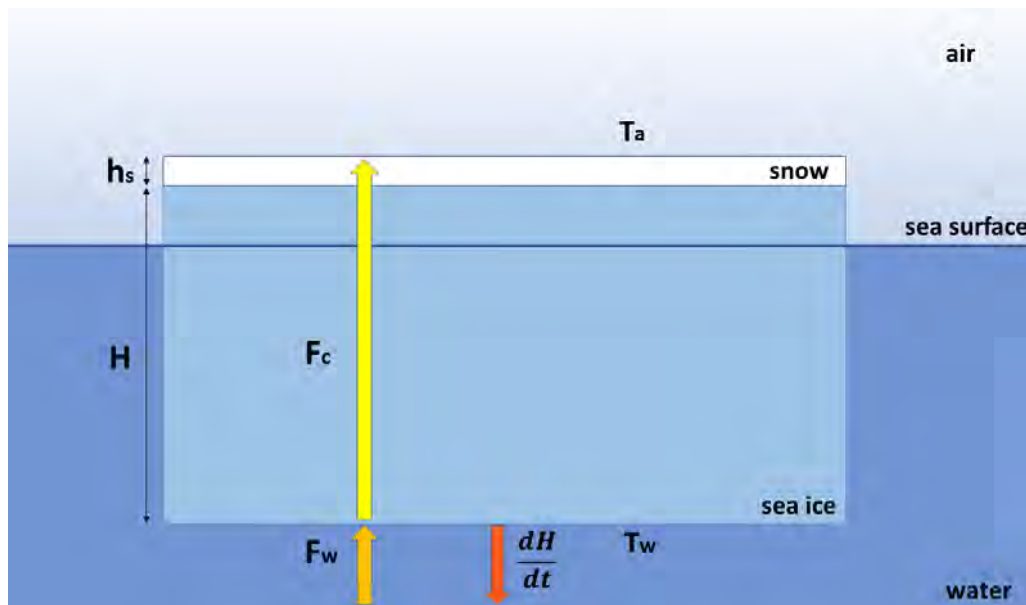


Figure 3.16: Scheme of heat transfer during sea ice growth

Both the heat released during the ice freezing process and the oceanic heat are transferred to the surface of the ice and finally released into the atmosphere.

The temperature of the ocean under the sea ice is generally at the freezing point for sea water, with some local variations due to salinity changes ([81]).

The ocean is generally warmer than the air even in winter. Temperature increases in oceanic water can sometimes melt the ice leading to completely ice free areas called “polynyas” ([83]). As in our study the water temperature remains substantially constant at the freezing point during the whole campaign, and as no polynyas has been recorded, the process of creating ice free regions through heat exchange from below the ice is not taken into account in the model.

Without loss of generality the water temperature can be assumed to be constant around $-1.8\text{ }^{\circ}\text{C}$ (for a value of salinity of 35 ppt ([3])). For this reason the gradient of temperature along the ice structure changes significantly according to the surface temperature. Surface temperature should be measured at the boundary between the ice (or the snow cover) and the air. However in this study there is no direct record of this quantity hence the surface temperature is set to be equal to the air temperature that is continuously recorded during the surveys by the weather station of the ship. In this study the values of air and water temperature that are used in the FDD model are averaged over a period of one day.

In the FDD model the relation between conductive heat flux and temperature is approximated to be linear and expressed by the Fourier’s law for heat conduction for two layers ([11]). Continuity of the conductive heat flux through the ice and snow layers and into the atmosphere is also assumed ([81]). The resultant net heat flux equation is:

$$F_w + \rho_i L_i \left(\frac{dH}{dt} \right) = \frac{T_w - T_a}{\left(\frac{1}{k} + \frac{H}{k_i} + \frac{h_s}{k_s} \right)} \quad (3.15)$$

where k is the atmospheric heat transfer coefficient between the ice (or snow if present) surface and the atmosphere, and k_i and k_s are the thermal conductivity of ice and snow respectively.

This formula can be used for modeling thermodynamical driven sea ice growth in case that time series of snow depth, air temperature, water temperature, and oceanic heat flux are provided.

If some of these quantities are not available, as it is the case for this

study, more assumptions must be used to further simplify the model.

The following assumptions are here made:

- The heat flux from the ocean is neglectable: the oceanic flux F_w is set to zero;
- The water temperature T_w could be either set equal to the freezing temperature of sea water for the whole survey or changed daily. This will not have a big impact on the result, as the differences in the water temperature are minimal in this study (from a minimum of -1.8 °C to a maximum of -1.6 °C). I have decided to take into account the local changes of salinity, recording local sea water temperatures instead of assuming a constant value for the whole campaign;
- The surface temperature is assumed to be equal to the air temperature T_a . Each day of the survey is characterised by a constant air temperature that is equal to the mean of the registered temperature throughout the day;
- k and the surface temperature are constant in time, hence $k \rightarrow \infty$;
- the snow depth can be assumed to increase linearly with ice thickness, as it is generally found (see for example [80]) according to formula ([11], [53]):

$$h_s = \alpha H \tag{3.16}$$

Where α is a proportionality coefficient that in this work can be calculated using the GEM-2 collected datasets (see section 4.4). Snow layers characterised by α coefficients bigger than 0.3 cause flooding of the sea ice surface, changing the dynamics of the growth ([92]). The snow/ice ratio in our dataset is always below this threshold value, so that flooding is not considered in this model.

The use of the previous assumptions cause sea ice growth to depend mainly on the temperature difference between water and air in the survey area.

To model sea ice growth over a certain period, equation 3.15 can be integrated over time. The formula for the calculation of the sea ice final thickness after a certain growth time is:

$$H^2(D) - H^2(1) = \frac{2k_i}{\rho_i L_i} \frac{1}{\left(1 + \frac{k_i \alpha}{k_s}\right)} \int_1^D (T_w - T_a) dt \quad (3.17)$$

where $H(D)$ is the sea ice thickness predicted for the last day “ D ” of the study; $H(1)$ is the initial ice thickness measured during the first day of the study, day 1; and the integral over time is calculated for the time interval of the survey.

The integral $\int_1^D (T_w - T_a) dt$ is the parameter that gives the name to the model: it represents the summation of the average daily subfreezing degrees for a certain period of time, and it is commonly indicated in literature as “FDD”.

An example of the use of the FDD model is found in [82]. Here measured sea ice growth is compared to FDD calculations, resulting in the ice thickness trend as a function of freezing-degree days is shown in figure 3.17.

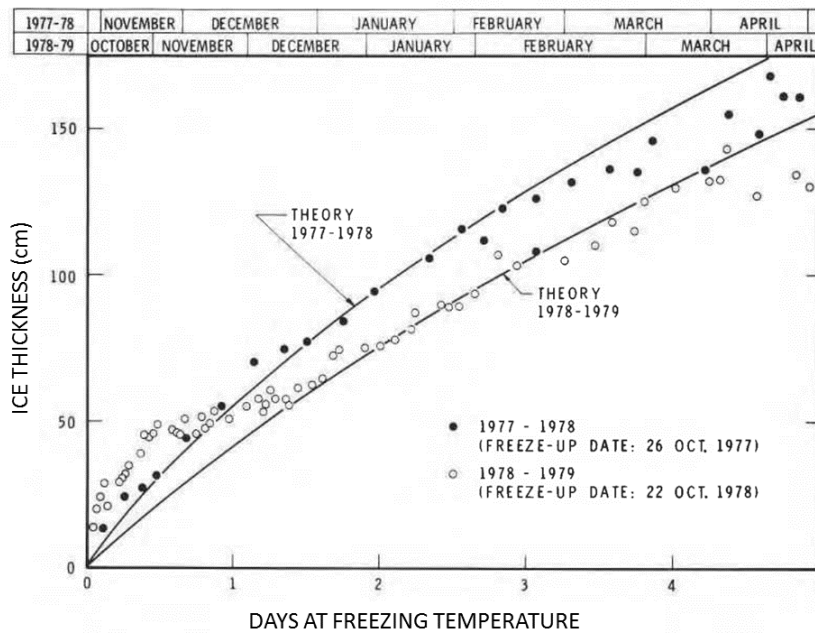


Figure 3.17: Measured sea ice growth compared to FDD calculations. Image from [82]

In literature measured values of sea ice thickness growth are found to be between 5 mm/day to 20 mm/day, depending, among other factors, on the season, the accumulated snow depth, and on the location of the area ([81]).

In case of absence of snow cover, equation 3.17 will reduce to the so-called ‘‘Stefan’s law’’ ([86]). This is one of the oldest and most simple models for sea ice growth which states that sea ice thickness grows with the square root of time:

$$H^2(D) = \frac{2k_i}{\rho_i L_i} \int_1^D (T_w - T_a) dt \quad (3.18)$$

In this formula h_s is set to zero because of the lack of snow, and the initial sea ice thickness $H(1)$ is also supposed to be zero. This means that Stefan’s law gives a consistent result only if the area of study is ice-free at the beginning of the survey and does not apply to this study case.

As anticipated, in 1961 D. L. Anderson tried an empirical approach to model sea ice growth, obtaining the values for the coefficients in Stefan’s law from time series of air temperature and ice thickness measured on site ([5]).

This method uses the following formula for the calculation of sea ice thickness thickening after a period of thermodynamic growth:

$$H^2 + 5.1H - 6.7 \int_0^D (T_w - T_a) dt = 0 \quad (3.19)$$

where time is expressed in days, thickness in centimeters, and the snow cover is parameterised using a factor $\alpha = 0.13$ for the mean ratio between snow depth and ice thickness ([92]). This approximate ice growth equation only applies to sea ice that is less than 80 cm thick.

A complete analysis of sea ice growth should consider more parameters in the FDD model, such as wind effects (see for example [30] and [8]), a thorough description of radiative and turbulent fluxes ([6]), and the influence of the seafloor on oceanic current and sea ice movements ([66]).

Chapter 4

Methods

4.1 Data collection

4.1.1 Area of study

The data of this project have been collected during the 101st expedition of the German research vessel “Polarstern” (PS101) to the Arctic, in the late Arctic summer of 2016.

The route of the expedition is shown in figure 4.1: the ship left from Tromsø, Norway and headed northeast of the Svalbard archipelago to reach the sea ice in September.

This thesis focuses on three campaign stations, taking place on the 26th of September, 29th of September, and 1st of October.

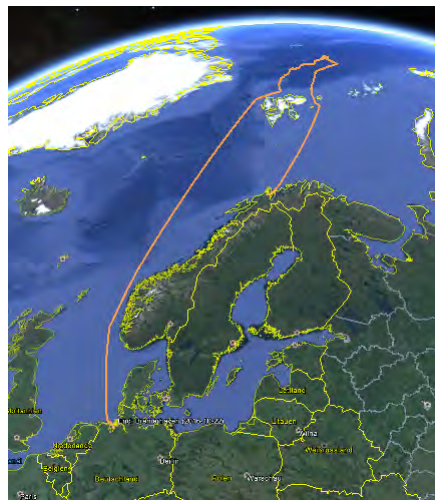


Figure 4.1: **Track of the PS101 Polarstern expedition**

The ArcGis map to the left of figure 4.2 shows the area of study of the campaign and the red box highlights the region studied in this work.

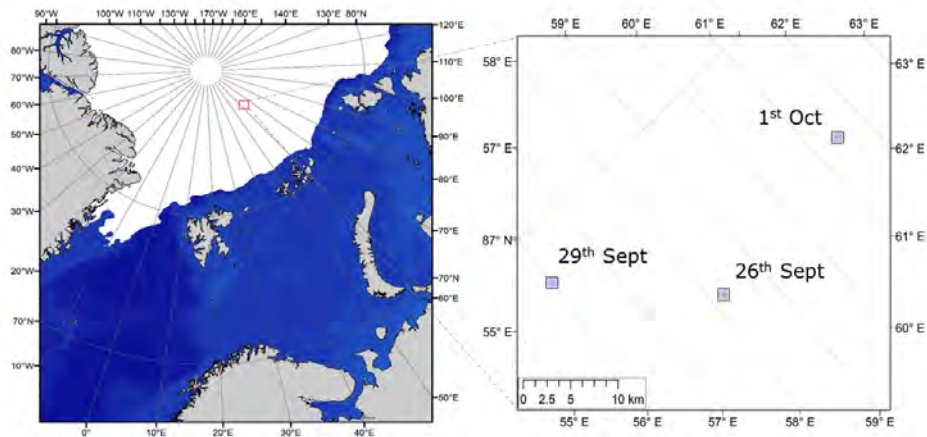


Figure 4.2: Map of the PS101 survey area. To the left: the red box shows the location of the three stations examined in this thesis work. To the right: zoom in of the red box area. The sea ice extent shown represents the average extent during the time period of the three stations, and it is averaged on the 5 days around the 28th of September, as extracted by the SSMIS data store of the ICDC Hamburg data centre ([42]) (Modified image from Luke Storrie)

A zoomed map of the three survey areas is displayed to the right of figure 4.2.

4.1.2 Instrumentation and survey logistics

During a station survey many different scientific instruments work at the same time. This thesis focuses on the use of the Alfred Wegener Institute remotely operated underwater vehicle to study the underside of the sea ice. Figure 4.3 and 4.4 show the ROV during fieldwork.



Figure 4.3: Side view of the remotely operated underwater vehicle. The multi-beam sonar is positioned in the black case with the AWI logo



Figure 4.4: **Front view of the remotely operated underwater vehicle**

The ROV is equipped with a large number of sensors from several disciplines; among these the upward looking multibeam sonar is the main sensor studied in this work.

At the beginning of a survey the ROV is deployed in the water through a hole cut in the ice or from the edge of the ice floe, as shown in figure 4.5 and 4.6 respectively. It is then driven for some hours under the sea ice, collecting a wide set of interdisciplinary data along its track ([43]). Data are continuously transmitted to the computers of the base camp through a long tether attached to the vehicle.

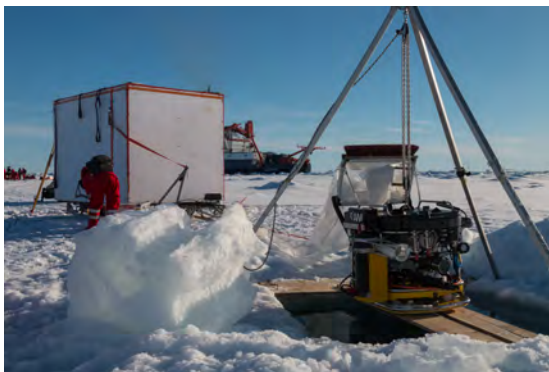


Figure 4.5: **ROV deployment through hole**



Figure 4.6: **ROV deployment from ice edge**

When the underwater survey is concluded the ROV is pulled out of the hole and the surveys above the sea ice begin. This second part of the work is dedicated to measuring sea ice thickness and snow depth

using an electromagnetic device together with the Magna Probe. The goal is to sample from above the same area of sea ice that has just been investigated from below by the ROV.

Navigating underwater can be very challenging in the Arctic. Problems with the navigation positioning system, low light levels, lack of reference points, and under-ice currents can cause the ROV to be driven away from the desired initial direction.



Figure 4.7: View of the navigation poles and GPS above the surface

To guide the vehicle, navigation poles are generally used and marked above the surface by flags, as shown in figure 4.7.



Figure 4.8: Underwater view of a navigation pole sticking below the sea ice

They are positioned under the ice at regular distances between each other to form a grid for the ROV. The poles are made to hang 3 m

below the ice so that they can be easily spotted using the navigation camera installed on the vehicle (4.8).

To spot and recognise them in low visibility conditions, these special poles show a white and red binary system pattern that associates each of them with their respective position in the grid along the planned track. A typical size for the grid is of the order of (100×50) m varying mainly depending on the ice surface morphology of the area.

This thesis goal is to use the multibeam upward-looking sonar to create a topographical map of the underside of the sea ice. Therefore, the main idea behind such a survey is to cover as thoroughly as possible a designated area. To do this the “mow the lawn” technique is generally preferred; it consists of driving the vehicle back and forward in parallel lines in order to homogeneously cover the area of interest.

The ROV maps created though display tracks with very different shapes between the three stations (see for example those in paragraph 5.3). This is due to two main causes.

One is linked to the several problems that can cause the ROV to drift during navigation, such as deviations due to currents, bad visibility, time issues, positioning issues due to interferences with other instruments, and/or sensors malfunctioning.

The second reason depends on the purpose of these surveys: as the ROV is a multidisciplinary sensors platform it is meant to collect various different datasets during a single survey. This might lead to conflicts when planning the track of the vehicle and the modality of the survey. As PS101 was the first expedition where the upward-looking multibeam sonar was tested, the choice of the track was not aimed only to the use of this particular sensor, but it was supposed to overlap with the operation of the other sensors mounted on the ROV for an efficient data collection.

Position on the ice is recorded using three GPS receivers placed at the corners of the grid of poles, creating a floe-fixed coordinate system. This system is used for positioning both sea ice thickness and snow depth datasets collected by the GEM and the Magna Probe respectively.

The ROV position under the ice is determined using an ultra-short

baseline (USBL) acoustic positioning system (MicronNav, Trittech, UK). The USBL calculates the vehicle positions in a X-Y coordinate system using the transponder mounted on the ROV. A conversion to geographic coordinates for the ROV position is necessary for the several softwares involved in the recording, renavigation, and multibeam sonar data handling processes for them to function properly. Hence why the transducer is given a fixed geographical position and the ice floe drift velocity is taken into account causing the new coordinates to be pseudo-geographical only.

A coordinate system conversion allows data recorded from below and from above the surface to be compared.

4.1.3 The remotely operated vehicle

During the last decade there has been an increasing trend in using marine robotic technology to study Arctic and Antarctic sea ice regions ([43]). ROVs and AUVs are used to investigate areas otherwise understudied because of clear logistical issues in accessing them.

The AWI newly developed research platform is aimed for interdisciplinary under-ice research and despite its small size, it provides a comprehensive sensor platform for studying the environment of the ice underside.

The ROV is a customised Ocean Modules M500 vehicle, built as a collaboration between the Swedish company “Ocean Modules” and scientists at AWI. It weighs 130 kg including all the sensors and it has a height of 0.73 m, length of 0.97 m, and a width of 0.75 m. The small size makes possible for the ROV to be deployed by only two persons. During navigation just 3 people are required to be in site: a pilot, a co-pilot, and an assistant to handle the tether.

Although built to work at a maximum depth of 500 m, the tether length limits the range to 300 m. However most of the operations take place in the upper 50 m of the water column, as the principal goal is to study the sea ice underside and its interaction with the marine environment underneath ([43]).

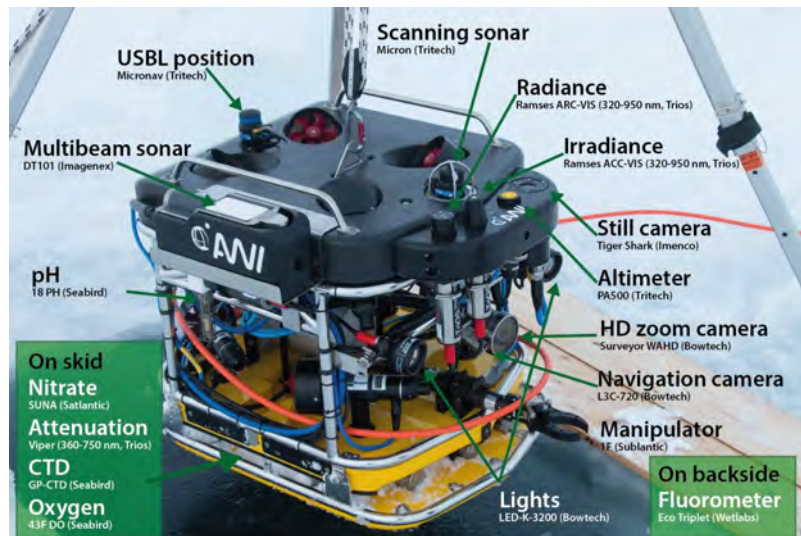


Figure 4.9: ROV sensors position (Image from [43])

The ROV houses several sensors, both for navigation and for scientific purposes, shown in figure 4.9.

Video cameras, an altimeter, and a scanning sonar are used to navigate under the ice and avoid collisions with it. A pressure sensor is used for depth measurements and to calculate sea ice draft together with the multibeam sonar. The ROV position is determined by the use of the USBL mentioned before, and the attitude by an inertial measuring unit.

Among the many scientific sensors are: the multibeam sonar for 3D underside topography and sea ice thickness measurements; two hyperspectral radiometers to measure light radiance and irradiance under the ice; biological sensors for measuring pH, nitrate, and chlorophyll fluorescence; and a CTD package (SBE GPCTD, Seabird Scientific, USA) for oceanographical measurements, such as temperature, salinity, and pressure.

These and other sensors allow for an interdisciplinary and comprehensive investigation of the under-ice environment during a single survey.

4.1.4 Multibeam sonar specifics

The type of sonar device employed in this thesis work is the Imagenex DT101 multibeam profiling sonar. It is a multibeam echo-sounder that is widely applied in bathymetric surveys.



Figure 4.10: **Imagenex DT101 multibeam profiling sonar**

The instrument integrates a multibeam sonar, a motion reference unit, and a sound velocity sensor into one single compact unit. DT101 requires only one cable for operating these three sensors.

Figure 4.10 shows the multibeam sonar complete unit, while figure 4.11 represents a schematic view of the MBS mounted on the ROV: the sonar is collocated on the top part of the vehicle in order to enable the upward-looking survey mode.

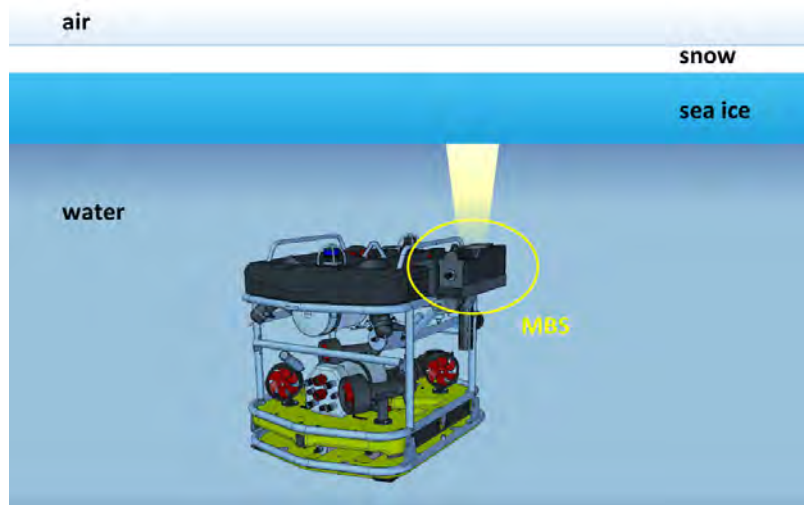


Figure 4.11: **Schematic view of the MBS (yellow circle) mounted on the ROV**

The DT101 multibeam sonar can work at a maximum depth of 300 m, it has a water depth range of 75 m, and a slant range of 150 m. The frequency is 240 kHz and it has a maximum ping frequency rate of 20 Hz. Both the transmitter and the receiver have angle widths of 3° along-track and 120° across-track. The resulting fan has a selectable number of beams from 120 to 480.

Further details can be found in the “DT101 Specification sheet” in

Appendix A.

4.1.5 Navigation and multibeam sonar dedicated software

Various software is necessary to record and handle the high amount of data collected by the ROV even just after few hours of dive.

The MBS raw data are collected using the dedicated Imagenex DT101 software. This software also enables the regulation of the range and gain of the acoustic signal during the surveys, and the display of navigation information and under ice topography both live and in playback.

The topography is displayed by using a colour map that represents the strenght of the return acoustic signal and by instantaneous profiles showing the average depth.

The DT101 software is particularly useful during navigation as it helps visualise the under ice environment where the vehicle moves, while recording the ROV attitude data and giving a complete diagnostic of the MBS.

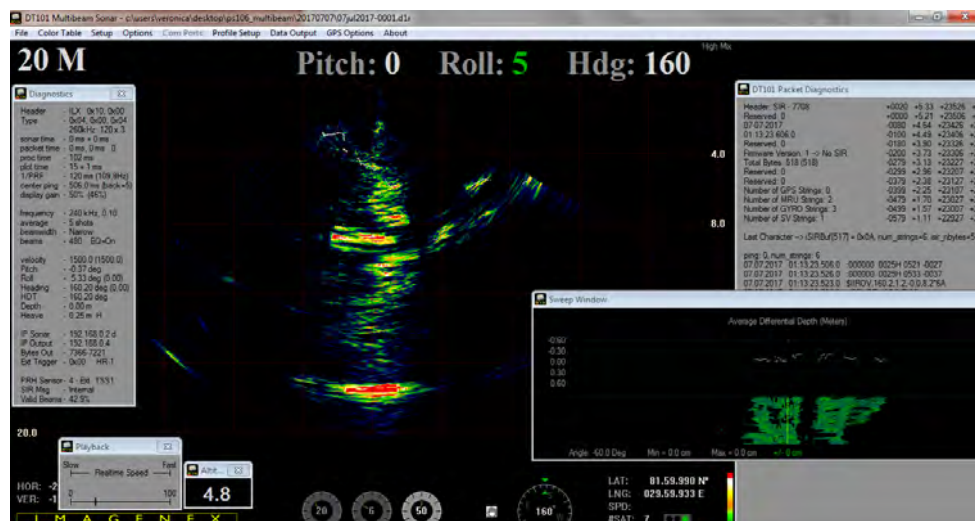


Figure 4.12: Screen capture of the main window of the DT101 program

Figure 4.12 and 4.13 show the DT101 interface when working in playback. Figure 4.12 shows the complete screen configuration used to monitor the MBS work during a survey. Here the MBS diagnostic and the ROV attitude data are displayed along with the topographic profiles. Figure 4.13 shows the DT101 sweep window where the under ice profiles recreate the 2D topography. The upper part of the figure

displays the instantaneous topographic profile, while below a colour scale represents the intensity of the echo.

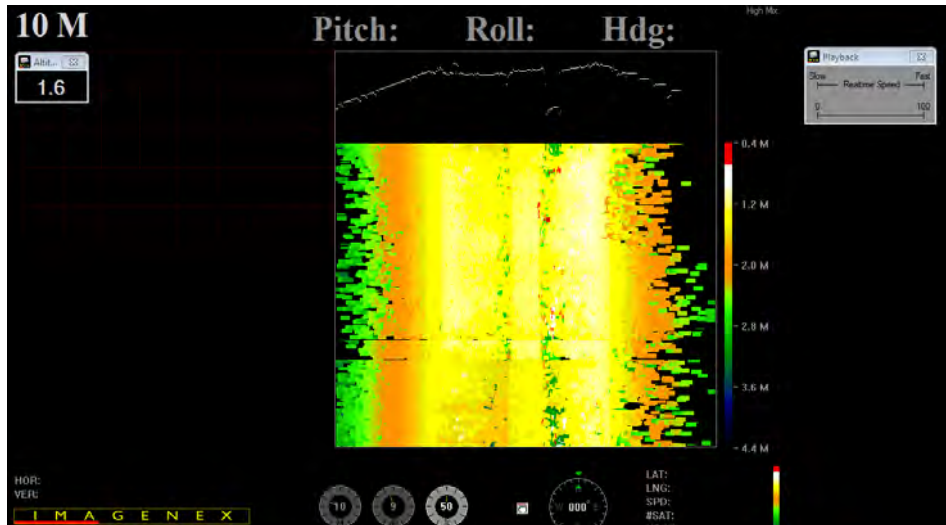


Figure 4.13: Screen capture of the DT101 sweep window for topographic profile display

The navigation software for data recording and storage is “SPOT.ON” (Ocean Modules, Åtvidaberg, Sweden).

This software is also directly involved in the creation of a smooth re-navigation track for the vehicle using the USBL recorded positions. An example of a survey track before and after applying the re-navigation created using SPOT.ON is shown in figure 4.14.

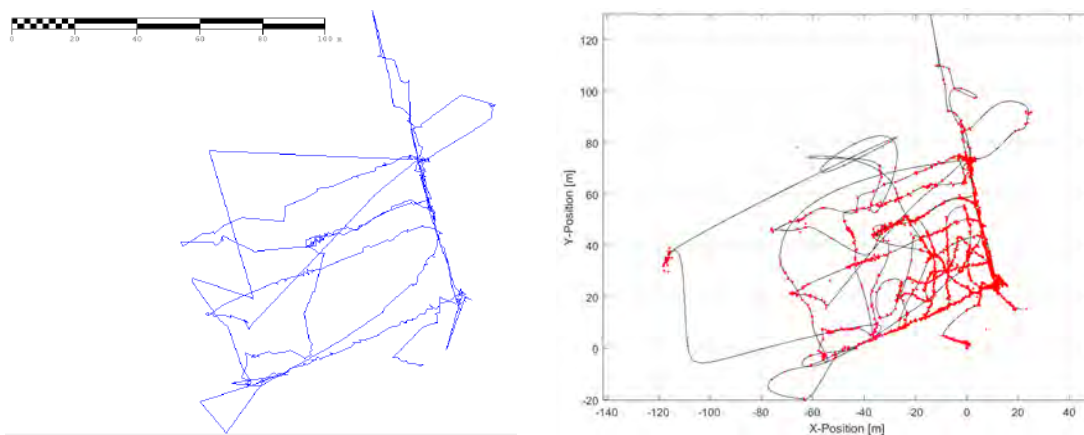


Figure 4.14: Example of survey track before and after applying the re-navigation

To the left the ROV track created using just the raw data from the MBS is displayed. The right part of the figure shows instead the same track after the application of the SPOT.ON re-navigation. Here the

red dots correspond to real positions of the vehicle along its track, as they are recorded by the USBL system, while the black lines represent the most probable route for the ROV, as it has been interpolated with a mathematical algorithm by SPOT.ON.

The MBS data are cleaned and processed using “CARIS Hips” version 10.0 (Teledyne Caris, Falmouth, USA), a screen capture of which is shown in figure 4.15.

The choice of CARIS Hips is because not only it is a complete and very competitive software for topographic analysis, but also because the number of data collected in just few hours of dive is too large to be processed using more conventional software.

In CARIS Hips raw navigation data collected during the survey can be imported and improved by using the renavigation datasets calculated by SPOT.ON together with some MatLab scripts.

A first step of renavigation data cleaning is suggested to avoid outliers. Parameters such as latitude and longitude, roll, pitch, heave and gyro, and a time stamp for each collected data must be included in the data handling process. More parameters, such as sound velocity in water and tide trends, can be included afterwards in order to correct the MBS measurements and increase their accuracy.

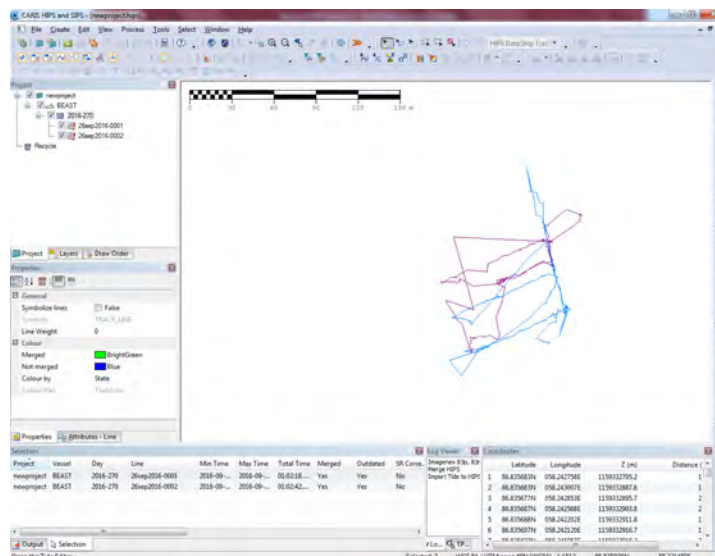


Figure 4.15: Screen capture of the main window of CARIS Hips

When all the required parameters are introduced in the program, a surface can be created and different editors facilitate the cleaning

of it at various levels. At the end of the CARIS data processing and cleaning a topographical map of the sea ice underside for each survey can be created. The sea ice thickness is measured by employing the multibeam sonar dataset that has been used for the topographical survey. The implemented processing workflow is presented in section 4.2.

4.2 Sea ice draft retrieval from multibeam sonar: workflow implementation

Besides the creation of topographic maps of the underside of the sea ice, the second main objective of this work is the implementation of a processing flow to measure sea ice thickness using an upward looking sonar. Such measurements enable the creation of 3D maps that show simultaneously two characteristics of the sea ice: the underside topography and its respective thickness, represented on the map by a colour scale.

This sea ice thickness measuring technique has been developed during the past 50 years. Upward-looking sonars can be attached to moorings (see for example [11]) or mounted on autonomous underwater vehicles (AUVs) ([55]). Some of these studies use CARIS Hips as the dedicated software for the data handling of the upward-looking multibeam sonar. The respective publications do not fully explain the processing workflow so that, despite the similarities, it was necessary in this study to implement an independent new processing workflow to handle the multibeam sonar datasets.

The first issue in implementing a workflow to measure sea ice thickness in CARIS Hips is that it is a software that was developed as a bathymetric tool. In bathymetry the sonar is located above the target with the aim of studying bottom topography, as shown in figure 4.16. Instead in this work an upward looking sonar is used to scan the underside of the sea ice: the position of the sensor relative to the target is reversed and the entire survey configuration setup is rotated by 180°. This complicates the use of this software because many operations must be modified, each function and variable must be tested

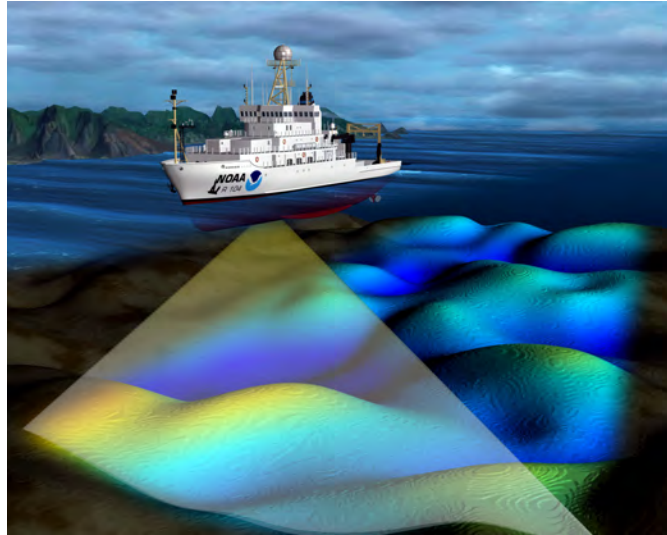


Figure 4.16: **Standard bathymetric survey.** (Image from NOAA coast survey)

and, if necessary, adapted taking into account the inverted configuration. This applies to each step of the standard CARIS data handling process used for standard bathymetry.

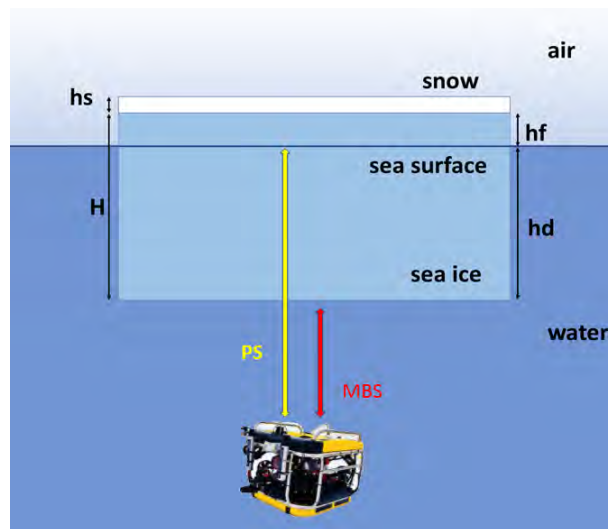


Figure 4.17: **Sea ice draft retrieval from multibeam sonar and pressure sensor measurements**

A straightforward inversion is inhibited by the lack of information given by the Teledyne Caris company to the user about the mathematics behind their software interface.

Using the notation for the sea ice vertical components introduced in section 3.1, figure 4.17 shows a schematic representation of the idea behind measuring sea ice draft using this “inverted bathymetric” con-

figuration.

Sea ice draft can be calculated as the difference between the depth of the vehicle measured by the pressure sensor (PS), and the distance between the ROV and the sea ice underside measured by the multibeam sonar.

4.2.1 Processing workflow

In this section a block diagram is used to schematically represent my newly implemented processing workflow in CARIS Hips for sea ice thickness retrieval from an upward-looking MBS.

Figure 4.18 shows the main flow steps for the multibeam sonar data handling that are involved in the creation of a new project in CARIS Hips. This process ultimately enables measurements of sea ice thickness, hence generating a comprehensive map of sea ice thickness and corresponding underside topography. A brief explanation of the main steps and crucial points of the work flow follows here.

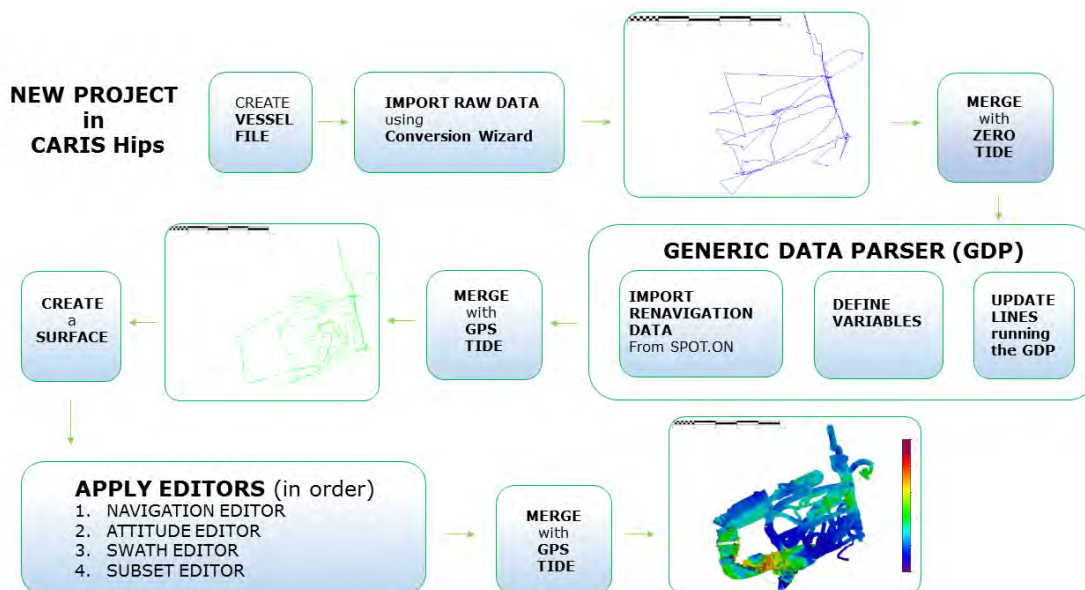


Figure 4.18: Block diagram of the processing workflow for sea ice thickness retrieval from multibeam sonar data

- **Determine a folder structure** Before creating a new project it is necessary to decide its folder structure in CARIS Hips. A folder hierarchy must be followed in order for the software to work properly and to avoid processed data directory problems. In the last versions (from 10.0 onwards) a predefined folders structure

is not mandatory as it used to be in the older versions. However, I have experienced some issues when using a different folder structure in a late version and then opening a project created with the new version in an old one. I therefore suggest to use the folder structure presented in figure 4.19 that has been proved to work for both the old CARIS Hips and Sips and the new CARIS Hips versions.



Figure 4.19: Block diagram of the processing workflow for sea ice thickness retrieval from multibeam sonar data

In any version, each survey project in the “Survey folder” should only have its vessel file and the project created in CARIS during the data processing. Adding different folders to the survey folder should be avoided, as the software could stop working properly due to the presence of raw files or CARIS Hips surfaces within it.

- **Create a new project** When starting a new project in CARIS Hips a project name, vessel file, and date must be created or linked to a previously existing project using the tool “Connect to”. At this point a coordinate reference system and project area extent can also be chosen.

The vessel file must contain all the sensors that are involved in the survey: they must be selected, switched on, and initialized adding the respective offsets. The vessel file used for this work enables the use of gyro, pitch, roll, and sound velocity profile sensors.

At this stage the project environment is ready to be used and the project itself can be opened and modified in CARIS Hips but will

still look empty.

- **Import raw data** The “Conversion Wizard” is the preferred tool used to import raw multibeam sonar data from DT101 into CARIS Hips. This tool also allows the setting of data format, file type, and of the first filters if necessary, like depth and navigation area.
- **Merge data** When new data are added to the project and after any operation every line of the project must be merged. This step saves all the changes applied to the project in order to refresh it by taking the new corrections into account. Merging can be done choosing different options: for our intent the most important is adding a tide. At this stage the data must be merged with no tide.
- **Renavigation datasets and generic data parser** The use of the generic data parser is an important step in the processing workflow. This is the stage when the SPOT.ON renavigation data are accounted for during the surface creation procedure, and when sea ice draft measurements can be achieved by a correct definition of the variables (see also section 4.2.2). The renavigation files created by SPOT.ON and some dedicated MatLab scripts include several parameters, as shown in figure 4.20. These parameters are measured by the ROV sensors, interpolated by the software, and revisited by MatLab scripts.

SpotonTime	Latitude[°]	Longitude[°]	X_Position[m]	Y_Position[m]	Depth[m]	Roll[°]	Pitch[°]	USBL-COG	TimeToPing [s]
2016-09-29T07:36:28.4	86.948223	56.011666	0.000239	-0.000296	0.000000	9.100000	-13.200000	138.733938	0.016998
2016-09-29T07:36:28.905	86.948223	56.011667	0.007407	-0.008991	0.000000	9.400000	-13.300000	136.924615	0.521995
2016-09-29T07:36:29.078	86.948223	56.011667	0.009899	-0.011926	0.000000	9.600000	-13.500000	136.334774	0.694997
2016-09-29T07:36:29.51	86.948223	56.011668	0.016197	-0.019136	0.000000	9.800000	-13.600000	134.856269	1.127001
2016-09-29T07:36:29.892	86.948223	56.011669	0.021856	-0.025347	0.000000	9.900000	-13.600000	133.465583	-1.064005
2016-09-29T07:36:30.457	86.948223	56.011671	0.030380	-0.034195	0.000000	10.000000	-13.600000	131.080932	-0.499002
2016-09-29T07:36:30.759	86.948223	56.011672	0.035009	-0.038735	0.000000	10.000000	-13.500000	129.564269	-0.197002
2016-09-29T07:36:31.033	86.948223	56.011672	0.039253	-0.042726	0.000000	9.900000	-13.500000	127.997365	0.076996
2016-09-29T07:36:31.537	86.948223	56.011674	0.047164	-0.049719	0.000000	9.700000	-13.400000	124.535154	0.580997
2016-09-29T07:36:32.034	86.948223	56.011675	0.055096	-0.056125	0.000000	9.500000	-13.200000	120.226766	1.077997

Figure 4.20: Extract of a renavigation dataset

In order to calculate sea ice draft in CARIS Hips it is necessary to define several parameters from the renavigation data: a file header, date, time stamp, sound velocity, latitude and longitude,

gyro, pitch, roll, GPS height and GPS Tide. GPS tide and height do not correspond to their physical quantities of course, however they are part of the method to retrieve sea ice draft.

When starting the workflow it is assumed that the renavigation dataset has already been corrected in case of sensors malfunctioning or scripts errors. These issues can lead to the collection of values that are out of their range, as it is commonly found for many of the ROV attitude data such as pitch and roll.

At the start of this work for example one of the main problems with the renavigation dataset was a variable time shift between the softwares and among the different surveys. The time stamps of the recording softwares did not match with that of the processing software, due to some synchronisation error between SPOT.ON and the monitoring computers especially after a time zone change. The issue was discovered in this work during the processing of the data and it has now been solved.

Another parameter that must be modified before using the renavigation file is the position offset between the sensors. As already mentioned sea ice draft is calculated as the difference between the pressure sensor and the multibeam sonar measurements. As these sensors are not positioned at the same height, their offset must be taken into account to avoid errors in calculating the sea ice thickness. This can be done by shifting the depth measured by the pressure sensor in the renavigation data sheets, or by accounting for it in the MatLab script.

The first renavigation files used included negative time to ping values. As a consequence of the SPOT.ON raw data interpolation new time to ping are created, but they are just fictional time derived from the software calculation. A MatLab script is used to decide which new time to ping matches best the real ones measured by the transducer. Negative values of time to ping in the renavigation files were caused by a partially wrong definition of the time to ping function in the existent script and the issue has now been corrected. A threshold is also set in order to remove the time to ping that protract for too long, as they might be the

result of noise or the reflection of a different signal.

Sound velocity is another parameter that has to be declared in the GDP and accounted for in the renavigation process. As mentioned in section 3.2.1, SVP depends on temperature, pressure, and salinity. The values have been extrapolated from the data collected with the CTD by the oceanographers. Although there is an option to add a complete sound velocity profile, in this work the sound velocity is set equal to the constant value of 1437 m/s, for the reasons explained earlier.

- **Create a surface** After merging the data using the option “GPS Tide”, a topographic surface of the survey is created. To increase this process efficiency I suggest to modify the surface using the various dedicated editors following the order presented in figure 4.18. Spatial resolution and depth filters can also be decided at this stage.

Further details about the workflow can be found in my brief user manual “CARIS Hips brief manual for sea ice draft measurements with DT101” in Appendix B.

4.2.2 Use of the tide tool as an escamotage for draft measurements

A thought out use of the “Tide” tool enables the software to work in a bathymetric inverted configuration. This tool is used in bathymetry to correct for tide observations by subtracting tide values from the sounding measured depth.

As previously mentioned, in the “inverted bathymetric” configuration and with the sensors mounted on the ROV, the sea ice draft can be calculated as the difference between the depth of the vehicle and the multibeam sonar distance from the ice underside.

This can be achieved in CARIS Hips by setting in the GDP the depth measured by the pressure sensor as both GPS Tide and GPS Height. GPS tide is calculated as the subtraction between the GPS Height and a given height that can be added as a single value or as a tide profile. To retrieve sea ice draft this height is set to zero and data are merged first with no tide and then with the GPS Tide tool. As both the PS measured depth and the MBS ice distance are affected by the same

ROV depth changes, there is no need for further corrections.

This mathematical artifice enables the calculation of the sea ice draft using the inverted bathymetry configuration.

The only issue is that all the draft values will have opposite signs as a consequence of the use of bathymetry dedicated tools in an inverted configuration. Hence, a sign conversion should generally take place before surface data exporting and handling in different programs.

4.3 Multibeam sonar spatial resolution calculation

One of the aims of this thesis is to improve the performance of the upward-looking multibeam sonar system for future expeditions.

It is therefore important to know the best feasible resolution of the multibeam sonar, in order to be able to evaluate which features can be detected and displayed during a survey and to compare the performances of this system with other methods for sea ice thickness measurements.

In this thesis the size of the smallest object detectable by the multibeam sonar and the level of detail that can be achieved for the maps of the ice underside are investigated for the first time, for this particular system.

Knowing the multibeam sonar resolution value and its dependance on the survey parameters before the start of a survey enables the choice of a working depth and speed that give the best results for a certain study.

To understand how to determine the resolution of the multibeam sonar it is important to remember how the MBS creates the acoustic signal and how this is processed by the dedicated software, as the resolution of the sonar rather depends on the processing than the physical device characteristics. As already mentioned, the MBS generates acoustic pulses in the shape of a fan that can be imagined as composed of a certain number of beams along the swath, forming a “profile”. The number of beams can be decided by the operator, depending on the software specifics and on the aim of the survey, as discussed in the following. The fan scans the underside of the ice while the ROV moves

underwater and it can be displayed live on the DT101 screen in order to give a first idea of the ice topography while the navigation is still taking place. Each received pulse is later displayed on the MBS data handling software CARIS.

To begin with, the MBS spatial resolution is dependent on the direction of the vehicle: the along-track resolution is defined as the resolution along the direction of motion of the vehicle (that coincides with the sensor motion as well), in our case along the ROV track; across-track resolution instead is defined perpendicular to the direction of motion. Figure 4.21 shows a screenshot of a MBS survey partial track visualised in CARIS Hips.

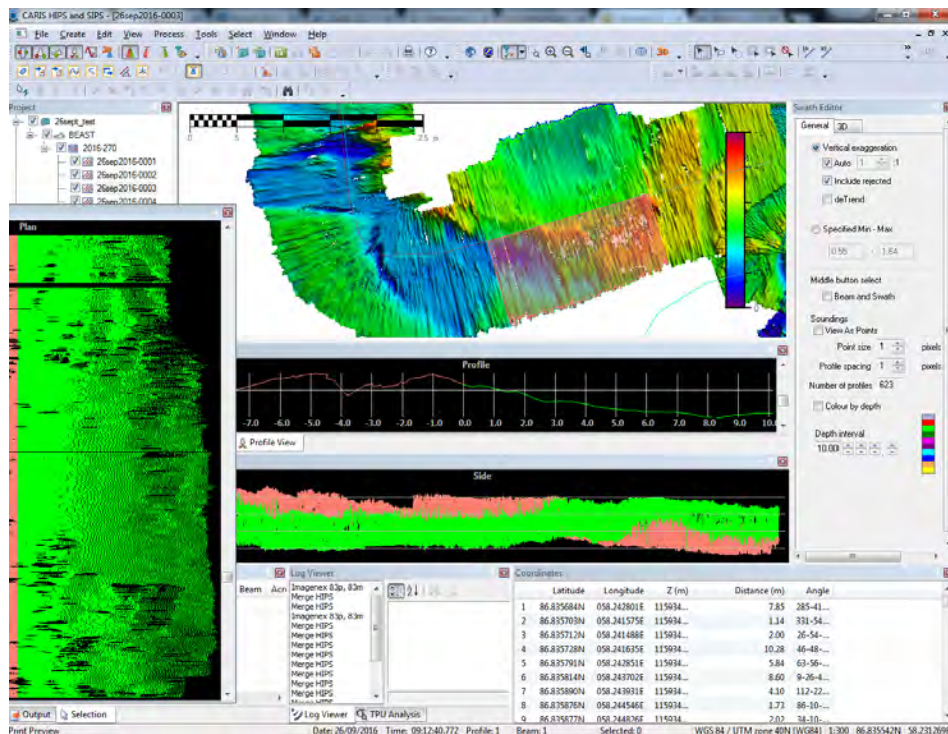


Figure 4.21: Screenshot of the graphic interface of CARIS Hips during data handling of the MBS for spatial resolution study

The top of the figure shows part of a survey map with a highlighted set of profiles, easily recognisable in green and pink. This choice of colours in CARIS is not random, instead it is inspired by navigation, where green and red are used to indicate the side of the vessel related to its direction of motion, where green is right and red is left. Following this convention, the direction of motion of the ROV along the map tracks displayed in CARIS Hips is always easily definable.

The same set of profiles can be visualised in different view modes, some of them shown in the bottom part of figure 4.21. Top view, side view, and profile view are especially useful for data cleaning.

Using the Navigation and Attitude editors in CARIS, and the multi-beam control software DT101, I could extrapolate all the parameters needed to define the MBS spatial resolutions.

In CARIS I measured the distance Δx covered by the ROV during the scan of the part of the track that coincides with the profiles highlighted, the time Δt taken for this displacement, and the width W of the swath. Using these quantities I then calculated the velocity v_{ROV} at which the vehicle was moving.

I also checked the renavigation data to find the depth d_{ROV} of the ROV during the same part of the survey, and counted the number N of profiles highlighted, while the pulse repetition frequency PRF (also called “ping rate”), that is the number of pings that can be counted during a certain time interval, can be calculated using the data displayed in DT101. The number of beams n in each fan can be changed during data acquisition in DT101 but during this pilot project this number was kept constant as set by default.

In this project the **across-track spatial resolution** R_{across} is defined as the swath width divided by the number of beams it is composed of as shown in equation 4.1.

$$R_{across} = \frac{W}{n} \quad (4.1)$$

The **along-track spatial resolution** R_{along} depends on the distance travelled by the ROV and on the number of profiles there contained, as shown in figure 4.2.

$$R_{along} = \frac{\Delta x}{N} \quad (4.2)$$

The along-track resolution depends therefore on the speed of the ROV and the ping rate of the multibeam sonar, as both parameters affect the number of profiles per track unit length.

An estimate of the MBS footprint can also be calculated. It is a function of the distance between the ROV and the ice, hence of the vehicle depth and of the underice topography. As a consequence, the footprint is expected to vary according to the type of survey. As mentioned in section 3.2.2 the footprint is spatially defined by the intersection between the two swaths that in this study have the same dimensions. Hence the footprint surface is here given by the square of the minor width of the swath. This quantity is not constant though, as it depends on the depth of the vehicle. It can be calculated by using the distance between the ROV and the sea ice, and the MBS angular aperture given in the DT101 specifics.

4.4 Sea ice draft and snow depth measurements from GEM-2 datasets

There were two GEM-2 related datasets available for this thesis work. The values of the first dataset consisted of the sum of snow depth and ice thickness, as they are directly measured by the electromagnetic device. The other dataset values represented bare sea ice thickness. These values were formerly calculated by subtracting in each station the snow depth values collected by the Magna Probe from the GEM-2 measurements.

As previously explained, snow determines important implications for sea ice growth. It is therefore necessary to retrieve the snow depth values for the three stations in order to use the FDD model. In this model snow depth is used to calculate the proportionality parameter α between sea ice thickness and snow depth, as presented in section 3.6.2. Therefore I subtracted the bare sea ice thickness to the sum of snow depth and ice thickness using MatLab, and found the values of snow depth sampled by the Magna Probe. A direct subtraction is possible since the GEM-2 and the Magna Probe are operated along the same survey track, as explained in section 3.4.

Given the large influence that the presence of a snow layer has on sea ice thickness growth, I found that it was worth checking if there was any correlation between snow depth and sea ice thickness values.

Hence I computed a regression plot for each station to investigate such potential correlation. As the resultant coefficients of determination R^2 were all of the order of 1% no clear correlation is found for any of the three stations between snow depth and sea ice thickness. All the plots and R^2 values are presented in Appendix C.

Sea ice thickness datasets were later converted into sea ice draft values. This enables the comparison between the GEM-2 and the MBS collected measurements. This conversion is achieved by using the isostatic model for sea ice explained in section 3.5. Following the notation given in section 3.1, I have used: the GEM-2 data without snow depth as sea ice thickness H ; the snow depth values measured by the Magna Probe and retrieved by subtracting the two GEM-2 datasets (as explained before) as h_s ; and the densities of the materials are set equal to the values found in recent literature ([2]) as follows:

Sea ice density: $\rho_i = 917 \text{ kg/m}^3$

Snow density: $\rho_s = 324 \text{ kg/m}^3$

Sea water density: $\rho_w = 1025 \text{ kg/m}^3$

Chapter 5

Results

5.1 Multibeam sonar resolution

5.1.1 Across and along-track resolution

Following the process described in section 4.3 it is possible to calculate the spatial resolution of the multibeam sonar both along and across-track. The resulting numerical parameters used for such calculations are presented in table 5.1.

Table 5.1: **Example of numerical values extracted from survey datasets for MBS spatial resolution calculation**

d_{ROV} (m)	v_{ROV} (m/s)	Δx (m)	Δt (s)	W (m)	N	n	PRF (Hz)
3.5	0.4	20	55	18	620	480	12

The resulting spatial resolutions referred to the water depth range are:

Across-track resolution: $R_{across} = 0.04$ m

Along-track resolution: $R_{along} = 0.03$ m

As for the footprint calculation, the first rough estimate resulting from this pilot project study is the measure of the common ensonified area of the transmitted and received swath, as mentioned in section 4.3. The swath width, and therefore the footprint size, increases with the vehicle depth as a consequence of the fan conical

shape, according to the following relation:

$$W = 2d_{ROV} \tan \frac{\theta}{2} \quad (5.1)$$

where θ represents the opening angle of the multibeam sonar fan. As previously described, the MBS transmitter and receiver swaths are wide across-track and narrow along-track. The MBS opening angle across-track is given in the DT101 specification sheet and is equal to 120° for both the transmitter and receiver fan. This angle, according to formula 5.1, defines a swath width along this direction around 3.5 times larger than the vehicle depth.

The footprint area is defined by the along-track swath width on each side. The swath width in this direction is determined by the smallest MBS fan angle, that has a nominal width of 3° . Using formula 5.1, the footprint side length is around 0.05 times the depth of the vehicle.

Given the strong dependance of the footprint size on the ROV depth, table 5.2 gives some examples of MBS footprint areas calculated for potential future surveys at various diving depths.

Table 5.2: DT101 calculated footprint size for different diving depths

Vehicle	Survey depth (m)	MBS fan angular aperture (degrees)	footprint (m) \times (m)
ROV	3.5	3	0.18×0.18
ROV	5	3	0.26×0.26
ROV	10	3	0.52×0.52
AUV	20	3	1.05×1.05
AUV	45	3	2.36×2.36

These depth values are chosen among the different survey depths of the ROV dives in this project, and some examples of values found in literature for both ROVs and AUVs for sea ice underside topographic surveys ([99], [36], [29]).

5.1.2 Vertical resolution and ice thickness uncertainty

The MBS vertical resolution is the parameter that must be taken into account when calculating sea ice draft and thickness uncertainties.

For this calculation it is also necessary to include the resolution of the pressure sensor: as previously explained, sea ice draft is calculated by subtracting the distance between the vehicle and the ice underside, and the depth of the vehicle referred to the water surface level. Therefore, to retrieve the vertical uncertainty of any thickness measurement derived using this method both the multibeam sonar and the pressure sensor vertical resolution must be taken into account. These two quantities propagate their uncertainties into the expression for the draft and thickness retrieval, and contribute together to the total vertical uncertainty that affects the sea ice thickness measurements of this study.

The vertical resolution of the multibeam sonar given in the specification datasheet is equal to 0.02% of the value of the range. In our study, for a typical range of around 5 m the resulting vertical resolution is then 10^{-3} m. Instead, the pressure sensor has a resolution of only 0.1 m, that is constant at any depth. Hence, a propagated total uncertainty of around 0.1 m affects the measurements of sea ice thickness and gives the vertical resolution of the complete system formed by the multibeam sonar and the depth sensor. In conclusion, even if the vertical resolution of the multibeam sonar is high, the use of the pressure sensor as a second instrument for the retrieval of ice thickness decreases the final total vertical resolution. Therefore, the quality of the results of this study for sea ice thickness retrieval using a multibeam sonar are affected by the poor resolution of the pressure sensor.

5.1.3 Maximising the multibeam sonar resolution

Improving the spatial resolution of the multibeam sonar is a key goal for future surveys.

The two horizontal resolutions and the vertical resolution of the system MBS/pressure sensor used for sea ice draft measurements can be maximised by adjusting the different parameters involved in their definitions as follows:

- For the across-track spatial resolution it would be ideal to use a larger number of beams for the swath. However, physical properties such as the size of the instrument limit the number to a

maximum of 480 in our case, hence no better across-track spatial resolution can be achieved in this way.

The other parameter that can be optimised for a higher across-track resolution is the swath width. The swath width increases with the vehicle depth, as a consequence of its geometrical shape, as shown in formula 5.1. A smaller width would lead to a better resolution, so this means that the ROV should be driven at shallow depths in order to minimize the swath size and improve the across-track resolution.

This solution however is a compromise as the vehicle must be kept at safe distance from the ice underside to avoid collisions and it must still collect enough data to create a good quality map in an acceptable amount of time. Since a close distance between the vehicle and the sea ice determines a narrow swath, at the same time a smaller area of the survey is covered per unit of time. This causes a considerable increase in the time that is necessary to collect a large amount of data that enable the creation of a continuous map without gaps in the data. A second compromise must therefore be found between resolution and survey time, otherwise a quicker survey would create irregular maps. More about these and other compromises are presented in the next section (5.1.4).

- The along-track spatial resolution can be improved by increasing the number of samples, that is by increasing the number of profiles N . This can be achieved using a higher pulse repetition rate. This quantity strongly depends on the data processing method as it is explained in section 5.1.4, although the maximum ping frequency rate is set by the hardware specifications to 20 Hz. The second parameter that can be changed to maximise the along-track resolution is the speed of the vehicle.

Driving the ROV at low speed decreases the distance Δx travelled in a set amount of time, improving the along-track spatial resolution. A slow survey can however oversample the area, collecting a large amount of redundant data that slow the software for the data acquisition down. A compromise between speed and the amount of data collected is therefore critical to achieve an efficient survey.

Working on both the parameters involved in the calculation of

the along-track resolution aims to increase the amount of profiles collected per unit distance.

- The sea ice draft maps created using the datasets measured by the MBS and the pressure sensor can also be improved in terms of vertical uncertainty. Although the MBS vertical resolution is higher than that of the GEM-2 (see section 5.1.2) the combined use with the pressure sensor for sea ice draft retrieval results in poor vertical resolution maps. To improve the vertical uncertainty that influences draft measurements it is suggested to measure the depth using the CTD package mounted on the ROV instead of using the pressure sensor. In fact, the CTD has a nominal vertical resolution of 0.002% of the range for pressure measurements. Hence, converting the CTD pressure measurements into depth would enable the creation of sea ice draft maps with higher resolution than those created using the pressure sensor.

5.1.4 Trade-offs

As previously mentioned, maximizing both lateral resolutions causes issues in terms of the duration of the survey such as decreasing the speed of the vehicle to achieve a higher along-track resolution, or diving in shallow water to decrease the swath width for a higher across-track resolution.

Compromises must be found between high resolution sea ice draft maps and an appropriate survey duration.

Depending on the available survey time for each station and on the desired quality for the draft maps, it is suggested to decide the desired resolution before the survey starts. Key points such as the amount of time to spend on the study of a certain area, which features are worth resolving, and the possible issues in terms of data processing time when resolution is improved must be considered.

As an example, I calculated the values to be set for the ROV and the MBS for a potential upcoming expedition in order to achieve a value of 0.01 m for both resolutions. This number is a feasible value that I chose to calculate some practical estimates to give an idea of the order of magnitude of the parameters that should be set to reach

such level of resolution. This value equals the maximum size for the spacing between the dendritic arms of the skeletal layer ([45], [52]) and it represents the lower limit of sea ice ruggedness found in one of the latest surveys of the sea ice underside ([55]). A spatial resolution of 0.01 m would therefore enable a very detailed study of sea ice texture.

- To achieve an across-track spatial resolution of 0.01 m the only parameter that can be changed is the distance of the ROV from the ice, as already discussed in section 5.1.3. Inverting the formula used to calculate the resolution and inserting this resolution value leads to a distance of 1.4 m, hence the ideal depth at which the vehicle should work to achieve an across-track resolution of 0.01 m is very close to the sea ice underside.
- The along-track spatial resolution can be changed by adjusting two free parameters.

The first option is to decrease the distance Δx traveled by the vehicle in a certain amount of time while keeping the number of profiles constant. This can be done by slowing the ROV down while keeping the ping frequency constant.

To achieve an along-track resolution of 0.01 m, this method would lead to a length of the survey track of only 6.2 m in 55 s, instead of 20 m as before. The resulting ROV speed to be set to achieve the desired resolution corresponds to only 0.1 m/s (0.2 knots) instead of the actual speed of this survey of 0.4 m/s (0.8 knots). This would of course lead to longer survey times, an issue of great importance in the harsh polar environment.

Moreover, speed has an impact in terms of navigation as well: a fast navigation helps the stability of the vehicle, thus a slow ROV is more subject to under ice currents and it is more difficult to drive it on a straight line.

The second option to achieve an along-track resolution of 0.01 m is to change the ping rate, while keeping the speed of the ROV constant. With a speed of 0.4 m/s and in 20 m path the necessary number of profiles to achieve such resolution would be 2000. However, this approach creates data processing complications which are described in detail in section 5.1.5.

Table 5.3 shows the survey depths and speed values suggested in order to create draft maps with both lateral resolutions equal to 0.01 m, and to achieve the high spatial resolution value of 0.05 m found in literature for a similar sea ice underside topography and draft measurement survey ([55]). With such resolution fine-scale sea ice textural features such as brine drainage channels can be identified.

Table 5.3: **Examples of suggested depth and speed values to achieve spatial resolution values of 0.01 m or 0.05 m**

R_{across} (m)	R_{along} (m)	Depth (m)	Speed (m/s)
0.01	0.01	1.4	0.1
0.05	0.05	6.9	0.6

5.1.5 Pulse repetition frequency limitations

As mentioned in the previous section, to improve the along-track resolution without slowing down the survey the number of ping per second could be increased. This would solve the problem of a “slow survey” with all the complications linked to it.

During this thesis work it was confirmed that changing this parameter is strongly dependent on the data processing that takes place during the “live” streaming of the survey collected data. The DT101 data acquisition and processing flow chart is displayed in scheme 5.1.

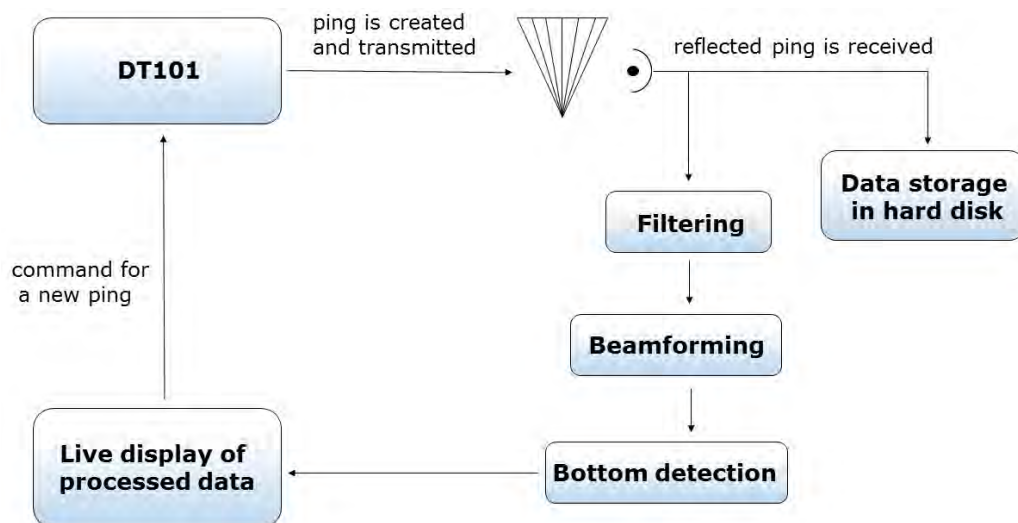


Figure 5.1: **DT101 data acquisition and processing flow chart**

During a survey it is indeed possible to stream live on DT101 the area

scanned by the multibeam sonar. The DT101 software commands the creation and transmission of a pulse to the MBS. When the reflected echo is received and collected, the software does two things at the same time: it stores the file as raw data in a hard disk, and it displays the processed data live on a screen.

While the first action is almost immediate, the second one takes some time, as the data collected go through a process of filtering, beam forming, and bottom detection. This enables the “live” display on through the DT101 interface of the MBS scanned area, in the form of a series of white points that represent the bottom profile of the sea ice, and a colour map that represents the intensity of the received signal from the ice underside.

After the data has been displayed, the program commands the sonar to create and send a new ping so that the loop can start again.

The ping frequency is therefore linked to the data processing and live visualisation time, because the sonar will not send a new ping unless the storage and display of the previous ping data is concluded. As a consequence, in order to increase the ping frequency it is necessary to limit the processing time for the live display of the data. It is therefore suggested to use a lower number of beams during the beam forming step for live visualisation. This would lead to a quicker visualisation of the data and allow for a higher ping frequency.

The MBS technical sheet shows a maximum PRF value of 20 Hz. During this work it was found that the ping rate used during the PS101 surveys is of only 12 Hz. This is most probably due to the fact that the number of beams used during the live display is set equal to the maximum value available on the technical sheet.

Although this choice improves the displayed image quality and therefore is useful during navigation, it slows down the DT101 data processing and inhibits the creation of high resolution maps.

To conclude, in order to achieve the highest PRF possible for the next campaigns it is suggested to use the lowest number of beams possible during the live part of the survey. This approach should speed up the beamforming process and the live display step. Choosing 120 beams

instead of the 480 used before this work should make a substantial difference in terms of data processing time and consequently allow for a higher pulse repetition rate.

The suggested use of a lower beam number during the live display stage of the survey does not affect the quality of the data acquired during the survey. This is because the raw data stored in the hard disk are independent from the beamforming, and are not influenced by the settings of the display stage.

After the survey visualisation takes place in playback. At this stage a new process of beamforming takes place, hence it is possible to set a higher number of beams. Setting a higher number of beams at this stage does not slow down the survey and improves the map spatial resolution.

In fact, setting 480 beams only in playback would leave the across-track resolution as high as it used to be for the past surveys, and at the same time it would increase the number of profiles per unit time and space, hence improving the along-track resolution.

5.2 Sea ice underside three-dimensional topographic maps

In this section the topographic maps of the sea ice underside obtained by using an upward-looking sonar mounted on a ROV are shown.

As explained in the dedicated section, the setup of the instruments is inverted with respect to standard bathymetry and enables a survey of the sea ice from below it. A map of the sea ice underside can be created by using the software CARIS Hips to handle and display the collected data.

Figure 5.2 shows a screenshot of CARIS Hips display window for the visualisation of topographic maps.

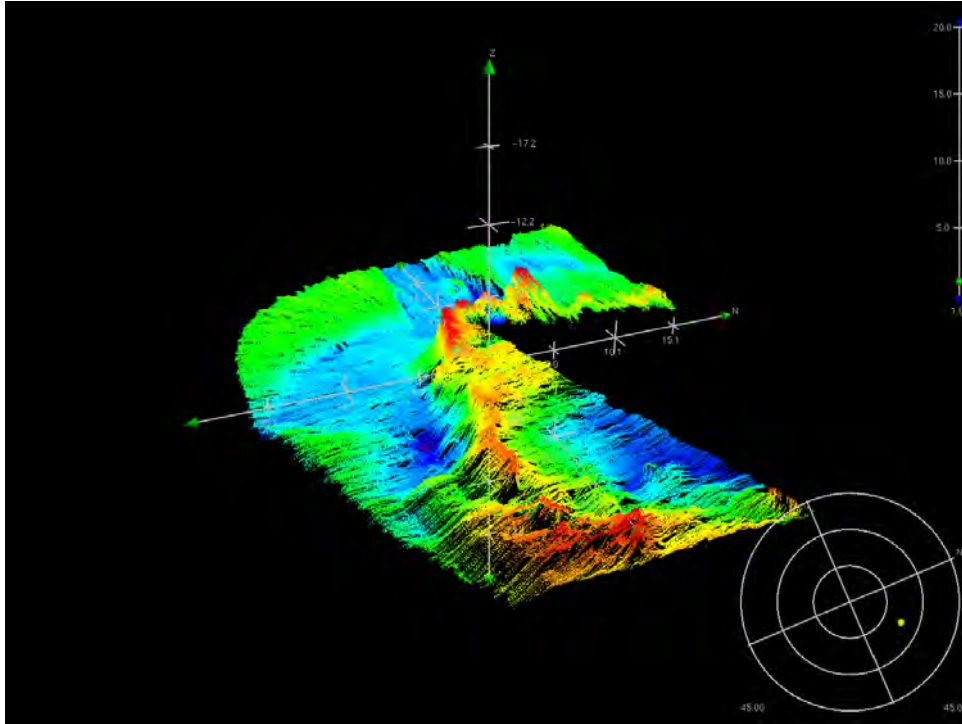


Figure 5.2: **CARIS Hips display window for topographic map visualisation. The map is rotated by 180° about the vertical axis for ease of visualisation**

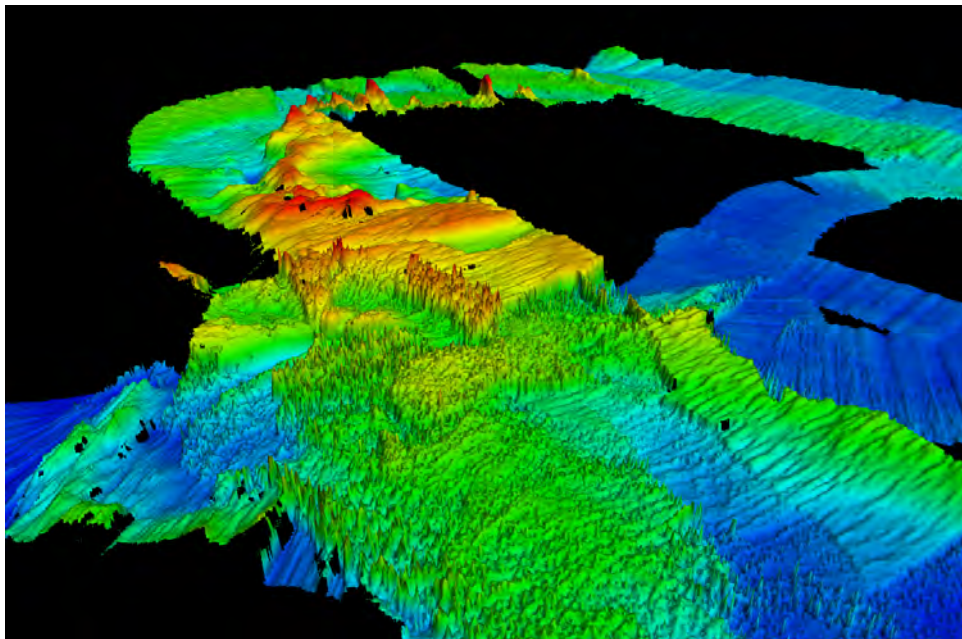


Figure 5.3: **Three-dimensional view of part of the survey of station 26th September. The map is rotated by 180° about the vertical axis for ease of visualisation**

Figure 5.3 and 5.4 show details of the 3D high resolution maps created for the station 26th September. In both cases the whole map is rotated by 180° about the vertical axis for ease of visualisation. This display

method is more intuitive as it derives from the standard representation of features in topography.

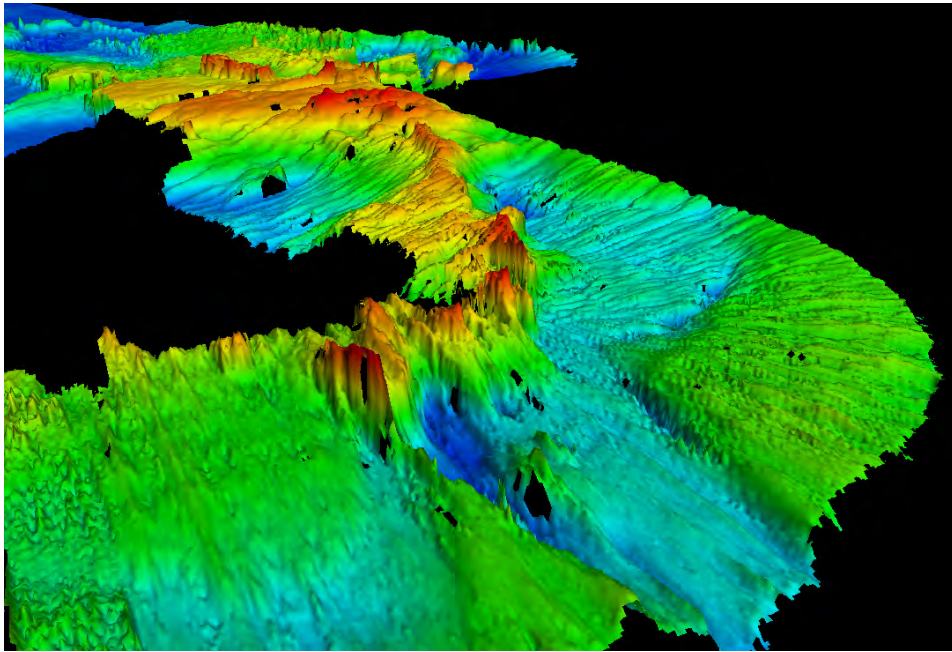


Figure 5.4: **Partial view of the survey of station 26th September. The map is rotated by 180° about the vertical axis for ease of visualisation**

The colour map displayed is of common use in bathymetry, where warm colours represent target areas that are closer to the sensor. Therefore, in this study warm colours represent the sea ice areas that extend more below the sea surface, hence the thick regions of sea ice (see section 5.3). A clear distinction is visible in both figures between deformed ice (in red and orange) and level ice (in blue).

In order to validate the topographic maps resulting from the multibeam sonar data handling, I used the underwater cameras videos: thank to the comparison of both the time stamps and the position of the ROV recorded by different softwares it is possible to compare the topographic maps to the sea ice features in the videos. Figure 5.5 shows two examples of this comparison.

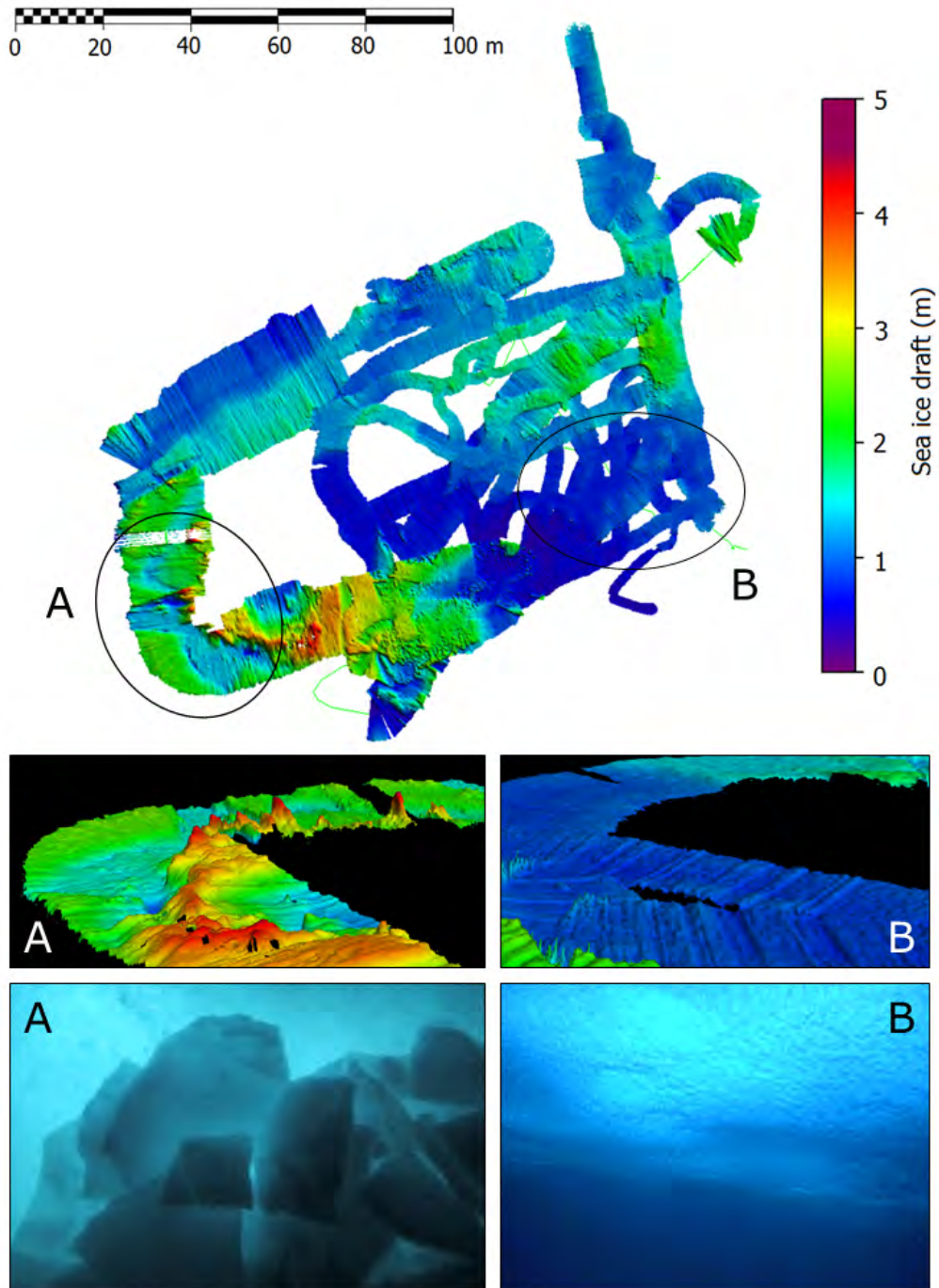


Figure 5.5: Topographic map and image validation from upward-looking camera. The upper part of the figure shows the top view of the sea ice underside topographic map created for station 26th September. Two areas of interest are marked and their respective 3D view displayed in CARIS Hips is presented below. For both areas a picture of the sea ice underside taken by the ROV upward-looking camera when diving under the area of interest is displayed below the corresponding CARIS Hips image. Figure A shows a ridge, while figure B displays a region of thin level ice

5.3 Sea ice draft distribution maps

In this section the sea ice thickness measurements collected by the multibeam sonar and by the electromagnetic device are analysed. Two distinct sets of maps are created for each station. One set is created using the software CARIS Hips and shows the measurements collected by the MBS, while the other is created using MatLab and shows the data collected by the GEM-2. The reason for the use of two softwares is because MatLab is not suitable to handle MBS data due to the large amount of time and memory that it would require. Therefore for this purpose it is more efficient to use the dedicated software CARIS Hips that can process large amount of data in a relatively short time.

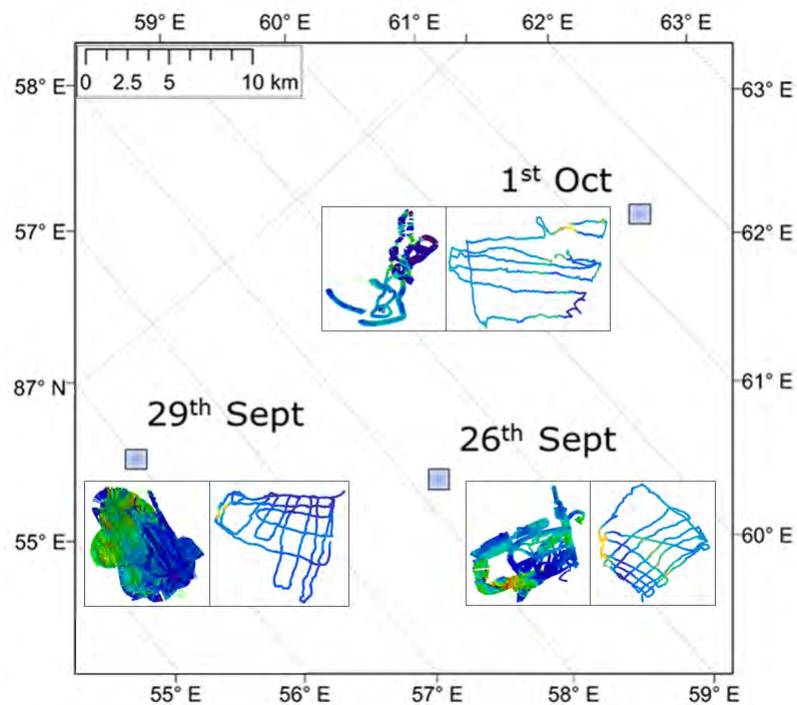


Figure 5.6: Overview of the three station surveys with MBS and GEM-2 corresponding maps

An overview of the three station surveys is given in figure 5.6 for orientation in the text. For each survey both MBS and GEM-2 maps are displayed, respectively to the left and to the right.

5.3.1 Sea ice draft distribution maps from multibeam sonar

The use of the upward-looking multibeam sonar for under-ice surveys together with the new processing flow implemented in this thesis (described in detail in section 4.2) enables the creation of the 3D topographic maps presented in the previous section. Each map created in CARIS Hips shows the sea ice underside 3D morphology representing the corresponding sea ice draft distribution by a colour scale.

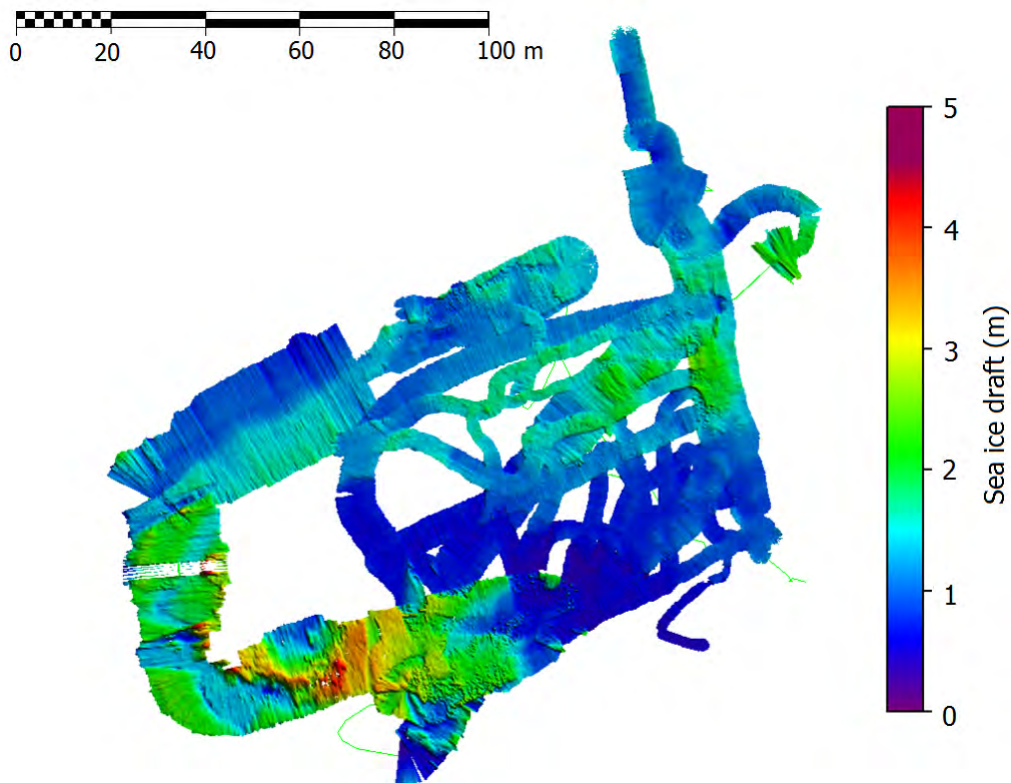


Figure 5.7: Station 26th September: CARIS Hips surface of the sea ice draft distribution measured by the multibeam sonar

The maps produced in CARIS Hips are shown in figure 5.7 for the survey 26th September, 5.8 for the 29th September, and 5.9 for the 1st October. They display two-dimensional aerial views of the actual 3D images produced with the software, examples of which have been presented in section 5.2.

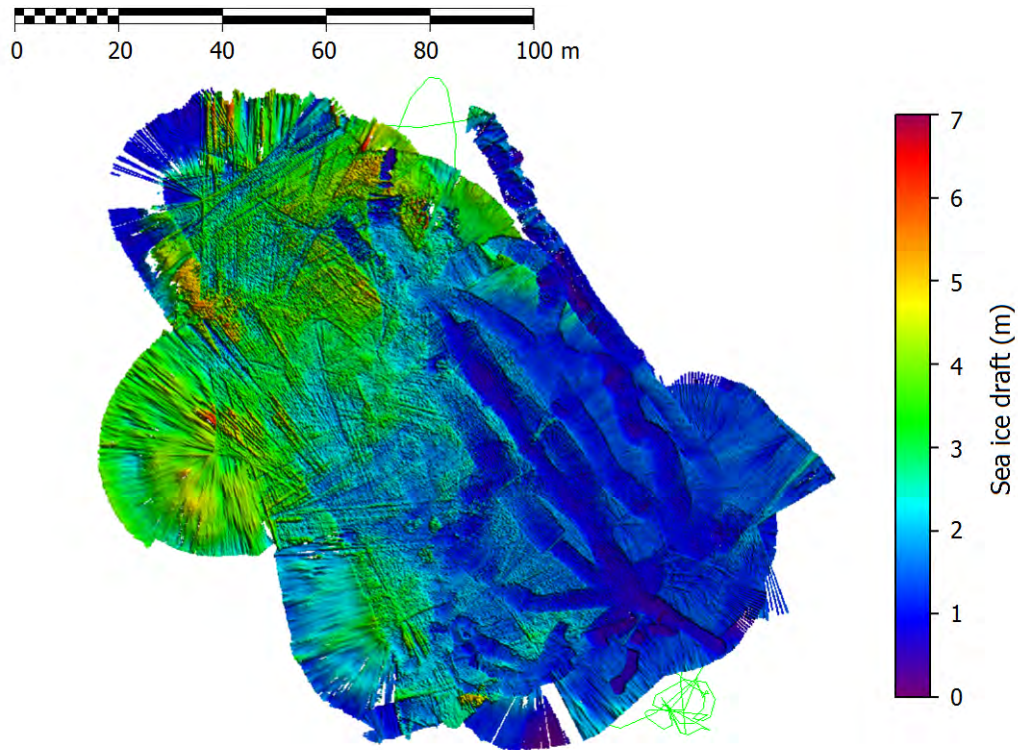


Figure 5.8: Station 29th September: CARIS Hips surface of the sea ice draft distribution measured by the multibeam sonar

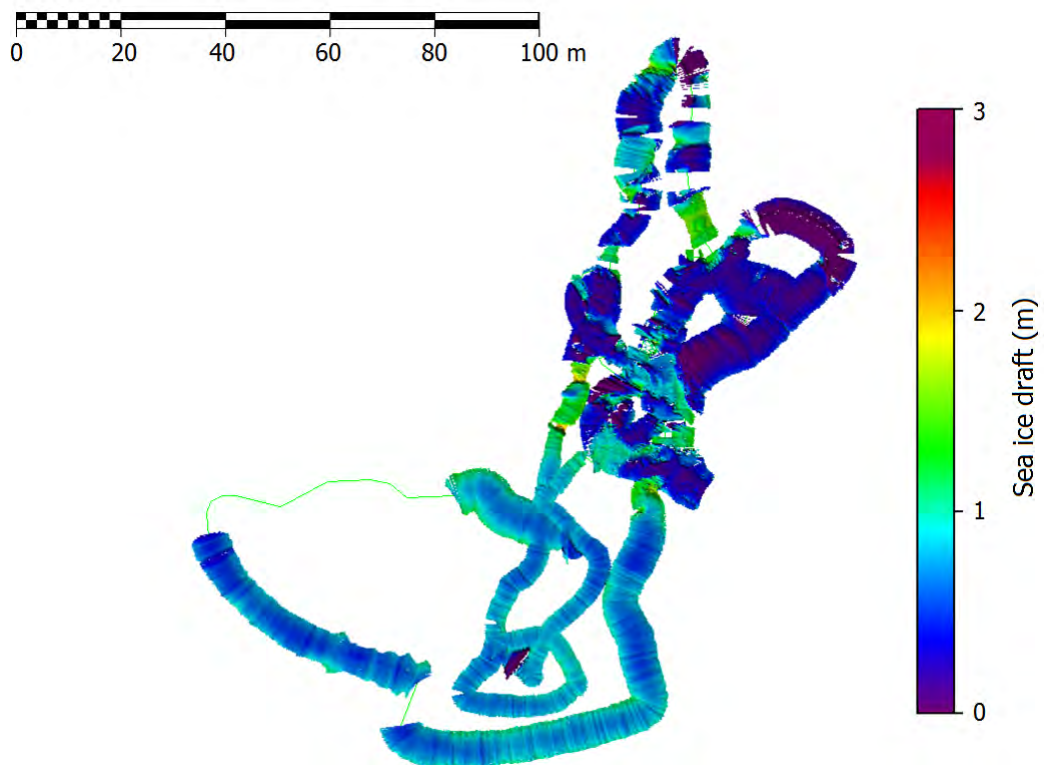


Figure 5.9: Station 1st October: CARIS Hips surface of the sea ice draft distribution measured by the multibeam sonar

The map colour scale represents sea ice draft values, with blue representing thin level ice, while red represents thicker regions of sea ice. The exact values of the colour scale vary from station to station according to the local sea ice thickness distribution for that specific survey. However, the colour violet always represents sea ice thinner than 0.1 m, that corresponds to the vertical uncertainty affecting the draft measurements. It can also represent open water but, apart for the ROV entrance hole, no open water surface was found in any of the three surveys.

A distance bar is also displayed above each map to represent the extent of the survey, usually of the order of 100 m maximum on each side.

5.3.2 Sea ice draft distribution maps from GEM-2

The GEM-2 maps show the three station distributions of sea ice draft collected during surveys above the ice.

These maps are created using the software MatLab, as the amount of data to be processed with the EM method is significantly smaller than for the multibeam sonar case. Moreover, MatLab is an accessible and powerful software to work with.

As already explained in section 4.4, retrieving the values of sea ice draft from the data collected by the GEM-2 takes some computational steps, as it is necessary to convert the collected raw data of snow depth and sea ice thickness into sea ice draft.

The figures presented in this section show the different stages of this conversion process:

- Figure 5.10, 5.11, and 5.12 represent the data as they are directly collected by the electromagnetic device. The maps show the distribution of the sum of **sea ice thickness and snow depth** along the GEM-2 and Magna Probe survey tracks;

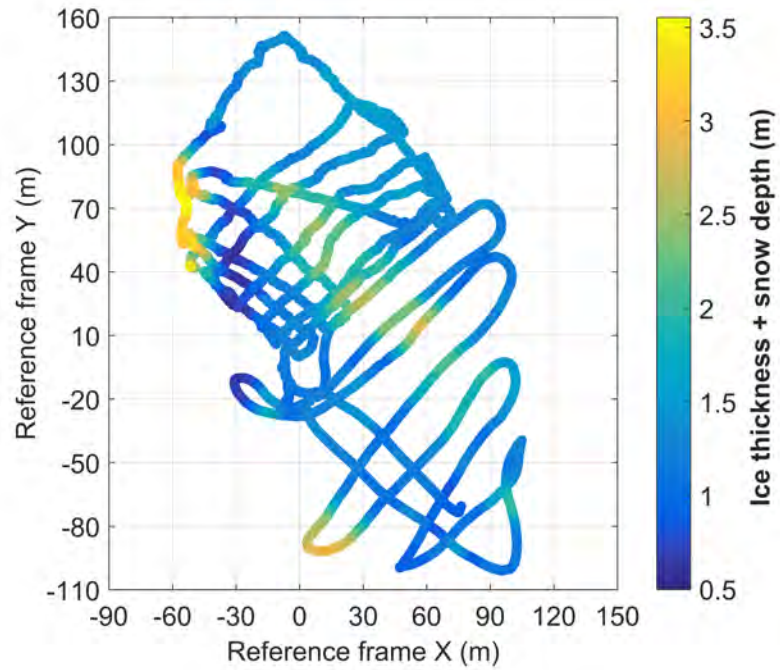


Figure 5.10: Station 26th September: sea ice thickness and snow depth distribution map measured by the GEM-2

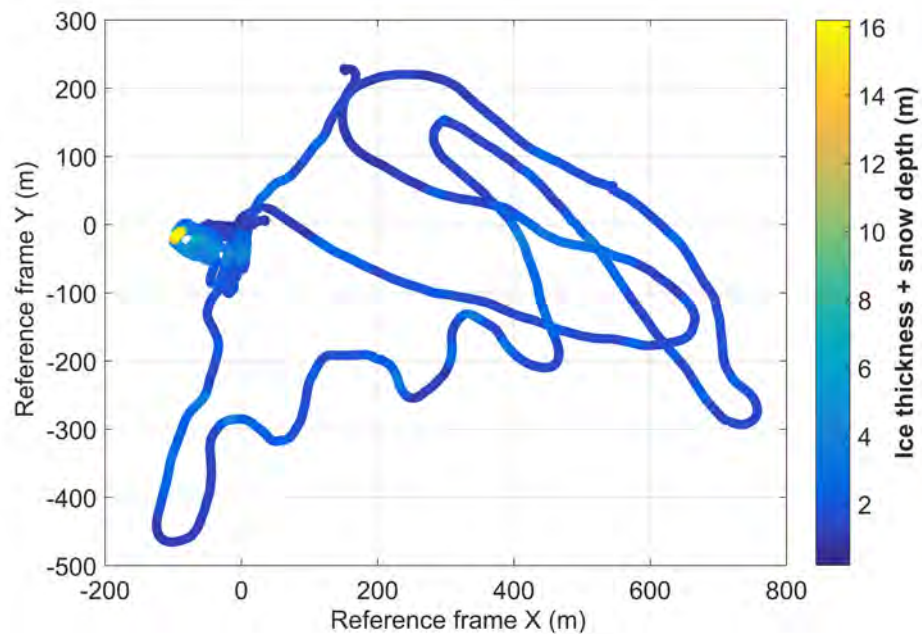


Figure 5.11: Station 29th September: sea ice thickness and snow depth distribution map measured by the GEM-2

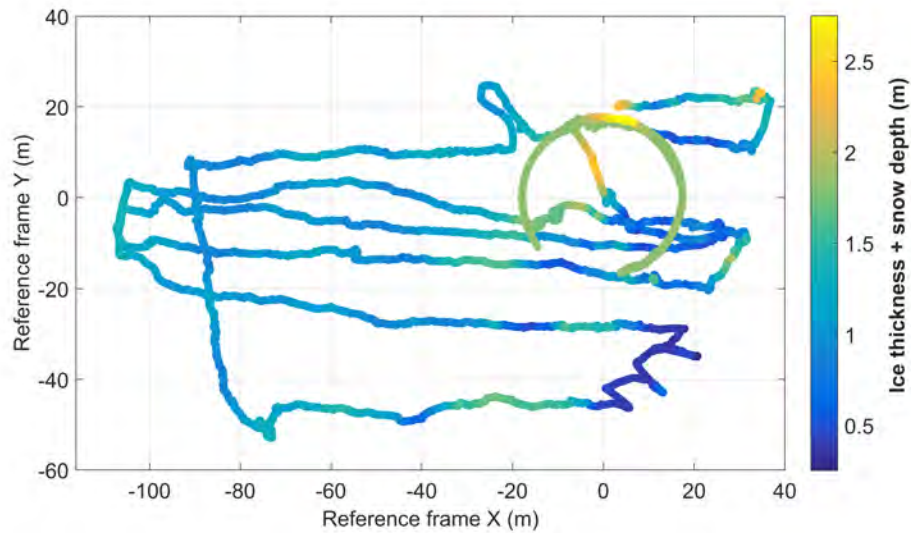


Figure 5.12: **Station 1st October: sea ice thickness and snow depth distribution map measured by the GEM-2**

- Figure 5.13, 5.14, and 5.15 represent data from the same three stations here displaying the distribution of **bare sea ice thickness**. The ice thickness values are calculated by subtracting the values of snow depth collected by the Magna Probe from the values of snow and ice plotted in the previous set of maps.

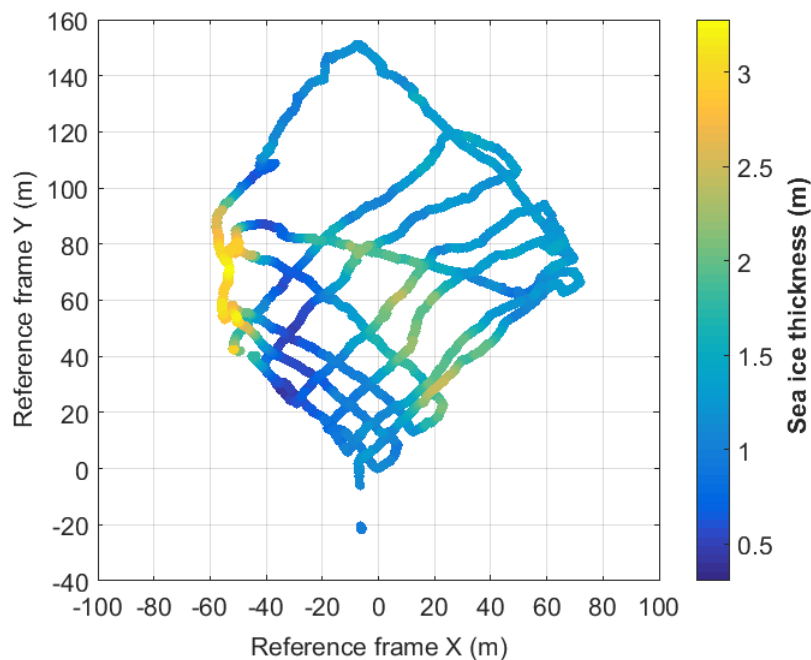


Figure 5.13: **Station 26th September: sea ice thickness distribution map without snow measured by the GEM-2**

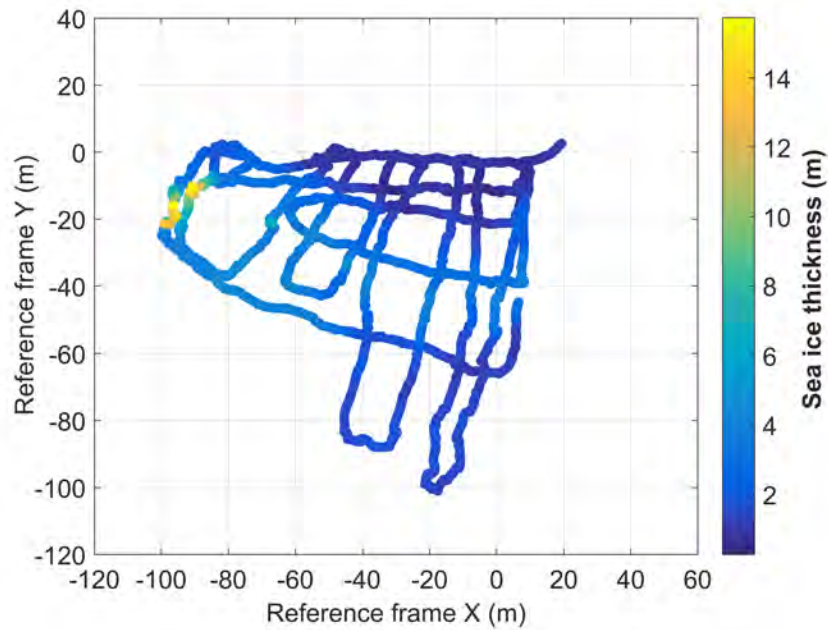


Figure 5.14: **Station 29th September: sea ice thickness distribution map without snow measured by the GEM-2**

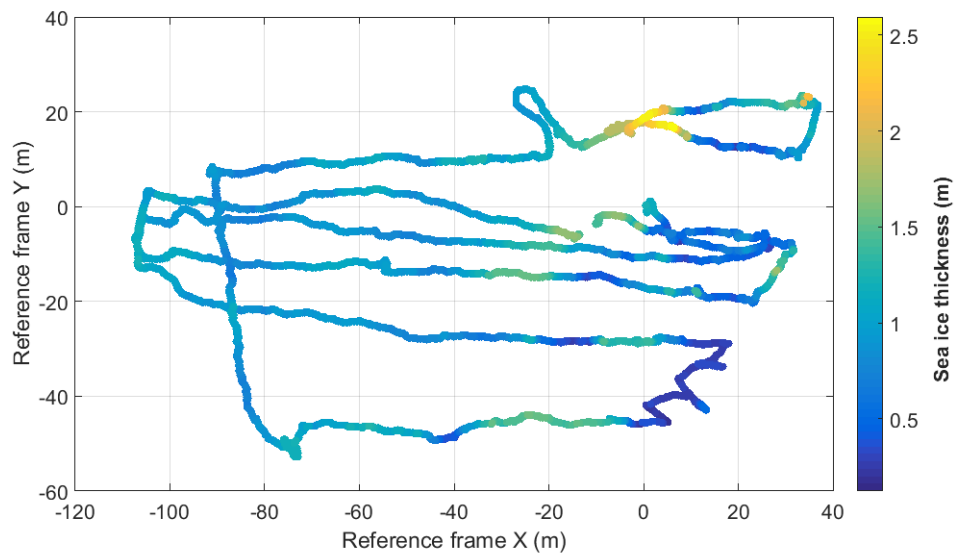


Figure 5.15: **Station 1st October: sea ice thickness distribution map without snow measured by the GEM-2**

A quick comparison between the MBS and these first GEM-2 maps shows very different survey extent and track shape for the same station. This difference is due to the fact that the electromagnetic device and the multibeam sonar are not operated along an identical path during the same station survey, and they

are not limited to the same grid areas. In general, the GEM-2 is operated over the same area that is scanned underwater by the ROV, but its survey can also be extended to different surrounding areas. This happens for example in the case of interesting features close to the ROV grid, such as the presence of the sail of a ridge, or in case that more statistics is advantageous for that particular station.

Different paths for the two instruments can cause the collection of very different sea ice distributions, due to the possible high spatial variability of sea ice thickness in that area.

Hence why, to deal with these differences I decided to create sea ice thickness and draft maps for the GEM-2 only for those areas that are more in common with the multibeam sonar survey tracks.

A clear example of this comes from the comparison of figure 5.10 and figure 5.13. When mapping sea ice thickness and draft the whole lower part of figure 5.10 has been rejected, as it represents the part of the GEM-2 survey that is not in common with that of the multibeam sonar.

This decision aims to reduce the differences between the distribution of thickness sampled by the two instruments, limiting the inequalities due to sea ice spatial variability along dissociated survey paths. By doing so, even though the two instrument tracks vary largely even on the common areas, the differences in sea ice thickness distributions are considerably minimised.

- The final GEM-2 maps in figure 5.16, 5.17, and 5.18 show the distribution of **sea ice draft** for the three stations. The draft values are derived from sea ice thickness measurements using the isostasy model conversion formula explained in section 3.5. These maps are those used for the comparison of sea ice draft distribution with the multibeam sonar maps.

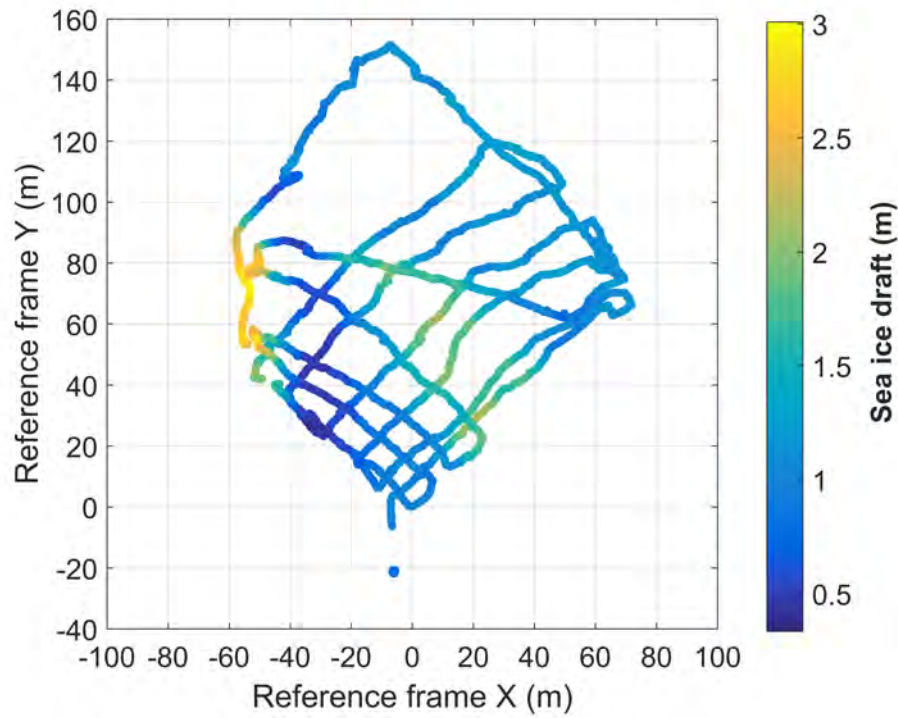


Figure 5.16: Station 26th September: Sea ice draft distribution map as calculated from the dataset of the electromagnetic device

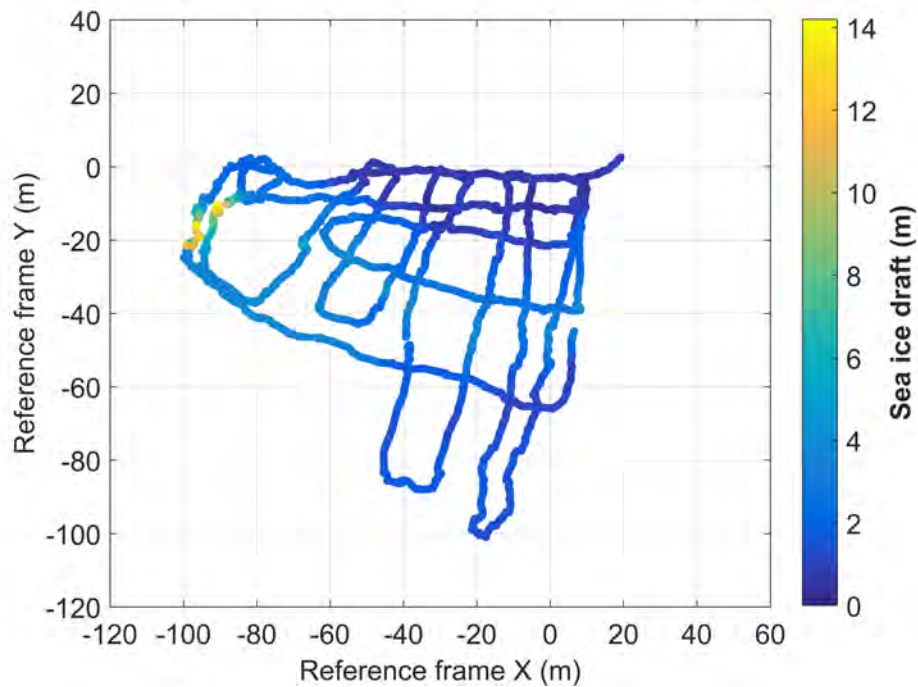


Figure 5.17: Station 29th September: Sea ice draft distribution map as calculated from the dataset of the electromagnetic device

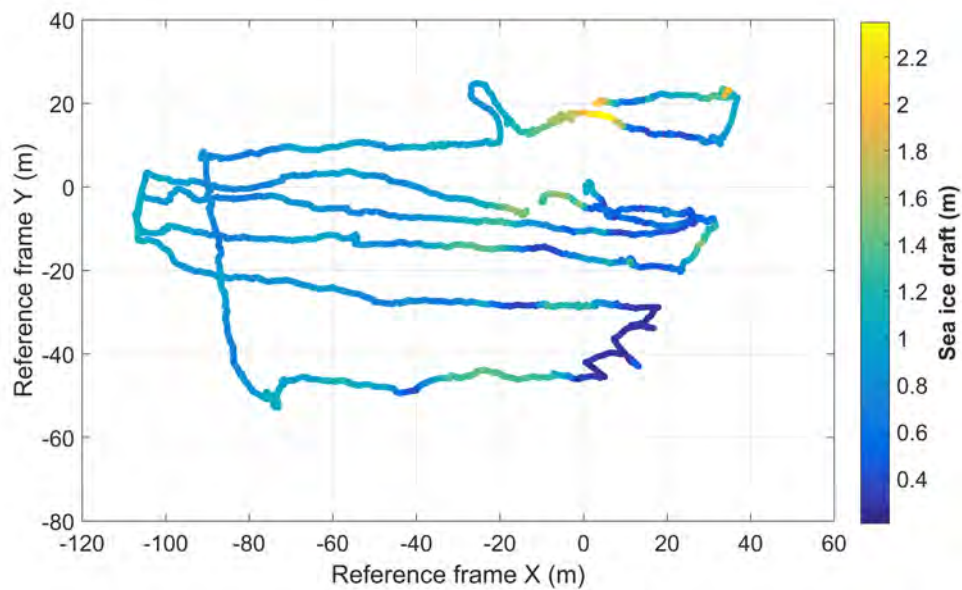


Figure 5.18: **Station 1st October: Sea ice draft distribution map as calculated from the dataset of the electromagnetic device**

5.4 Histograms of sea ice draft distribution

From the sea ice draft distribution maps of each station and for both instruments I have derived histograms to show the frequency of each sea ice draft value.

The histograms display draft values on the x axis expressed in meters and counts of each draft value on the y axis.

There are two different histograms for each station: one shows the dataset of sea ice draft collected by the multibeam sonar, and the other shows the corresponding dataset collected by the electromagnetic device. As already explained in the previous section the survey tracks of the GEM-2 differ from those of the MBS. Therefore, I have limited the GEM-2 sea ice mapping and the creation of the respective histograms to the areas where the MBS has also been operated.

All histograms are presented with the corresponding station map created with the respective instrument. This enables a clearer interpretation of the data and an easier orientation along the text when referring to the survey overview in figure 5.6.

5.4.1 Histograms of MBS sea ice draft datasets

A statistical study of multibeam sonar maps and the creation of corresponding histograms can be performed in CARIS Hips. Even though no additional software is needed, after a first data handling in CARIS Hips I decided to transfer the multibeam sonar statistics data into MatLab. This is done by extracting the data in ASCII format from CARIS Hips and importing them into MatLab.

This decision was made mainly for consistency and efficiency reasons. As the GEM-2 statistics must be created in MatLab, working on the same software for the MBS data enables the use of the same script for the creation of histograms for both instruments, thus saving time and facilitating the comparison.

The light blue histograms in figure 5.19, 5.20, and 5.21 show the sea ice draft distribution of the three stations measured by the multibeam sonar. The bin size is set equal to 0.1 m as it corresponds to the vertical uncertainty affecting sea ice draft measurements. The histograms are displayed in temporal order, from the 26th September to the 1st October. For easier interpretation, the corresponding MBS retrieved draft map is displayed in the upper-right corner of each histogram.

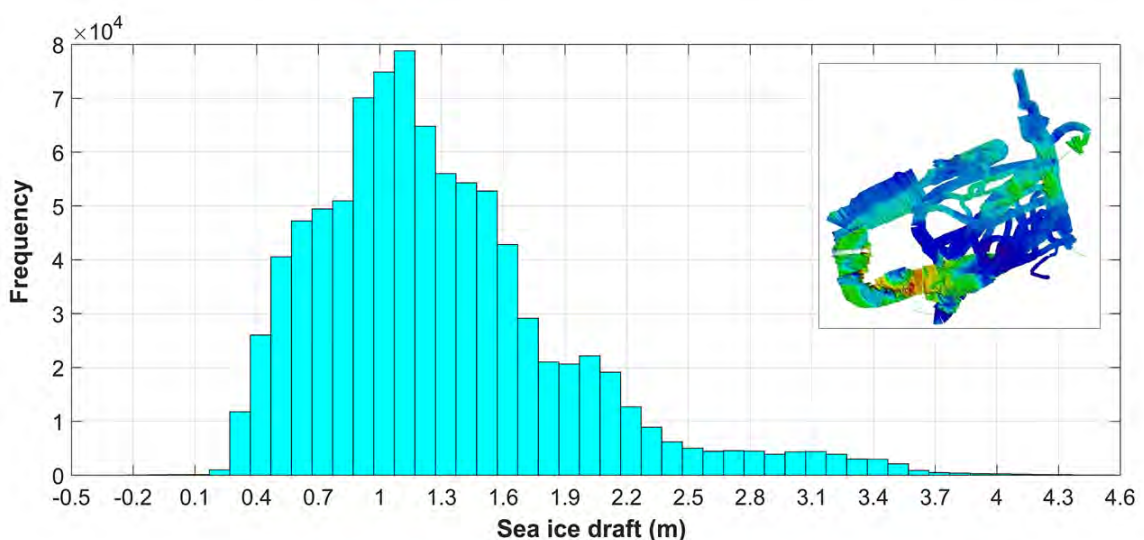


Figure 5.19: **Station 26th September: Histogram of the sea ice draft distribution as retrieved by MBS dataset. In the upper-right corner the corresponding MBS sea ice draft map is displayed.**

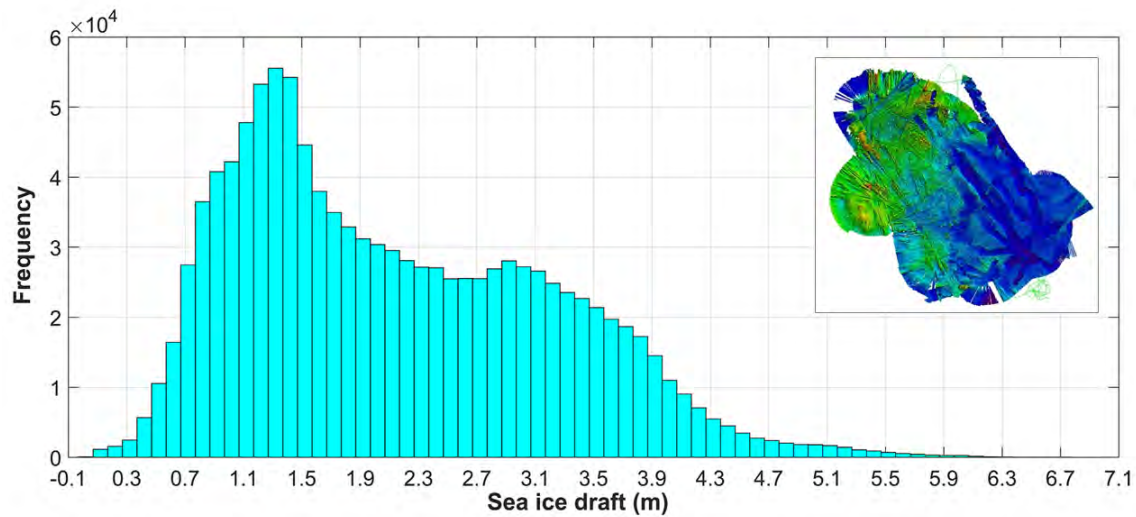


Figure 5.20: **Station 29th September: Histogram of the sea ice draft distribution as retrieved by MBS dataset. In the upper-right corner the corresponding MBS sea ice draft map is displayed.**

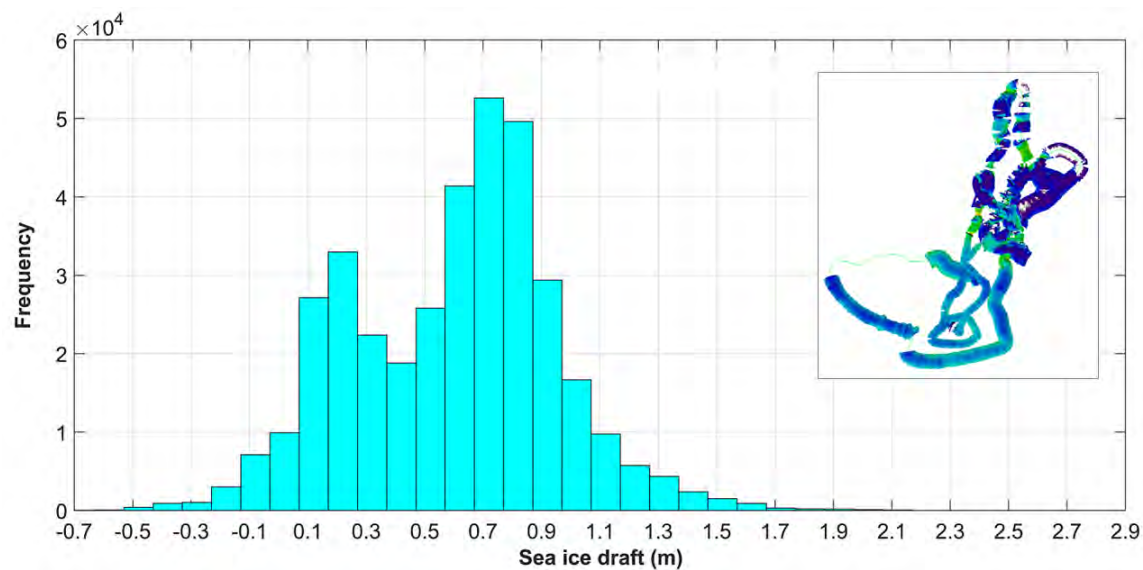


Figure 5.21: **Station 1st October: Histogram of the sea ice draft distribution as retrieved by MBS dataset. In the upper-right corner the corresponding MBS sea ice draft map is displayed.**

For each histogram I calculated minimum, maximum, mean, mode, and standard deviation values for the sea ice draft dataset.

The results for the MBS histograms are presented in table 5.4, where each quantity is expressed in meters.

Table 5.4: Statistical parameters of the three stations sea ice draft distribution measured by the multibeam sonar. All quantities are expressed in meters

Station	Minimum	Maximum	Mean	Mode	Standard deviation
26/09/2016	-0.4	4.5	1.3	1.1	0.6
29/09/2016	-0.1	6.8	2.1	1.3	1.1
01/10/2016	-0.7	2.7	0.6	0.8	0.4

5.4.2 Histograms of GEM-2 sea ice draft datasets

To create sea ice draft histograms the GEM-2 datasets must initially be converted from sea ice thickness into draft, using the isostasy model explained in section 3.5.

The GEM-2 dataset conversion is performed using MatLab and it enables a direct comparison with the sea ice draft distributions measured by the MBS. The creation of GEM-2 histograms is also performed in MatLab.

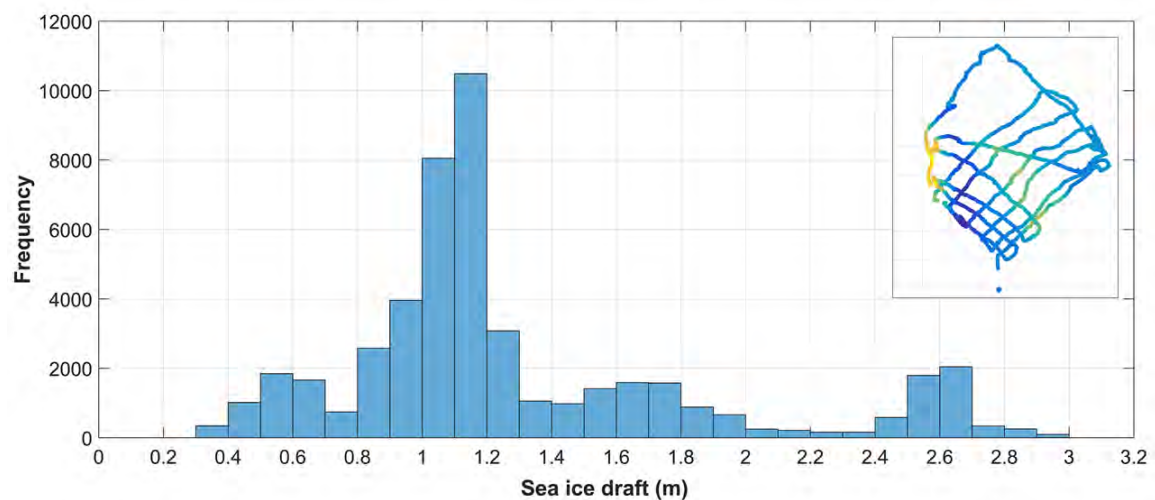


Figure 5.22: **Station 26th September: Histogram of the sea ice draft distribution as retrieved by the GEM-2 dataset. In the upper-right corner the corresponding GEM-2 sea ice draft map is displayed.**

The blue histograms in figure 5.22, 5.23, and 5.24 show the sea ice draft distribution for the datasets of the three stations as measured by the electromagnetic device after snow subtraction and draft conversion.

The histograms are displayed in temporal order. For easier in-

terpretation, the corresponding GEM-2 draft map is displayed in the upper-right corner of each histogram. The bin size for these histograms is 0.1 m, equal to the electromagnetic device vertical resolution.

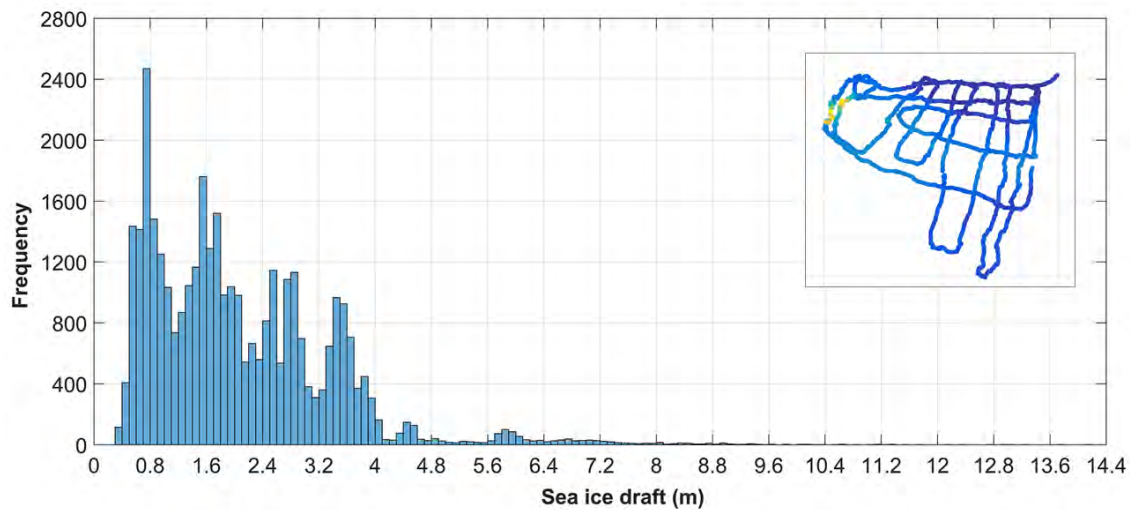


Figure 5.23: **Station 29th September: Histogram of the sea ice draft distribution as retrieved by the GEM-2 dataset. In the upper-right corner the corresponding GEM-2 sea ice draft map is displayed.**

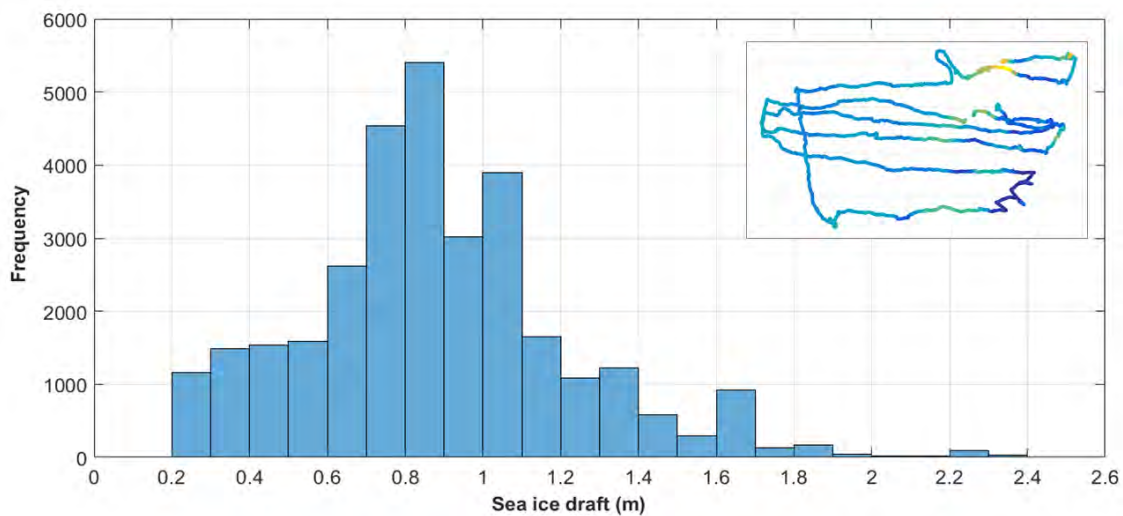


Figure 5.24: **Station 1st October: Histogram of the sea ice draft distribution as retrieved by the GEM-2 dataset. In the upper-right corner the corresponding GEM-2 sea ice draft map is displayed.**

For these histograms I calculated minimum, maximum, mean, mode, and standard deviation values for the sea ice draft dataset measured

by the GEM-2. The results are presented in table 5.5.

Table 5.5: Statistical parameters for the three stations sea ice draft distribution measured by the electromagnetic device. All quantities are expressed in meters

Station	Minimum	Maximum	Mean	Mode	Standard deviation
26/09/2016	0.3	3.1	1.3	1.1	0.6
29/09/2016	0.3	14.2	2.0	0.7	1.3
01/10/2016	0.2	2.4	0.8	0.9	0.4

5.5 Comparison of the two methods for sea ice draft measurements

The maps and histograms displayed in the previous paragraphs show the sea ice draft distributions collected by the two devices used during the campaign, the MBS and the GEM-2. In this section a comparison between the two resulting sets of distribution is presented.

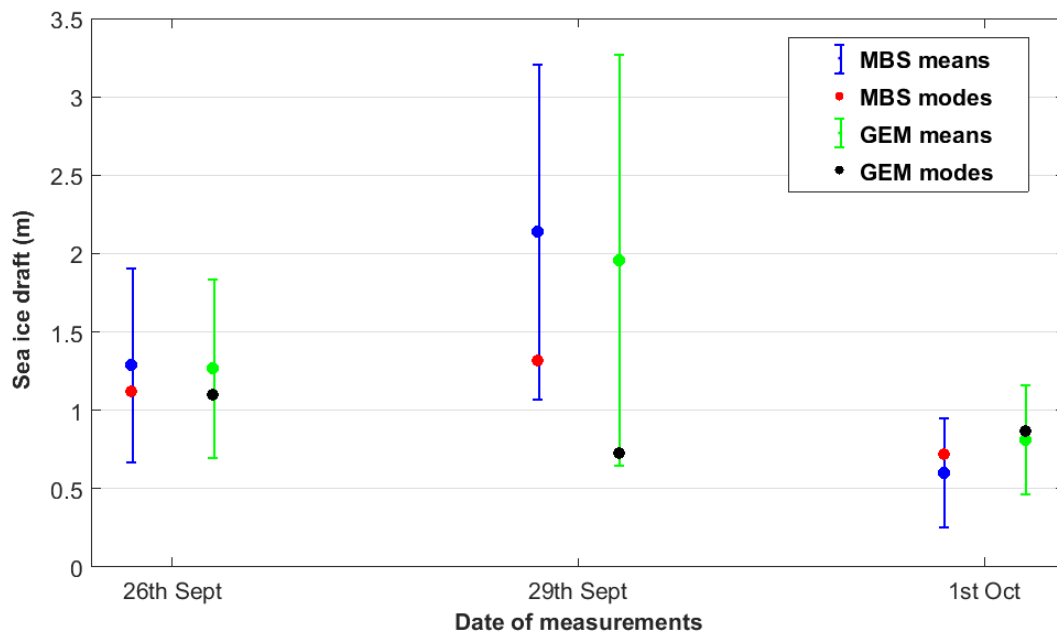


Figure 5.25: Comparison of sea ice draft for the three stations between the MBS and the GEM-2 datasets. The x axis shows the survey dates and the y axis shows the sea ice draft mean, mode, and standard deviation values of the stations expressed in meters. Blue represents MBS mean values and their corresponding standard deviations, while green represents the same type of data collected by the GEM-2. Red and black points show respectively the mode values measured by the MBS and by the GEM-2 for each station

Figure 5.25 shows the sea ice draft mean, mode, and standard deviation values for the three stations for both MBS and GEM-2 datasets (previously presented in table 5.4 and 5.5) allowing for a direct comparison of the sea ice draft measurements between the instruments.

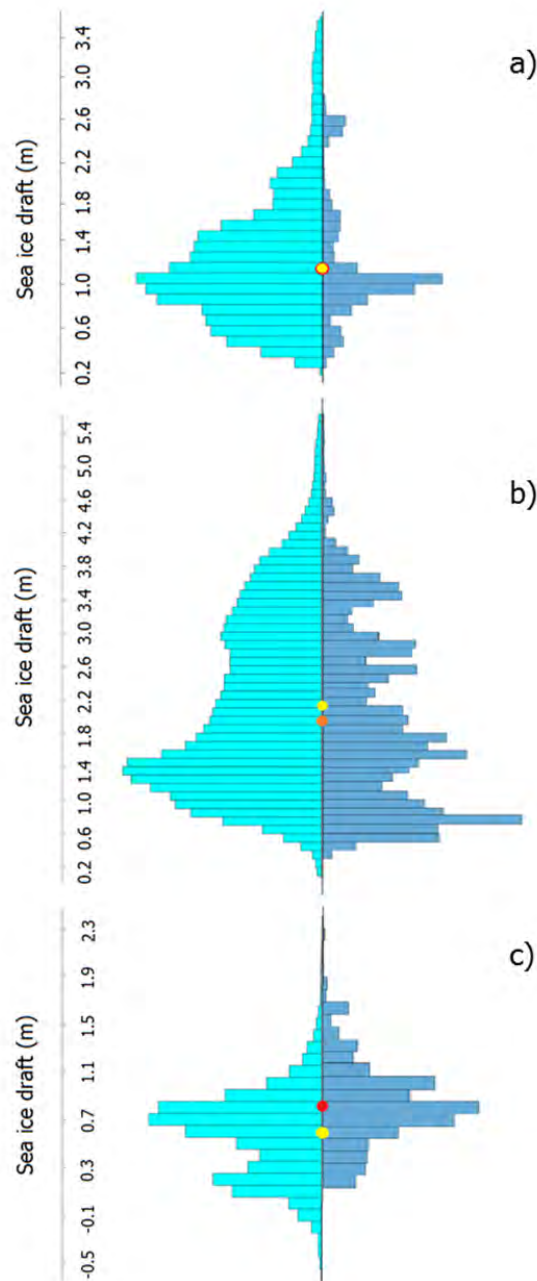


Figure 5.26: Violin plots of sea ice draft distributions collected by the MBS (to the left) with mean values in yellow, and by the GEM-2 (to the right of the plot) with mean values in orange. The three station distributions are displayed in temporal order from top to bottom, with a): station 26th September; b): station 29th September; c): station 1st October

An efficient more graphic way to compare the two instrument distributions for all the stations is to use violin plots.

Figure 5.26 presents a violin plot for each station, created using the histograms presented in section 5.4. Each violin plot is composed of two histograms: the light blue ones to the left represent the sea ice draft distribution collected by the MBS (for more details see figure 5.19, 5.20, and 5.21); while the dark blue ones to the right represent the histograms created using the GEM-2 datasets (for more details see figure 5.22, 5.23, and 5.24).

The long tails of the histograms at thick ice values are not displayed for a clearer comparison with those stations where this component is missing.

5.6 Snow depth distribution analysis

For a complete overview of the vertical composition of the sea ice I created a map of the snow depth distribution and a corresponding histogram for each station.

The maps in figure 5.27, 5.28, and 5.29 show the snow depth distribution measured by the Magna Probe for the three stations, displayed in temporal order.

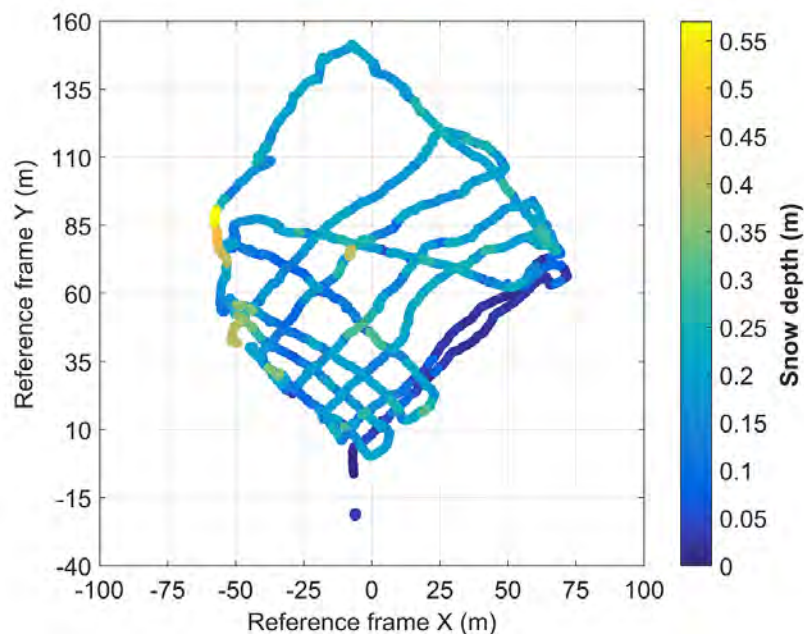


Figure 5.27: **Station 26th September: Snow depth distribution map as retrieved by the Magna Probe sampling.**

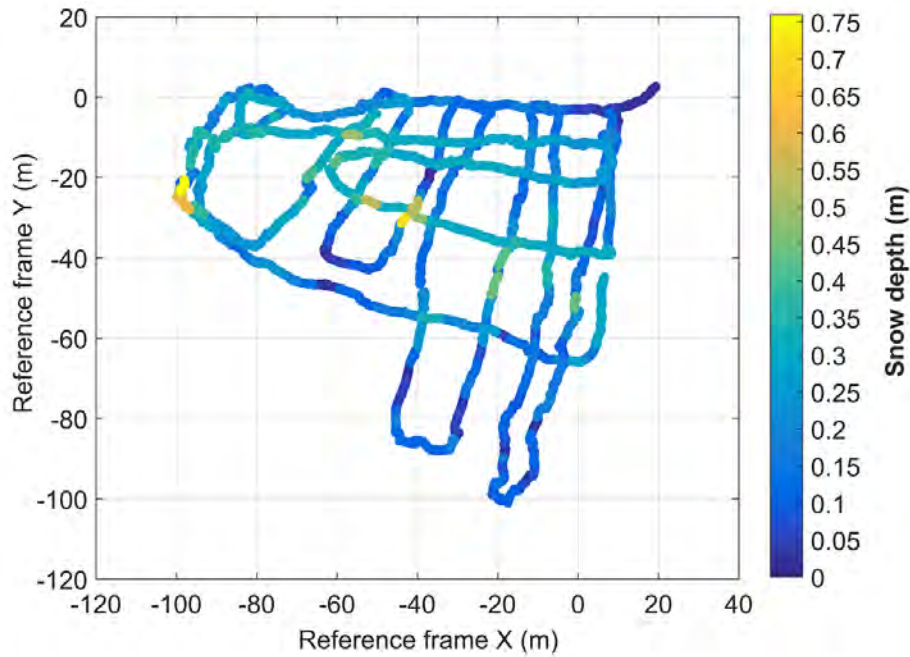


Figure 5.28: **Station 29th September: Snow depth distribution map as retrieved by the Magna Probe sampling.**

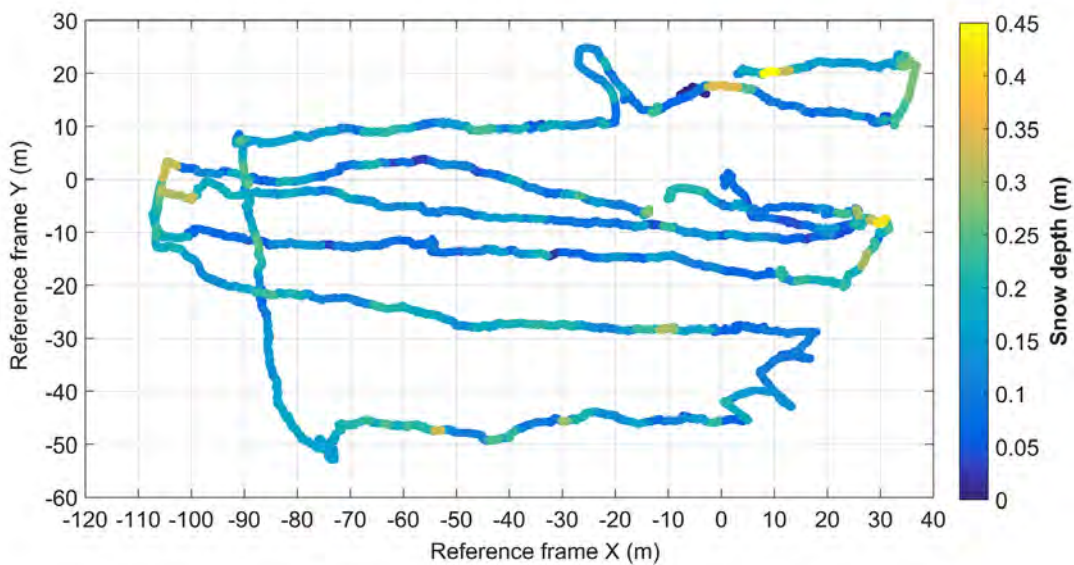


Figure 5.29: **Station 1st October: Snow depth distribution map as retrieved by the Magna Probe sampling.**

A comparison with the draft maps retrieved by the electromagnetic device (figure 5.16, 5.17, and 5.18) shows the same track shapes. This is because for these snow maps I only considered the part of the Magna Probe survey that overlaps with the survey area of the MBS, similarly to what has already been done for the GEM-2 draft maps,

as explained in section 5.3.2.

The histograms of snow depth frequency for each station are displayed in figure 5.30, 5.31, and 5.32.

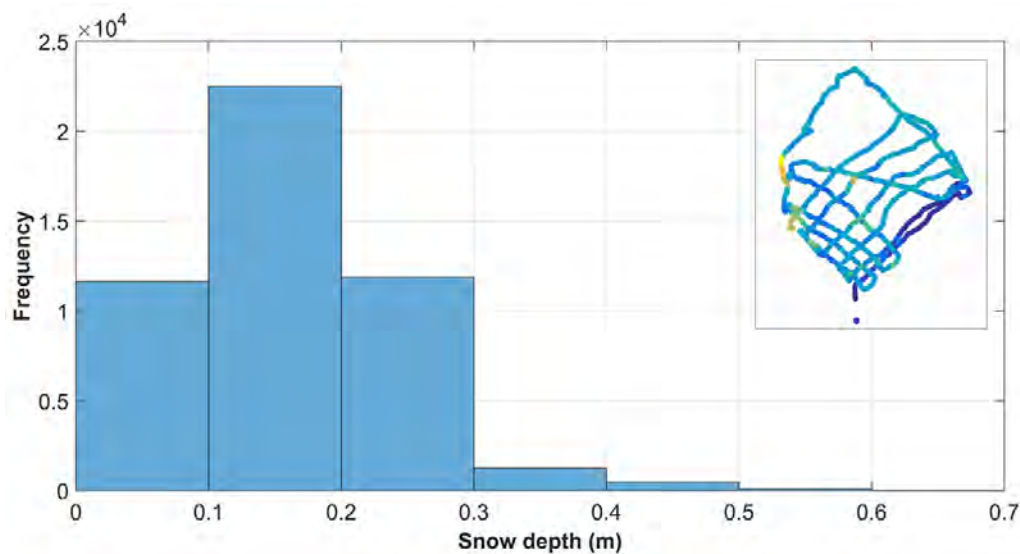


Figure 5.30: **Station 26th September: Histogram of snow depth distribution retrieved by the Magna Probe. In the upper-right corner the snow depth map of the corresponding station is displayed.**

The histogram bin size of 0.1 m equals the vertical resolution of the GEM-2 and not of the Magna Probe, as it would be expected. This is because the snow depth datasets used in this project have been collected by the Magna Probe but have been retrieved for this study in an indirect way.

As explained in section 4.4, the available data come from GEM-2 files previously handled in MatLab that give both the values of the bare sea ice thickness, and the sum of the thickness of the sea ice and the snow depth together. The snow depth values are then found by subtracting the two mentioned datasets, hence why the bin size for the histograms is equal to the vertical resolution of the electromagnetic device. This does not affect the resulting sea ice draft vertical resolution, as the GEM-2 vertical uncertainty still predominates on the Magna Probe one.

Each histogram displays in the upper-right corner the snow depth map of the corresponding station, for a clearer interpretation of the

different datasets.

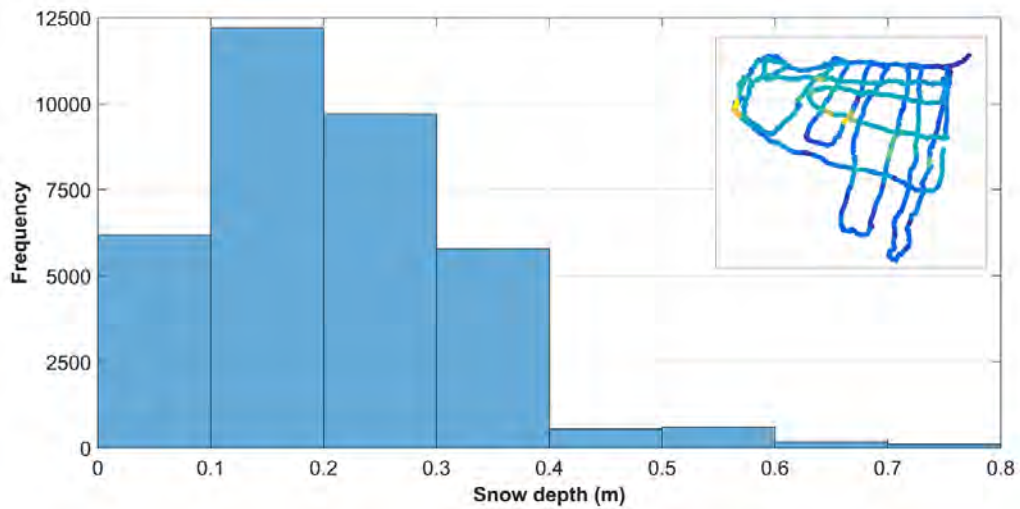


Figure 5.31: **Station 29th September:** Histogram of snow depth distribution retrieved by the Magna Probe. In the upper-right corner the snow depth map of the corresponding station is displayed.

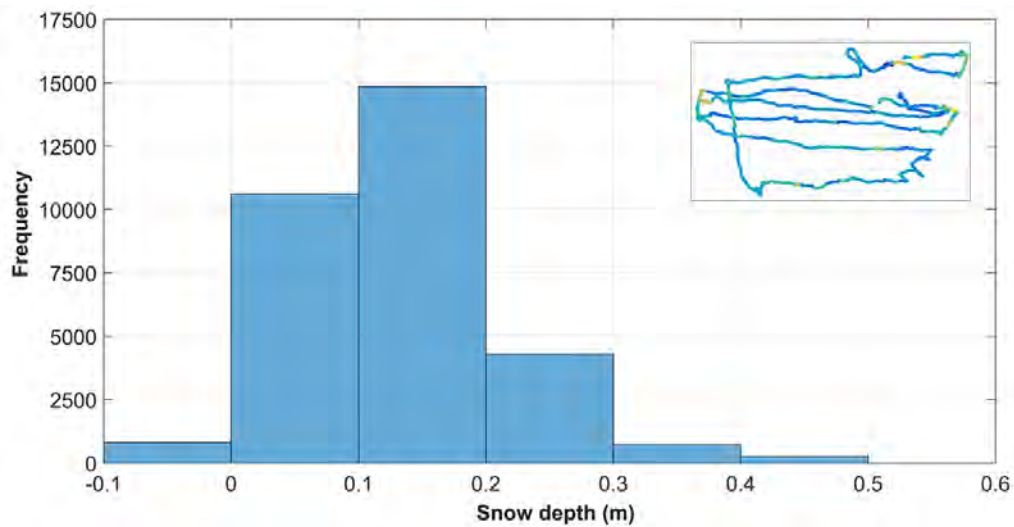


Figure 5.32: **Station 1st October:** Histogram of snow depth distribution retrieved by the Magna Probe. In the upper-right corner the snow depth map of the corresponding station is displayed.

Table 5.6 shows the statistical parameters for the snow depth distribution for the three stations.

Table 5.6: Minimum, maximum, mean, mode, and standard deviation values for the snow depth distribution for the three stations. All quantities are expressed in meters

Station	Minimum	Maximum	Mean	Mode	Standard deviation
26/09/2016	0.0	0.6	0.2	0.2	0.1
29/09/2016	0.0	0.8	0.2	0.2	0.1
01/10/2016	0.0	0.4	0.1	0.1	0.1

For a quick comparison between the snow cover of the three surveys, I plotted the snow depth mean and mode values of the three stations as presented in figure 5.33.

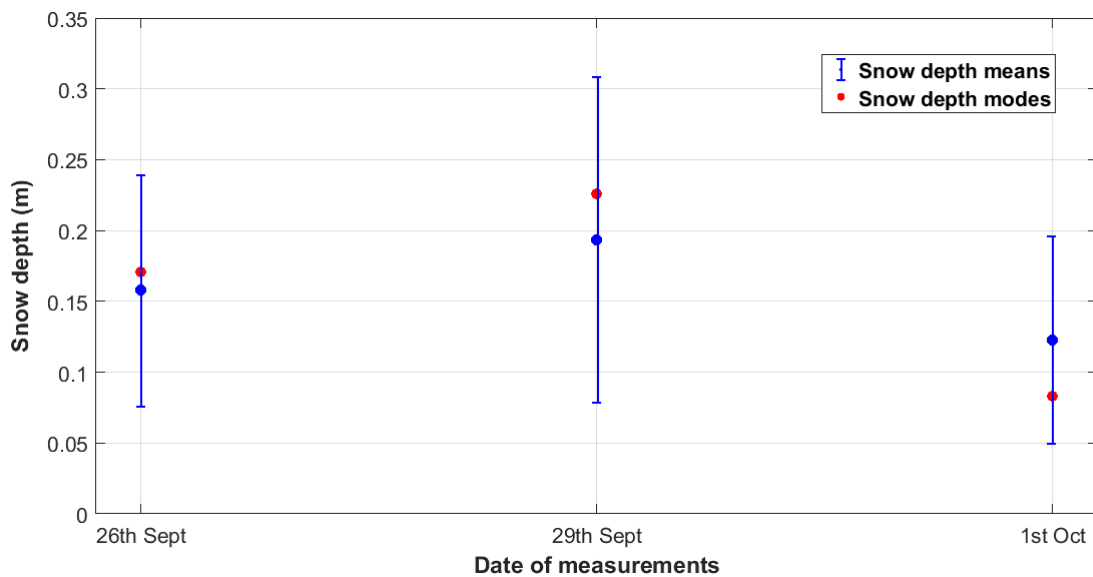


Figure 5.33: Snow depth mean, mode, and standard deviation values of the three stations. Blue represents the mean values and the respective standard deviations, while red represents the mode values. The error bars represent the standard deviation of the snow depth distribution for the corresponding station

5.7 Sea ice growth model results

The datasets of sea ice thickness collected by the GEM-2 and by the MBS are here investigated in order to assess sea ice growth in the three study areas. To do this the FDD model for sea ice thermodynamic growth explained in section 3.6.2 is used.

Sea ice growth is generally assessed by collecting time series of sea ice thickness measurements over the same area and investigating

the potential growth using a model. In this study however, there is no repeated sea ice thickness dataset available for the same station, hence the measurements from the three stations are used as a time series. This is because this work was meant as a pilot project intended with different purposes, therefore the main aim is not the use of the FDD model. The following sea ice growth investigation is meant merely as a trial for the use of the model and an attempt to investigate the possibility to determine sea ice growth for this study asset.

To assess sea ice growth among the three stations I first converted sea ice draft into thickness, and then compared the modal values of each station by plotting them in temporal order and fitting the resulting trend according to the FDD model growth law.

The datasets of the three stations show a bi- or multimodal sea ice thickness distribution, as the histograms in section 5.4 show. The presence of more than one mode derives from the high spatial variability of the sea ice thickness distributions, created by the presence of different features in the study areas, such as ridges and melt ponds. Hence, it is necessary to select which mode to use in the model.

Moreover, a comparison of the three stations shows different sea ice thickness distributions. In particular the set of ridges found in stations 26th and 29th September cause the sea ice thickness distribution to be more varied than in station 1st October, where the sea ice is thinner and more homogeneous. A threshold must therefore be set to try to compare similar sea ice thickness values between the stations and avoid areas of deformed ice where the FDD model should otherwise be modified (see [53]).

These two main issues make it more difficult to investigate a potential thermodynamic growth than if the survey were repeated on the same area.

In order to diminish the impact of the spatial variability intra and inter-stations, I decided to only study thin first-year level ice. Following the sea ice nomenclature of the World Meteorological Organisation ([103]), this type of ice is characterised by a maximum

thickness of 0.7 m. This value is here set as a threshold to separate each thickness distribution in two parts: a first part of thin ice that is investigated for thermodynamic growth, and a second part of thick ice.

However, not all stations show a clear mode in the range of thin first-year ice values. I therefore decided to use for the model the thinnest sea ice thickness mode present in each histogram that is as close as possible to the defined threshold, and does not exceed the upper limit for medium first-year ice of 1.2 m ([103]). In the following I refer to these resulting mode values as the “thin ice” thickness modes.

In this study sea ice thickness measurements are available from both MBS and GEM-2 datasets. Ideally, the FDD model was meant to be used on both sets of measurements. However, the fact that the MBS and the GEM-2 were operated on different areas of the same station causes the thickness distributions measured by the two instruments to show some differences, as it is visible by comparing the respective histograms in section 5.4. In particular, while a thin ice thickness mode is present in each of the GEM-2 datasets, the MBS does not always record such a mode for thin sea ice.

Due to the lack of a clear thin ice component measured by the MBS, modeling sea ice growth using the FDD model for the multi-beam sonar dataset is inhibited. Consequently, I was able to use the model only for the sea ice thickness datasets retrieved by the GEM-2. The GEM-2 collected values of thin first-year ice draft and thickness mode for each station are shown in table 5.7.

Table 5.7: **Thin ice draft and thickness mode values with respective uncertainties for each station. All quantities are expressed in meters**

Station	Thin ice draft mode	Thin ice thickness mode	Uncertainty
26/09/2016	0.5	0.6	0.1
29/09/2016	0.7	0.8	0.1
01/10/2016	0.8	0.9	0.1

As explained in section 3.6.2, to use the FDD model the ratio

α between snow depth and ice thickness must be known.

In this study there are three different α coefficients, one for each station, hence they are averaged for use in the model. The single ratio values are extracted from field data by calculating the mean ratio for each station.

The results are shown in table 5.8 where the averaged mean ratio is also displayed with the corresponding uncertainty.

Table 5.8: **Snow-ice ratio with corresponding uncertainty for each station and calculated averaged mean ratio**

Station	Snow-ice ratio	Uncertainty
26/09/2016	0.19	0.16
29/09/2016	0.14	0.10
01/10/2016	0.13	0.11
Averaged mean ratio	0.15	0.10

Referring to formula 3.17, for the initial value of ice thickness $H(1)$ I used the thin ice thickness mode of station 26th September, as this is the first station in temporal order.

Regarding the calculation of the time integral of the difference between the temperature of water and air, I extracted the field data from DSHIP, a specific software that collects and archives various kind of data during Polarstern navigation ([28]).

From the PS101 DSHIP database I extracted the daily mean air and water temperature averaged over 24 hours measured by the weather station on board for the part of the expedition relevant for this sea ice growth study, from 26th September to the 1st October for a total of 6 days.

Table 5.9 shows the parameters downloaded from DSHIP and used for the calculation of the time integral of formula 3.17. Each day in table 5.9 was characterised by subfreezing air temperature, and accounted for in the model.

Table 5.9: Values of air and water temperature extracted from DSHIP. From left to right: daily mean air temperature and respective standard deviation; daily mean water temperature and respective standard deviation; difference of the daily mean water temperature and mean air temperature with respective uncertainty. In the bottom-right corner: accumulated freezing-degree days “FDD” with respective uncertainty, and average $(\bar{T}_w - \bar{T}_a)_m$ of the mean temperature differences between the six days. The FDD is calculated from the data in the above column as the sum of the daily mean air temperatures after subtracting the freezing daily water temperatures

Date	\bar{T}_a ($^{\circ}C$)	$\sigma(T_a)$ ($^{\circ}C$)	\bar{T}_w ($^{\circ}C$)	$\sigma(T_w)$ ($^{\circ}C$)	$\bar{T}_w - \bar{T}_a$ ($^{\circ}C$)	$\delta(\bar{T}_w - \bar{T}_a)$ ($^{\circ}C$)
26/09/16	-2.3	0.4	-1.8	0.1	0.5	0.1
27/09/16	-5.5	1.3	-1.8	0.1	3.7	0.3
28/09/16	-8.1	1.6	-1.7	0.1	6.4	0.4
29/09/16	-9.9	0.9	-1.7	0.1	8.2	0.2
30/09/16	-9.8	1.1	-1.7	0.1	8.1	0.2
01/10/16	-6.6	3.8	-1.6	0.1	5.0	0.8
					31.9 ± 1.1 $^{\circ}C \cdot days = \text{FDD}$	
					5.3 ± 1.1 $^{\circ}C = (\bar{T}_w - \bar{T}_a)_m$	

When all these field data are gathered together the thin sea ice thickness mode values for the three stations are plotted, and the resulting growth trend can be fitted using the numerical constants found in literature ([2], [53]) and presented in table 5.10.

Table 5.10: Critical numerical constants used for the FDD model growth fit

Parameter	Numerical value
Sea ice thermal conductivity	$k_i = 2.2$ W/K·m
Snow thermal conductivity	$k_s = 0.3$ W/K·m
Sea ice density	$\rho_i = 916.7$ kg/m ³
Water latent heat of freezing	$L_i = 334.9 \times 10^3$ J/kg

The mathematical formula used to fit the trend in time of the sea ice thickness mode values for the three stations according to the FDD model is the following customized power law:

$$y = (a + bx)^{1/2} \quad (5.2)$$

Comparing this power law to the FDD model formula 3.17, “y” represents the thickness mode for the final station 1st October, and “x” represents days at freezing temperature. The fitted parameters “a” and “b” are defined as follows and the respective units are displayed:

$$a = H^2(1) \quad (5.3)$$

$$[a] = m^2$$

$$b = \frac{2k_i}{\rho_i L_i} \frac{1}{\left(1 + \frac{k_i \alpha}{k_s}\right)} (\bar{T}_w - \bar{T}_a)_m d_s \quad (5.4)$$

$$[b] = m^2/days$$

The numerical values for these two parameters are calculated using:

- the constants found in literature and presented in table 5.10;
- the calculated snow-ice proportionality coefficient α of table 5.8;
- the average of the mean temperature differences $(\bar{T}_w - \bar{T}_a)_m$ presented in table 5.9;
- and the conversion parameter d_s from seconds to days, necessary to make the model formula homogeneous in units.

The resulting fit is presented in figure 5.34. It shows the best fit for the trend of the thin sea ice thickness modes of the three stations in time according to the FDD model growth formula.

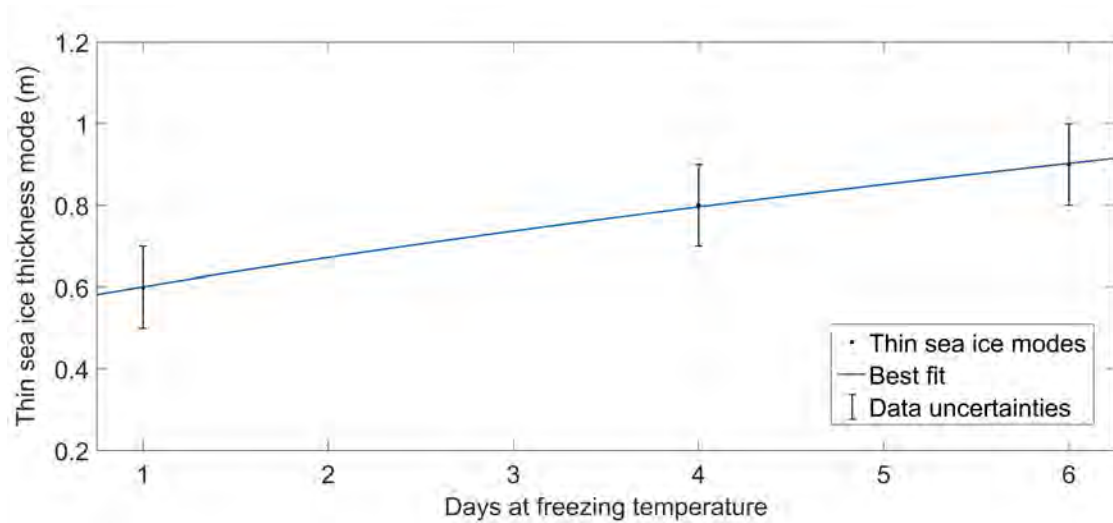


Figure 5.34: Best fit of thin sea ice thickness trend in time. On the horizontal axis are displayed the days at freezing temperature, while the vertical axis shows the thin sea ice thickness mode values for the three stations. Each mode value is affected by an uncertainty of 0.1 m

Table 5.11 shows the values of the parameters a and b in two cases: a_{FDD} and b_{FDD} are the two parameters calculated for the FDD model formula using field data, under the hypothesis of the presence of a component of thermodynamic growth among the stations; while a_{fit} and b_{fit} are the two parameters as they are extracted from the fit.

Table 5.11: Values a_{FDD} and b_{FDD} calculated from field data, and values a_{fit} and b_{fit} extracted from the thin sea ice growth fit. Each parameter is presented with the corresponding uncertainty

$a_{FDD} \pm \delta a_{FDD} (m^2)$	$a_{fit} \pm \delta a_{fit} (m^2)$
0.4 ± 0.1	0.3 ± 0.1
$b_{FDD} \pm \delta b_{FDD} (m^2/days)$	$b_{fit} \pm \delta b_{fit} (m^2/days)$
0.003 ± 0.001	0.091 ± 0.026

The value for the final sea ice thickness mode predicted after a period of ice growth of 6 days is calculated using the FDD model formula.

Table 5.12 enables the comparison between the actual GEM-2 field data measurement $H(D)$ for station 1st October and the value obtained from the model, indicated with $H(D)_{FDD}$.

For comparison sake, the final sea ice thickness mode value $H(D)_{And}$

predicted using the empirical approximate equation implemented by Anderson is presented in the same table (see formula 3.19).

Table 5.12: **Sea ice thickness final mode values obtained from GEM-2 field measurements, calculated using the FDD model formula, and predicted by Anderson's law with respective uncertainties. Each quantity is displayed with the corresponding uncertainty and is expressed in meters**

$H(D) \pm \delta H(D)$	0.9 ± 0.1
$H(D)_{FDD} \pm \delta H(D)_{FDD}$	0.63 ± 0.09
$H(D)_{And} \pm \delta H(D)_{And}$	0.72 ± 0.05

Chapter 6

Discussion

6.1 Considerations regarding the multibeam sonar resolution

Section 5.1.3 showed how calculating the resolution of the multibeam sonar is important to improve the quality of the sea ice maps, and make a survey as efficient as possible in terms of time and resources. Due to the close distance between the MBS and the bottom of the sea ice at which the ROV can operate, and due to the high density of pulses that the MBS can transmit, high resolution topographic maps of the sea ice underside can be created.

This section presents the parameters that can be adjusted to achieve a high spatial resolution for the sea ice maps created using the MBS datasets. The role of the pulse repetition rate in reaching such resolution was also revealed. Moreover, the use of the CTD mounted on the ROV instead of the pressure sensor is suggested in order to retrieve depth measurements for more accurate draft calculations. With this method it is possible to create sea ice draft maps affected by smaller vertical uncertainties.

A future study of how the DT101 data processing time depends on the choice of the settings is suggested. Trials of data acquisition and processing using 120 beams instead of 480 during the beamforming process are strongly recommended before the start of a new campaign, in order to increase the multibeam sonar performances.

Depending on the survey goals and strategies and on the surveyed object sizes, a survey area could be first mapped with low resolution and in a short time. This would give a first idea of the areas where

to focus the survey, for example around some specific features such as a ridge. Then the ROV and MBS survey parameters previously discussed could be changed to create a high resolution map of the interesting parts of the survey area.

Resolution symmetry on both track directions can also be achieved by adjusting the survey settings.

The spatial resolution achieved so far with this study asset is higher or comparable to recent similar studies on sea ice underside topography (see for example [55]).

It has to be kept in mind though that the actual positioning system for the ROV is the main source of uncertainty. Indeed, the uncertainty value related to the positioning system is around two orders of magnitude higher than the one of the multibeam sonar. Unless the precision in finding the position of the vehicle is soon increased, the nominal resolution of the multibeam sonar cannot be reached in terms of the location of the details displayed.

Without a better positioning system, the precision of the maps created using the MBS data loses part of its importance. The result is a high resolution map with details that can be visualised up to 0.1 m resolution, but with a positioning uncertainty that does not allow the knowledge of where these features are located in space, with an uncertainty as large as 1 m.

For this reason, a separate study of the positioning system is necessary and strongly recommended.

6.2 Analysis of the sea ice underside topographic maps

The 3D topographic maps created using CARIS Hips show the morphology of the sea ice underside with great detail. The images shown in section 5.2 reveal the presence of deformed ice in station 26th September.

The bottom left corner of figure 5.7 shows an area of highly deformed ice compared to the surroundings. After a comprehensive study of this ice feature using CARIS and video footage in parallel, and after comparisons with similar topographic features found in literature (see for example [100]), this thick ice formation is most probably found

to be a new pressure ridge ([103]). The bottom-left image from the upward-looking camera in figure 5.5 validates this hypothesis: clear blocks of ice of different sizes are piled up forming the ridge keel. The corresponding area of the 3D map reports a maximum draft for this ridge of around 4 m.

Level-ice is also present in the map and represented by cold colours. The major part of the level-ice of the map in figure 5.5 has a mean draft below 1 m and it is most probably thin first-year ice, while the blue-green areas of the map represent medium and thick first-year ice, with a maximum draft of around 1.8 m ([103]).

From green and towards warmer colours the draft exceeds 2 m and the corresponding sea ice is recognised and classified as multi-year ice.

In this study the resolution of the topographic maps varies continuously mainly due to the change of the diving depth of the ROV during a survey. A suggestion for potential future surveys dedicated to the study of the sea ice underside topography could be to operate the ROV at a constant distance from the ice bottom and with a constant speed. This would lead to more homogeneous topographic maps with swaths of the same size and a constant spatial resolution, as much as the navigation issues discussed in section 4.1.2 allow for it.

The high resolution of the MBS and the possibility to change it according to the parameter relations presented in section 5.1.3 reveal promising performances for this instrument. The upward-looking MBS method for sea ice underside surveys described in this thesis will enable future investigations of both sea ice topography and sea ice texture. Future dedicated surveys will have the potential to study the sea ice roughness and to identify particular features such as the ice brine channels, as demonstrated by previous recent studies where a MBS lateral resolution of 0.05 m is used with these purposes ([55]). For a complete overview, the 3D topographic maps of the sea ice underside could be combined in the future with 3D maps of the sea ice surface morphology from airborne images.

6.3 Comparison between MBS and GEM-2 sea ice draft distributions

The MBS and GEM-2 sea ice draft distributions presented in section 5.3 and 5.4 are here compared.

First of all, the shape of the maps created using the two instruments for the same station do not coincide, hence the tracks followed by the MBS and the GEM-2 respectively do not overlap. As a consequence, even if the survey area is the same, the two instruments might measure different sea ice thickness. Operating the two instruments along different tracks does not create big differences in the collected datasets if the sea ice thickness variability over the survey area is low, otherwise it can lead to the collection of very different thickness distributions.

Section 5.5 presented a comparison between the sea ice draft distributions resulting from the two methods for sea ice thickness sampling. As can be seen in figure 5.25, the mean and mode values of the sea ice distributions measured by the two instruments for each station show good agreement within the instrumental uncertainties. The standard deviation values represent the variability of the sea ice thickness for the respective stations. The larger standard deviation of station 29th September represents the strong component of sea ice rafting observed during this survey. This is also visible in the respective histograms in figure 5.20 and 5.23. Indeed, the sea ice draft values for station 29th of September reach a maximum of 7.1 m for the MBS dataset and 14.4 m for the GEM-2 dataset, while the maximum draft values found during the other two surveys is respectively 3 and 4 m.

The main differences between the sea ice draft distributions collected by the two instruments appear when comparing the histograms presented in section 5.4. The bin size of the histograms is the same for the two instruments, as it is set equal to the vertical resolution of the GEM-2 and the MBS/pressure sensor setup that are both 0.1 m. Large differences are visible in the thin ice range and in the tail of the histograms towards thicker regions of ice. The GEM-2 histograms

do not show any value of sea ice draft below around 0.2 m. This is because the electromagnetic device should not be pulled on sea ice that is thinner than a threshold thickness of 0.3 m for safety reasons. As a consequence, the maps of sea ice draft retrieved by the GEM-2 miss completely the component of young ice. The MBS on the contrary, can be operated under any ice thickness value, thus giving important information about thin sea ice that would otherwise be lost if operating the GEM-2 only. The lack of the thin ice component cause the GEM-2 calculated sea ice means to be biased towards higher values, hence the resulting draft distributions do not reproduce the sea ice draft distribution in an accurate way.

The issue of the lack of the thin sea ice component does not affect the draft distributions measured using the MBS. Instead, table 5.4 shows negative minimum draft values. The reason for such inconsistent values could be linked to an initial incorrect calibration of the MBS/pressure sensor setup. One option is that the pressure sensor was not properly calibrated at the surface level and the depth measurements used to calculate the sea ice result therefore biased. The second option is that the MBS is incorrectly calibrated. A third option is that negative draft values could derive from the fact that a constant sound velocity correction has been used instead of a complete profile at various depths.

For future surveys it is suggested to first check the pressure sensor calibration at the beginning of each survey, and then use the tool “Vertical shift” during the data handling in CARIS Hips. The use of this tool can reveal whether the measured sea ice draft is biased. This is done by checking that the ice draft that is measured below an area of open water is zero, and otherwise shifting the whole dataset of the resulting measured value.

It is also suggested to use sound velocity profiles during data handling in CARIS Hips.

Differences in thick ice regions can be recognised when comparing the tail of the distributions. In station 26th September and 1st October the sea ice draft maximum value is larger in the MBS dataset than in the GEM-2 one, while the reverse is true in station

29th September. There are two main limitations that apply to the statement of general conclusions on the comparison of the tails of these histograms: one is that the different paths of the two instruments can give different ice thickness measurements due to the high spatial variability of the sea ice thickness; the second is that it is obvious that three stations are not enough to state any general comment. The same applies to the mean and mode respective values collected by the two instruments. In the first two stations the mean and mode collected by the MBS are higher than for the GEM-2, while in station 1st October the GEM-2 values are the highest.

Additionally, as explained in section 3.3, previous works on electromagnetic induction sounding for sea ice thickness measurements found that this sampling method underestimates the thickness of sea ice ridges. This would lead to datasets of sea ice draft with biased thick ice values.

The underestimation of ridges is one of the limitations linked to the electromagnetic device method. It is found to generally lead to smaller standard deviation values, hence in this work the datasets of the MBS could be expected to include thicker ice than the GEM-2 ones with a resulting more various distribution of sea ice draft. However, this is true only for station 26th September and 1st October, while station 29th September shows a very high spatial variability and the corresponding standard deviation measured by the GEM-2 is larger than for the MBS dataset. As stations 26th and 29th September show the highest spatial variability of all stations with the presence of thicker areas, the fact that the GEM-2 mean and mode values in these station are smaller than those measured by the MBS could be linked to the underestimation of the GEM-2 in measuring the thickness of the ridged areas. Station 1st October is mainly composed of level-ice, hence the underestimation of the GEM-2 is not visible. The GEM-2 collected mean and mode values are found to be larger than the corresponding ones collected by the MBS. Two stations are however not enough to prove such a hypothesis.

Due to the underestimation of the GEM-2 in measuring the draft of sea ice ridges, it is expected to find longer tails for the histograms created from the MBS datasets. This is found for station 26th

September and 1st October, however Station 29th September shows an opposite behaviour. It displays a set of measurements for thick ice that reaches a maximum of 14.2 m, when the MBS dataset maximum value is 6.8 m. This is probably due to the presence in this station of thick deformed ice that was surveyed by the GEM-2, but was not, or only partially, by the MBS. This example shows the limitations of sampling sea ice thickness along different paths, as the ice spatial variability hinders a direct comparison between the two sampling methods.

Although the thin ice and thick ice ranges are not covered in the same way by the two instruments, the mean and mode values for all three histograms show a good agreement within the instruments uncertainties thus validating the newly implemented workflow for measuring sea ice draft with a multibeam sonar.

The histograms created from the MBS datasets show a much smoother shape when compared to those retrieved by the GEM-2. This is due to the higher amount of data collected by the MBS during each survey, that is on average one order of magnitude more than the amount collected by the GEM-2.

A high amount of data give a more accurate representation of the actual sea ice draft distribution, so that a generally bimodal trend can be recognised for the multibeam sonar datasets of the three surveys, while the GEM-2 histograms show sea ice draft distributions with multiple peaks.

This is shown in particular when the GEM-2 histogram in figure 5.23 is compared to the MBS histogram in figure 5.20. The multi-peak distribution of the sea ice draft collected by the GEM-2 for station 29th September is probably caused by the sparse amount of data collected by the electromagnetic device compared to the MBS. In this station only a maximum of 2500 measurements for each sea ice draft value are collected by the GEM-2, while 56000 counts are collected by the MBS for the same station.

Even after accounting for the differences between the survey tracks of the two instruments, it is expected that a higher number of collected data during the GEM-2 surveys would lead to a smoother distribution reproducing a bi-modal distribution similar to the one created from

the MBS datasets.

The density of the collected measurements is not the only parameter to be compared between the two instruments, as the footprint size must also be considered.

As previously stated, both the MBS and the GEM-2 footprint size depend on the distance between the instrument and the sea ice underside. By setting the same distance for both devices equal to 5 m, the resultant footprint size of the MBS is $(0.26) \times (0.26)$ m, while the GEM-2 footprint is around $(20) \times (20)$ m, hence in this case the footprint of the MBS is almost two orders of magnitude smaller than the GEM-2 one. In general the GEM-2 footprint is wider than the MBS one. This enables the MBS to collect more accurate measurements, especially in regions of thick ice such as in the presence of a ridge. The large footprint of the GEM-2 is also the cause of the already mentioned ridge underestimation, explained in section 3.3.

In turn, the MBS system for sea ice draft measurements is not free of issues. The ROV is a complicated vehicle to be operated, while the GEM-2 surveys take place simply by pulling a sledge.

While the GEM-2 needs the Magna Probe to sample the snow depth, the MBS needs the pressure sensor depth measurements in order to retrieve sea ice draft. Concerning this, in this study these two instruments are mounted in different positions on the ROV. This is because they cannot be positioned on top of each other for obvious reasons, and therefore they monitor slightly different parts of the sea ice underside. The sea ice draft calculated using the resulting measurements is therefore affected by this misalignment. As this study represented a first attempt to measure sea ice draft using the MBS, this misalignment was not taken into account. However, a study of this issue is suggested for future operation, especially in case of planned high resolution surveys.

In conclusion, the statistical values of the datasets measured by the MBS and the GEM-2 are in good agreement between the two methods and validate the new processing workflow implemented during this thesis work. The thin and thick ice components show

some differences due to the high spatial variability of the sea ice draft over the stations, and to the different survey tracks followed by the two instruments.

Comparing the two methods show that the issues of using the GEM-2 over areas of ice thinner than 0.3 m and over ridges do not occur when measuring sea ice draft using the MBS. Hence, the MBS represents a valuable source of thin ice measurements, important for modeling ice growth. Although in this pilot project the collected MBS datasets could not be used for sea ice growth investigations, this study showed that there is no instrumental obstacle in targeting future surveys with this purpose. Moreover, even if the MBS represents a technically demanding method of measuring the sea ice thickness, it is a non-destructive sampling method suitable for repeated surveys on the same area.

For a future study of the comparison between the two instruments, it is suggested to follow the same tracks during a survey or to cover thoroughly the same survey area using the mow the lawn technique. This study showed the validation of the MBS implemented workflow through the good agreement with the GEM-2 datasets. Future surveys could also compare the GEM-2 and MBS datasets to ice cores taken during the same survey for further thickness comparison.

6.4 Sea ice growth model validation

The results obtained from the study of the sea ice thickness growth in section 5.7 are here discussed. The field data measurements used for this growth study are compared the sea ice growth model predictions of section 3.6.2. In section 5.7 the FDD model was used to investigate a potential component of sea ice thermodynamical growth between the three stations. The FDD model growth law was parameterised using formula 5.2 and the coefficients a and b were calculated using the collected field data according to the model.

After a period of 6 days with the values for temperature, snow, and initial ice thickness presented in section 5.7, the final ice thickness resulting from the use of the model is 0.63 m (see table 5.12). Hence, the resulting sea ice thermodynamical growth rate would be equal to 5 mm/day. This result is in good agreement with the values of sea ice

growth rate found in the Arctic for similar environmental conditions and during the late growing season (see for example [53], [82], [8]).

The same formula was used to fit the trend in time of the thin ice thickness mode values collected for the three stations during the surveys. The resulting fit coefficient a and b presented in table 5.11 do not agree with the parameters calculated using the FDD model. Being the final sea ice thickness measured 0.9 m, the resulting hypothetical sea ice thermodynamical growth would be of 50 mm/day. A comparison between the final values of modelled and field data sea ice thickness presented in table 5.12 shows a difference of 30 cm, and a difference of one order of magnitude between the sea ice growth rates.

In section 5.7 the result of the use of the model for sea ice growth implemented by Anderson is also used to calculate the hypothetical final sea ice thickness value for the period studied in this work. The final value of 0.7 m reported in table 5.12 would lead to a sea ice thermodynamical growth of 20 mm/day. This result is in good agreement with the values found in literature for the early stage of sea ice growth, up to 10 days, and with similar temperatures ([53], [82], [8]).

However, this result is overestimated, as the α factor used in this empirical model is smaller than the one measured during the study period. Being the ratio of snow cover depth and sea ice thickness larger in this study, it is expected to find a sea ice growth rate smaller than the one calculated using Anderson's model. Moreover, this model only applies to sea ice thickness below 0.8 m, while in this study thicker modes are also considered in the calculations, and could lead to differences in the modelled final thickness value.

The field data can be modelled using the FDD model growth formula, but the results do not represent the collected data. The fitted parameters a and b do not agree with those calculated using the FDD growth formula, therefore the model is not convalidated for the collected sea ice thickness modes, with the measured environmental values of initial ice thickness, snow cover, and freezing-degree days. In conclusion, the fit results show a possible thermodynamical growth

that however does not match the conditions of study. This is probably linked to the fact that a study of the thermodynamical growth is inhibited by the high spatial variability between the three stations. While the first two stations show thicker ice distributions, station 1st October presents thinner sea ice. This might lead to different thin ice mode values influenced by the local ice topography. Moreover, the mean thinner ice together with the smallest amount of snow cover among the stations, might have caused a faster growth for station 1st October.

It is therefore found that in order to be able to determine a thermodynamical growth component, the spatial variability should be minimised. The choice of using sea ice thickness modes with values that are above the range of the thin ice might have compromised the study. This choice was however forced by the datasets available, and it demonstrated that it is not possible to detect a thermodynamical growth component with this study asset. Therefore, future studies for sea ice growth study should focus on time series of sea ice thickness measurements on the same area.

Although the MBS datasets could not be used in this study as time series for sea ice growth investigations, the measurements collected during station 1st October reveal important information. The FDD model prediction seem to be validated by the first mode of thin ice in station 1st October. During the expedition this station area was surveyed twice in a period of 4 weeks. During the first time open water areas were reported, as it was the end of the Arctic summer. After 4 weeks, the same area shows no more open water, and the first sea ice thickness mode measured in this station is 0.2 m. A resulting growth of 20 cm in 4 weeks would give a growth rate of around 7 mm/day, in good agreement with the values found in literature.

6.5 Operational recommendations: Advancements in approach and methods

During this work different enhancements to the multibeam sonar data acquisition and handling are suggested.

In addition to what has already been recommended for the MBS resolution, more suggestions concern the data acquisition software and script.

Concerning the renavigation files created by SPOT.ON, it is suggested to create a dedicated MatLab script for data cleaning. This would allow for a quick rejection of all data out of their physical range, and avoid the large pitch and roll outliers that still affect the MBS datasets. For the sake of efficiency, it is also suggested to include in this script the offset between the MBS and the pressure sensor positions.

Some issues linked to the non-synchronised time between the MBS data acquisition and handling software, and the presence of negative time to ping in the datasets found during this work were promptly solved by AWI scientists.

Some operation limitation still remain and need some improvement. The largest uncertainty in this work is linked to the USBL positioning system. The respective uncertainty is as large as 1 m, hence it inhibits the determination of the precise location of the features mapped by the multibeam sonar.

However, this issue does not affect the final results of this work. The statistics used to handle the huge amount of data for the entire stations averages out the uncertainty spreading it on a big set of data and does not change the final conclusions.

Moreover, the MBS datasets are affected by ray bending, hence sound velocity profiles should be added for future surveys to achieve accurate results, especially during deep dives.

A new calibration of the MBS at the beginning of each survey is also suggested. Calibrating the instrument below the open water area of the dive entrance hole could allow for a more accurate determination of sea ice draft. As each MBS retrieved sea ice draft map shows a component of negative draft values, measuring the open water offset and using it in CARIS Hips during the Vertical shift process could improve the results.

Chapter 7

Conclusions and outlook

In this thesis I successfully implemented a new workflow for sea ice draft measurements using the data collected by the upward-looking multibeam sonar mounted on the AWI remotely operated vehicle during the Polarstern campaign PS101. The data were collected using, besides many other sensors, a multibeam sonar and a pressure sensor working in parallel. The resulting datasets were processed using the software CARIS Hips. The new workflow enables the creation of sea ice underside 3D topographic maps correlated with the respective sea ice draft measurements. After the data handling in CARIS Hips, the map statistical information can be easily exported into a more common software, such as MatLab. Hence, this workflow can also be used for a quick visualisation and data handling of the multibeam sonar data during field campaigns. The spatial resolution of the MBS was also calculated in order to determine the resolution of the sea ice draft maps created in CARIS Hips. These maps show a resolution as high as 0.03 m along-track and 0.04 m across-track at 3.5 m depth, and a vertical uncertainty of 0.1 m affects the sea ice draft measurements. The calculated footprint size of the MBS at 3.5 m is found to be (0.18) x (0.18) m. Also, the MBS derived sea ice draft datasets are compared to the sea ice thickness data collected by the GEM-2 that was operated during the same surveys. The comparison can take place after the conversion of the GEM-2 datasets from ice thickness to draft using the isostasy equilibrium. This procedure allowed for a direct comparison of the sea ice draft distributions measured by the two instruments for the same survey area. The two sampling methods were found to have the same vertical resolution. In future surveys the MBS vertical resolution could be improved by using the CTD mounted on the ROV to

collect depth measurements. The two instrument distributions agree well on the modal values within the instruments uncertainties. Some differences are found in the thin and thicker part of the sea ice draft distributions. The GEM-2 lacks any sea ice thickness measurement below 0.3 m because of safety operational reasons, and it shows shorter tails towards thick ice values, probably due to the instrument typical underestimation of deformed ice. Moreover, the high amount of data collected by the MBS due to its sampling rate, that is double the one of the GEM-2, create smooth bi-modal sea ice draft distributions. Instead, the GEM-2 sea ice draft histograms show a multi-peak distribution. The footprint of the MBS was calculated for different survey depths. At the average depth of 5 m, the MBS footprint is found to be two orders of magnitude higher than that of the GEM-2, therefore it gives more accurate results, and makes the MBS an appropriate instrument for detailed surveys. From this study comparison the MBS results to be a valuable source of thin ice measurements that are important for sea ice growth modelling; it gives accurate measurements on deformed ice as it does not underestimate ridged areas as it happens for the GEM-2; and it can be operated under any ice thickness, without any lower threshold limitations. Although the GEM-2 is an easy device to be handled, while driving the ROV is a demanding process, the MBS has the merit of being a versatile, comprehensive, and multidisciplinary sensor platform. The MBS is also a non-destructive sea ice draft sampling method suitable for repeated surveys.

In conclusion, the good agreement of the two methods on the modal and mean values proved the validity of the newly implemented workflow. A future combined operation of the two instruments on the same survey area, respectively under and above the sea ice, would allow for a comprehensive study of the sea ice thickness, sea ice surface morphology, and sea ice underside topography.

Suggestions were formulated in order to improve the MBS data acquisition and respective script after some issues were found during the data handling of the MBS. Among other improvements, a better positioning system and the use of a sound velocity profile for sonar range calculations are recommended for future surveys.

Also, estimates of the ROV diving parameters have been calculated in order to indicate the best resolutions achievable for different future

survey settings and purposes.

Finally, the freezing-degree days model for sea ice growth was applied to investigate potential changes of the thin ice thickness over time between the three stations due to thermodynamical growth. The snow depth measurements collected over the survey stations by the Magna Probe were taken into account when using the model. The FDD model formula for sea ice growth was used to fit the GEM-2 collected thin ice mode values. It is found that the model does not agree with the field data. Most probably the determination of a sea ice thermodynamical growth component is hindered by the high spatial variability of the three survey areas. Nonetheless, the formation in one of the stations of a few centimeters of new ice from open water during a survey period of a month is found to be in good agreement with the growth rate values found in literature.

The results of this thesis prove that the new processing workflow implemented in CARIS Hips allows for a reliable, efficient, and high resolution retrieval of sea ice draft measurements collected by an upward-looking sonar mounted on a remotely operated vehicle.

The methods presented in this thesis can be adopted for a future year-round spatial and temporal study of sea ice thickness and underside morphology, such as the upcoming drift campaign MOSAiC (Multi-disciplinary drifting Observatory for the Study of Arctic Climate). This type of survey would enable a constant study of the same ice floe, providing time series of various sea ice properties. A potential long term study of the thermodynamic growth and the application of precise growth models to the results would become possible. A year-round survey would also enable the study of seasonal transitions that are necessary to fill the existing data gap during winter time in the Arctic. During such a challenging survey, the multibeam sonar together with the other many interdisciplinary sensors of the ROV could be mounted on an autonomous underwater vehicle. This would empower long, fast, and deep surveys, with no tether-limited ranges, and operated by a very stable vehicle. These suggestions would help to achieve a complete overview of the sea ice underside environment, and contribute to the improvement of climate models.

Bibliography

- [1] Alexander, P., Duncan, A., Bose, N. and Smith, D. (2013) Modelling acoustic transmission loss due to sea ice cover. *Acoustics Australia* 41(1):79-89
- [2] Alexandrov, V., Sandven, S., Wahlin, J. and Johannessen, O. M. (2010) The relation between sea ice thickness and freeboard in the Arctic. *The Cryosphere*, 4:373-380
- [3] “All About Sea Ice”, National Snow and Ice Data Center. Accessed 16 February 2018 /cryosphere/seaice/index.html
- [4] Allen, J. T., Keen, P. W., Gardiner, J., Quartley, M. and Quartley, C. (2017) A new salinity equation for sound speed instruments. *Limnology and Oceanography: Methods*, Volume 15, Issue 9
- [5] Anderson, L. (1961) Growth rate of sea ice. *Journal of Glaciology*, 3(30):1170-1172
- [6] Appel, I. (2016) Enhancing calculation of thin sea ice growth. *Polar Science* 10(4)
- [7] Arndt, S., Meiners, K. M., Ricker, R., Krumpfen, T., Katlein, C. and Nicolaus, M. (2017) Influence of snow depth and surface flooding on light transmission through Antarctic pack ice. *J. Geophys. Res. Oceans*, 122:2108-2119
- [8] Ashton, G. D. (1989) Thin Ice Growth. *Water Resources Research* 25(3):564-566
- [9] Barber, D. G., Asplin, M. G., Papakyriakou, T. N., et al. (2012) Consequences of change and variability in sea ice on marine ecosystem and biogeochemical processes during the 2007-2008 Canadian International Polar Year program. *Climatic Change* 115:135

- [10] Barnhart, K. R., Overeem, I. and Anderson, R. S. (2014) The effect of changing sea ice on the physical vulnerability of Arctic coasts. *The Cryosphere*, 8:1777-1799
- [11] Behrendt, A., Dierking, W. and Witte, H. (2015) Thermodynamic sea ice growth in the central Weddell Sea, observed in upward-looking sonar data. *Journal of Geophysical Research: Oceans*, 120:2270-2286
- [12] Berkson, J. M., Clay, C. S. and Kan, T. K. (1973) Mapping the underside of arctic sea ice by backscattered sound. *The Journal of the Acoustical Society of America* 53, 777
- [13] Brandon, M. A., Cottier, F. R. and Nilsen, F. (2010) *Sea Ice*, chapter *Sea Ice and Oceanography*:79-111. Blackwell Publishing Ltd, 2nd edition
- [14] Brekhovskikh, L. M. and Godin, O. (1990) *Acoustics of Layered Media I*, Springer-Verlag Berlin Heidelberg (1)
- [15] Buckingham, M. J. (1988) Diffraction of harmonic acoustic radiation by the apex of a ridge. *The Journal of the Acoustical Society of America* 83:S1, S47-S47
- [16] Centre for Polar Observation and Modelling Data Portal, ESA. <http://www.cpom.ucl.ac.uk/csopr/seaice.html>
- [17] Chamuel, J. R. and Brooke, G. H. (1988) New findings on scattering from floating plate with lateral heterogeneities. *The Journal of the Acoustical Society of America* 83:S1, S47-S47
- [18] Chen, C. T. and Millero, F. J. (1977) Speed of sound in seawater at high pressures. *J. Acoust. Soc. Am.* 62(5):1129-1135
- [19] Christ, R. D. and Wernli, R. L. (2013) *The ROV Manual: A User Guide for Remotely Operated Vehicles*. Second Edition, Butterworth-Heinemann
- [20] Chu, D. and Stanton, T. K. (1990) Application of Twersky's boss scattering theory to laboratory measurements of sound scattered by a rough surface. *The Journal of the Acoustical Society of America* 87(4):1557-1568

- [21] Coachman, L. K. and Barnes, C. A. (1962) Surface Water in the Eurasian Basin of the Arctic Ocean. *Arctic*, 15(4):251-278
- [22] Colosi, J. A. (2016) *Sound Propagation through the Stochastic Ocean*. Cambridge University Press
- [23] Comiso, J. C., Parkinson, C. L., Gersten, R. and Stock, L. (2008) Accelerated decline in the Arctic sea ice cover. *Geophys. Res. Lett.*, 35(1), L01703
- [24] Del Grosso, V. A. (1974) New equation for the speed of sound in natural waters (with comparisons to other equations). *The Journal of the Acoustical Society of America* 56,1084
- [25] Descamps, S., Aars, J., Fuglei, E., Kovacs, K. M., Lydersen, C., Pavlova, O., Pedersen, A. O., Ravolainen, V. and Stroem, H. (2017) Climate change impacts on wildlife in a High Arctic archipelago-Svalbard, Norway. *Glob Change Biol*, 23:490-502
- [26] Dieckmann, G. S. and Hellmer, H. H. (2010) *Sea Ice, The importance of sea-ice: An overview*, pages 1-22. Blackwell Publishing Ltd, 2nd edition
- [27] Doney, S. C., Ruckelshaus, M., Duffy, J. E., Barry, J. P., Chan, F., English, C. A., Galindo, H. M., Grebmeier, J. M., Hollowed, A. B., Knowlton, N., Polovina, J., Rabalais, N. N., Sydeman, W. J. and Talley, L. D. (2012) Climate change impacts on marine ecosystems. *Annual Review of Marine Science* 4(1):11-37
- [28] DSHIP Data Extraction, <https://dship.awi.de/dship-extraction/data>
- [29] Dowdeswell, J. A., Evans, J., Mugford, R., Griffiths, G., McPhail, S., Millard, N., Stevenson, P., Brandon, M. A., Banks, C., Heywood, K. J., Price, M. R., Dodd, P. A., Jenkins, A., Nicholls, K. W., Hayes, D., Abrahamsen, E. P., Tyler, P., Bett, B., Jones, D., Wadhams, P., Wilkinson, J. P., Stansfiels, K. and Ackley, S. (2008) Autonomous underwater vehicles (AVUs) and investigations of the ice-ocean interface: deploying the Autosub AUV in Antarctic and Arctic water. *Journal of Glaciology*, 54 (187):661-672

- [30] Eicken, H. and Lange, M. A. (1989) Development and properties of sea ice in the coastal regime of the southeastern Weddell Sea. *J. Geophys. Res.* 94(C6):8193-8206
- [31] Environment and Climate Change Canada (2016) www.ec.gc.ca
- [32] Etter, P. C. (2013) *Underwater Acoustic Modeling and Simulation*, Fourth Edition, CRC Press
- [33] Fossheim, M., Primicerio, R., Johannesen, E., Ingvaldsen, R. B., Aschan, M. M. and Dolgov, A. V. (2015) Recent warming leads to a rapid borealization of fish communities in the Arctic. *Nature Climate Change*
- [34] Francois, R. E., Garrison, G. R. and Wen, T. (1988) Reflectivity of sea ice. *The Journal of the Acoustical Society of America* 83:S1, S46-S47
- [35] Garrison, G. R. and Francois, R. E. (1988) Reflections from a block of sea ice. *The Journal of the Acoustical Society of America* 83, S46
- [36] German, C. R., Boetius, A., Whitcomb, L. L., Jakuba, M., Bailey, J., Judge, C., McFarland, C., Suman, S., Elliott, S., Katlein, C., Arndt, S., Bowen, A., Yoerger, D., Kinsey, J., Mayer, L. A., Nicolaus, M., Laney, S., Singh, H., Maksym, T. L., and Team, P. S. 86 *Scienti* (2014) First scientific dives of the Nereid Under Ice hybrid ROV in the Arctic Ocean. Fall Meeting, American Geophysical Union (AGU), San Francisco, CA
- [37] Grebmeier, J. K., Overland, J. E., Moore, S. E., Farley, E. V., Carmack, E. C., Cooper, L. W., Frey, K. E., Helle, J. H., McLaughlin, F. A. and McNutt, S. L. (2006) A major ecosystem shift in the northern Bering Sea. *Science* 311 (5766):1461-1464
- [38] Hendricks, S. (2009) Validierung von altimetrischen Meereisdickenmessungen mit einem helikopter-basierten elektromagnetischen Induktionsverfahren, PhD thesis, University Bremen
- [39] Ho, J. (2010) The implications of Arctic sea ice decline on shipping. *Marine Policy*, 34(3):713-715

- [40] Hunkeler, P., Hendricks, S., Hoppmann, M., Farquharson, C. G., Kalscheuer, T., Grab, M., Kaufmann, M. S., Rabenstein, L. and Gerdes, R. (2015) Improved 1D inversions for sea ice thickness and conductivity from electromagnetic induction data: Inclusion of nonlinearities caused by passive bucking. *Geophysics* 81(1)
- [41] Johnson, M. and Eicken, H. (2016) Estimating Arctic sea-ice freeze-up and break-up from the satellite record: A comparison of different approaches in the Chukchi and Beaufort Seas. *Elem. Sci. Anth.*, 4:124
- [42] Kaleschke, S., Girard-Ardhuin, F., Spreen, G., Beitsch, A. and Kern, S. ASI Algorithm SSMI-SSMIS sea ice concentration data, originally computed at and provided by IFREMER, Brest, France, were obtained as 5-day median-filtered and gap-filled product for [PERIOD] from the Integrated Climate Data Center (ICDC, icdc.cen.uni-hamburg.de/), University of Hamburg, Hamburg, Germany
- [43] Katlein, C., Schiller, M., Belter, H. J., Coppolaro, V., Wenslandt, D. and Nicolaus, M. (2017) A New Remotely Operated Sensor Platform for Interdisciplinary Observations under Sea Ice. *Front. Mar. Sci.* 4:281
- [44] Kohlbach, D., Graeve, M., A., Lange, B., David, C., Peeken, I. and Flores, H. (2016) The importance of ice algae-produced carbon in the central Arctic Ocean ecosystem: Food web relationships revealed by lipid and stable isotope analyses. *Limnology and Oceanography* 61(1)
- [45] Kovacs, A. (1997) Estimating the full-scale flexural and compressive strength of first-year sea ice. *J. Geophys. Res.*, 102(C4):8681-8689
- [46] Kwok, R. and Rothrock, D. A. (2009) Decline in Arctic sea ice thickness from submarine and ICESat records: 1958-2008. *Geophysical Research Letters*, 36
- [47] Kwok, R., Cunningham, G. F., Wensnahan, M., Rigor, I., Zwally, H. J. and Yi, D. (2009) Thinning and volume loss of the Arctic Ocean sea ice cover: 2003-2008. *J. Geophys. Res.*, 114

- [48] Kwok, R. and Untersteiner, N. (2011) The thinning of arctic sea ice. *Physics Today*:36-41
- [49] L-3 Communications SeaBeam Instruments (2000) Multibeam Sonar, Theory of Operation. Retrieved at: <https://www.scribd.com/document/153750093/Sea-Beam-Multi-Beam-Theory-Operation>
- [50] Lake, R. A. and Lewis, E. L. (1970) Salt rejection by sea ice during growth. *J. Geophys. Res.* 75(3):583-597
- [51] Langleben, M. P. (1970) Reflection of Sound at the Water-Sea Ice Interface. *Journal of Geophysical Research*, 75:5243-5246
- [52] Løset, S., Shkhinek, K. N., Gudmestad, O. T. Ove and Høyland, K. V., Actions from ice on arctic offshore and coastal structures, LAN (January 2006)
- [53] Lepparanta, M. (1993) A review of analytical models of sea-ice growth. *Atmosphere-Ocean*, 31(1):123-138
- [54] Liu, G. and Becker, A. (1990) Two-dimensional mapping of sea-ice keels with airborne electromagnetics. *Geophysics*, 55(2):239-248
- [55] Lucieer, V., Nau, A. W., Forrest, A. L. and Hawes, I. (2016) Fine-Scale Sea Ice Structure Characterized Using Underwater Acoustic Methods. *Remote Sensing* 8(821)
- [56] Lurton, X. (2002) *An Introduction to Underwater Acoustics: Principles and Applications*. Springer Science & Business Media
- [57] Lurton, X. (2016) Modelling of the sound field radiated by multibeam echosounders for acoustical impact assessment. *Applied Acoustics*, 101, 201-221
- [58] Makela, A., Witte, U. and Archambault, P. (2017) Ice algae versus phytoplankton: resource utilization by Arctic deep sea macroinfauna revealed through isotope labelling experiments, *Marine Ecology Progress series*, 572:1-18
- [59] Mayer, W. G. (1974) Determination of transverse wave velocity in transition layer of sea ice from reflection of water-borne sound. *J. Geophys. Res.* 79(6):885-886

- [60] Mazzoldi, P., Nigro, M. and Voci, C. (2007) *Fisica*. EdiSES, Volume 2, second edition, pp. 539-561
- [61] Medwin, H. and Clay, C. S. (1998) *Fundamentals of Acoustical Oceanography*. Academic Press
- [62] Meier, N., Hovelsrud, G. K., van Oort, B. E. H., Key, J. R., Kovacs, K. M., Michel, C., Haas, C., Granskog, M. A., Gerland, S., Perovich, D. K., Makshtas, A. and Reist, J. D. (2014) Arctic sea ice in transformation: A review of recent observed changes and impacts on biology and human activity. *Reviews of Geophysics* 52(3)
- [63] Melling, H., Johnston, P. H. and Riedel, D. A. (1995) Measurements of the underside topography of sea ice by moored subsea sonar. *J. Atmos. Oceanic Technol.*, 3:589-602
- [64] McCammon, D. and McDaniel, S. (1985) The influence of the physical properties of ice on reflectivity. *Journal of the Acoustical Society of America* 77(2):499-507
- [65] Nicolaus, M., Katlein, C., Maslanik, J. and Hendricks, S. (2012) Changes in Arctic sea ice result in increasing light transmittance and absorption. *Geophys. Res. Lett.*, 39
- [66] Nghiem, S.V., Clemente-Colon, P., Rigor, I. G., Hall, D. K. and Neumann, G. (2012) Sea floor control on sea ice. *Deep Sea Research II*, 77(80):52-61
- [67] Nummelin, A., Ilicak, M., Li, C., and Smedsrud, L. H. (2016), Consequences of future increased Arctic runoff on Arctic Ocean stratification, circulation, and sea ice cover. *J. Geophys. Res. Oceans*, 121:617-637
- [68] Pedersen, C. A., Roeckner, E., Luthje, M. and Winther, J (2009) A new sea ice albedo scheme including melt ponds for ECHAM5 general circulation model. *J. Geophys. Res.*, 114
- [69] Perovich, D. K., Richter-Menge, J. A., Jones, K. F. and Light, B. (2008) Sunlight, water, and ice: Extreme arctic sea ice melt during the summer of 2007. *Geophysical research letters*, 35

- [70] Peterson, I. K., Prinsenber, S. and Holladay, J. S. (2003) Sea-Ice Thickness Measurement: Recent Experiments using Helicopter-borne EM-Induction Sensors. *Recent Res. Devel. Geophysics* 5:1-20
- [71] Pfaffling, A., Haas, C. and Reid, J. E. (2007) A direct helicopter EM - sea-ice thickness inversion assessed with synthetic and field data. *Geophysics*, 72(4)
- [72] Polyakov, I., Pnyushkov, A. V., Alkire, M. B., Ashik, I. M., Baumann, T. M., Carmack, E. C., Goszczko, I., Guthrie, J., Ivanov, V. V., Kanzow, T., Krishfield, R., Kwok, R., Sundfjord, A., Morison, J., Rember, R. and Yulin, A. (2017) Greater role for Atlantic inflows on sea-ice loss in the Eurasian Basin of the Arctic Ocean. *Science* 356.6335:285-291
- [73] Rajkumar, T. (2014) Single and Multibeam echo sounder. MBES Taicheng Report. Retrieved by: <https://www.slideshare.net/TaichengmongRajkumar/mbes-taicheng-report>
- [74] Reid, J., Pfaffling, A. and Vrbancich, J. (2006) Airborne electromagnetic footprints in 1D earths. *Geophysics* 71(2):G63-G72
- [75] Rothrock, D.A., Yu, Y. and Maykut, G. A. (1999) Thinning of the Arctic sea-ice cover. *Geophysical Research Letters* 26(23):3469-3472
- [76] Rudels, B., Anderson, L. G. and Jones, E. P. (1996), Formation and evolution of the surface mixed layer and halocline of the Arctic Ocean. *J. Geophys. Res.*, 101(C4):8807-8821
- [77] Sandven, S., Kloster, K., Sagen, H., Alexandrov, V., Gerland, S., Hall, R., Forsberg, R. and Haas, C. (2005) Sea ice thickness and freeboard as function of snow and ice properties. CRYOSAT Workshop 8-10 March 2005
- [78] Schwartz, M., Reflection, Transmission and Impedance, Lecture 9. Lecture notes retrieved by: <https://users.physics.harvard.edu/~schwartz/15cFiles/Lecture9-Impedance.pdf>

- [79] Serreze, M.C. and Barry, R.G. (2011) Processes and Impacts of Arctic Amplification: A Research Synthesis. *Global and Planetary Change*, 77:85-96
- [80] Shokr, M. and Barber, D. G. (1994) Temporal evolution of physical and dielectric properties of sea ice and snow during the early melt season: Observations from SIMS'90 experiment. *Journal of Glaciology*, 40(134):16-30
- [81] Shokr, M. and Sinha, N. (2015) *Sea ice: physics and remote sensing*. John Wiley and Sons
- [82] Sinha, N. K. and Nakawo, M. (1981) Growth of first-year sea ice, Eclipse Sound, Baffin Island, Canada. *Journal of Glaciology*, 27(96)
- [83] Smith, W. O. and Barber, D. G. (2007) *Polynyas: Windows to the World*. Elsevier Oceanography Series, Volume 74:1-458
- [84] Soreide, J., Leu, E., Berge, J., Graeve, M., and Falk-Petersen, S. (2010) Timing of blooms, algal food quality and *Calanus glacialis* reproduction and growth in a changing Arctic. *Global change biology*
- [85] Stanton, T. K., Jezek, K. C. and Gow, A. J. (1986) Acoustical reflection and scattering from the underside of laboratory grown sea ice: Measurements and predictions. *The Journal of the Acoustical Society of America* 80, 1486
- [86] Stefan, J. (1891) *Über die Theorie der Eisbildung: insbesondere über Eisbildung im Polarmeere*. *Ann. Phys.*, 3rd Ser. 42:269-286
- [87] Stroeve, J., Hamilton, L. C., Bitz, C., M. and Blanchard-Wrigglesworth, E. (2014) Predicting September sea ice: Ensemble skill of the SEARCH Sea Ice Outlook 2008-2013. *Geophys. Res. Lett.* 41:2411-2418
- [88] Stroeve, J. and Notz, D. (2015) Insights on past and future sea-ice evolution from combining observations and models. *Global and Planetary Change*
- [89] Stroeve, J., Jenouvrier, S., Garrett Campbell, G., Barbraud, C. and Delord, K. (2016) Mapping and assessing variability in the Antarctic marginal ice zone, pack ice and coastal polynyas in two

- sea ice algorithms with implications on breeding success of snow petrels. *The Cryosphere*, 10:1823-1843
- [90] Sullivan E.J. (2008) Active Sonar. In: Havelock D., Kuwano S., Vorlaender M. (eds) *Handbook of Signal Processing in Acoustics*. Springer, New York, NY
- [91] Taskjelle, T., Hudson, S. R., Granskog, M. A. and Hamre, B. (2017) Modelling radiative transfer through ponded first-year Arctic sea ice with a plane-parallel model. *The Cryosphere*, 11: 2137-2148
- [92] Thomas, D. N. and Dieckmann, G. S. (2010) *Sea Ice*, second edition. Wiley-Blackwell
- [93] Tilling, R.L., Ridout, A. and Shepherd, A. (2017) Estimating Arctic sea ice thickness and volume using CryoSat-2 radar altimeter data. *Adv. Space Res.*
- [94] Twersky, V. (1957) On Scattering and Reflection of Sound by Rough Surfaces. *View Affiliations The Journal of the Acoustical Society of America* 29(2):209-225
- [95] Tokinagaa, H., Xie, S. and Mukougawa, H. (2017) Early 20th-century Arctic warming intensified by Pacific and Atlantic multi-decadal variability. *Proceedings of the National Academy of Sciences*, 201615880
- [96] Vilming, S. (1998) The development of the multibeam echosounder: An historical account. *J. Acoust. Soc. Am.*
- [97] Wadhams, P. (2000) *Ice in the ocean*. London: Gordon and Breach Science
- [98] Wadhams, P. and Comiso, J. C. (1992) The Ice Thickness Distribution Inferred Using Remote Sensing Techniques, *Microwave Remote Sensing of Sea Ice. Geophysical Monograph* 68:375-383. American Geophysical Union, Washington D.C.
- [99] Wadhams, P. and Doble, M. J. (2008) Digital terrain mapping of the underside of sea ice from a small AUV. *Geophys. Res. Lett.* 35, L01501

- [100] Wadhams, P., Wilkinson, J. and Mcphail, S. D. (2006) A new view of the underside of Arctic sea ice *Geophys. Res. Lett.* 33
- [101] Wainwright, H. M., Liljedahl, A. K., Dafflon, B., Ulrich, C., Peterson, J. E., Gusmeroli, A., and Hubbard, S. S. (2017) Mapping snow depth within a tundra ecosystem using multiscale observations and Bayesian methods, *The Cryosphere* 11.2 (857)
- [102] Wilkinson, J.P., Boyd, T., Hagen, B., Maksym, T., Pegau, S., Roman, C., Singh, H. and Zabilansky, L. (2015) Detection and quantification of oil under sea ice: The view from below, In *Cold Regions Science and Technology*, Volume 109
- [103] WMO Sea-Ice Nomenclature (2014) Volume I, JCOMM Expert Team on Sea Ice, 5th Session
- [104] Wong, G. S. K. (1995) Speed of sound in seawater as a function of salinity, temperature, and pressure. *The Journal of the Acoustical Society of America* 97, 1732

Acknowledgements

This thesis is the result of an amazing study experience that has been made possible thank to many people that I would like to thank.

First of all, my tutor Dr. Christian Katlein from AWI, for his help throughout the work, for the good discussions, and the many interesting things and tricks that he taught me. Thank you for the extra patience with someone who did not belong to the field, and for the opportunity to work together.

I am indebted to Dr. Marcel Nicolaus from AWI who, together with Christian, gave me the amazing opportunity to join them onboard Polarstern in the Arctic. I will never forget this experience and the amount of things that I have learned during the fieldwork. Thank you for giving me this chance.

I would like to thank Prof. Francesco Marin, who agreed to be my supervisor at the University of Florence. He gave me the chance to study abroad during my thesis internship and study period, hence making all this possible.

I am grateful to Dr. Thomas Krumpfen and Dr. Stefan Hendricks from AWI, for their help in my search for knowledge about the GEM. Thanks a lot.

I would like to extend my thanks to all the colleagues at AWI and in the Sea Ice Physics group, in particular to Louisa Tie-mann, Hannes Schulz, and Marco Zanatta. Great time with you guys, smashing high-level conversations, coffee breaks, and cake on the floor.

A big thank you to the crew, captains, chief scientists, and all

the nice scientists on PS105 and PS106 especially. Thanks for the nice time, the incredible adventure, and interesting conversations.

Thank you to the “bathymetry people”: Simon Dreutter, Patricia Slabon, and Amin Mardani. For your help, horseriding, good food, and laughs. Simon, thank you for all the patience on the first day: you made me understand and finally survive CARIS.

This whole experience would have never been possible without the support of my amazing family. My parents, Lucia and Rino, who always encouraged me to pursue my dreams, no matter how far I had to go. They taught me to believe in myself and to always be strong. Thank you for your constant love and trust. My sisters, Viola and Benedetta, more than sisters. For the crazy conversations while I was away, your constant support, and welcome back home. You gave me all the warmth I needed at the North Pole. To my niece Franci, who helped me studying by carefully scribbling four-year-old letters on my notes. I hope this work will inspire you one day. To my grandpa Rolando, who is going to ask lots of questions about this thesis work and, no matter what, be very proud of me. To Luke, who constantly helped me and cheered me up during the months in Germany and always. I could not have managed without your encouragement and love.

Appendix A

DT101 Specification sheet

**DT101**

445-091 AUGUST 2013-REVISED APRIL 2016

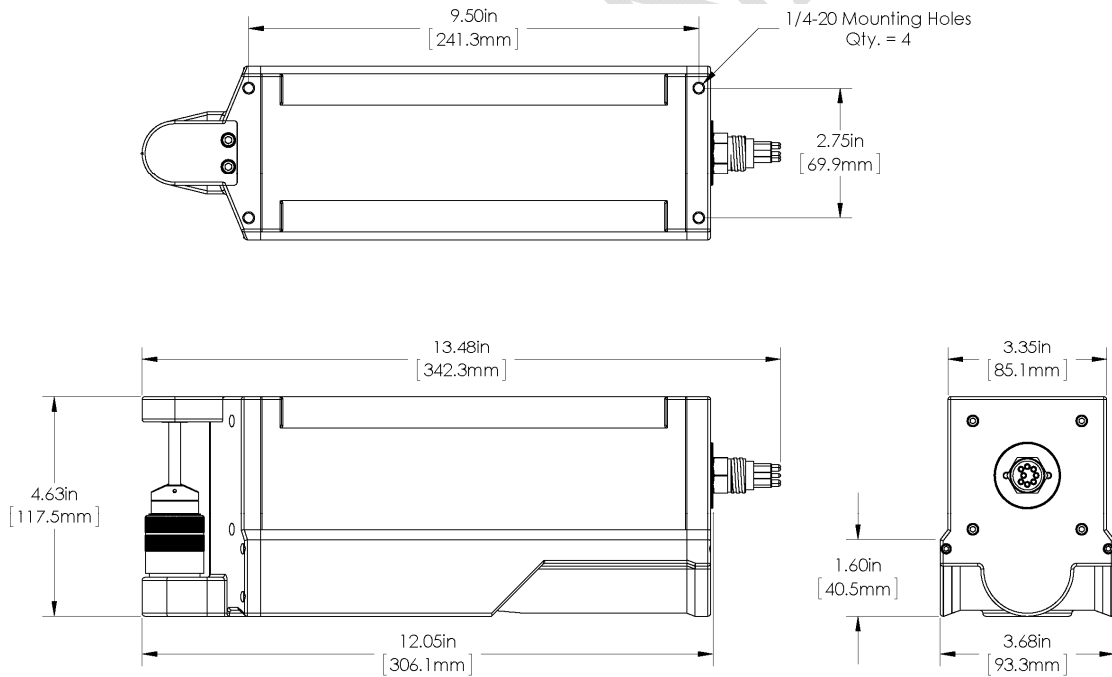
**IMAGENEX MODEL DT101
MULTIBEAM PROFILING SONAR
with Internally Integrated
Motion Reference Unit
& Sound Velocity Sensor**

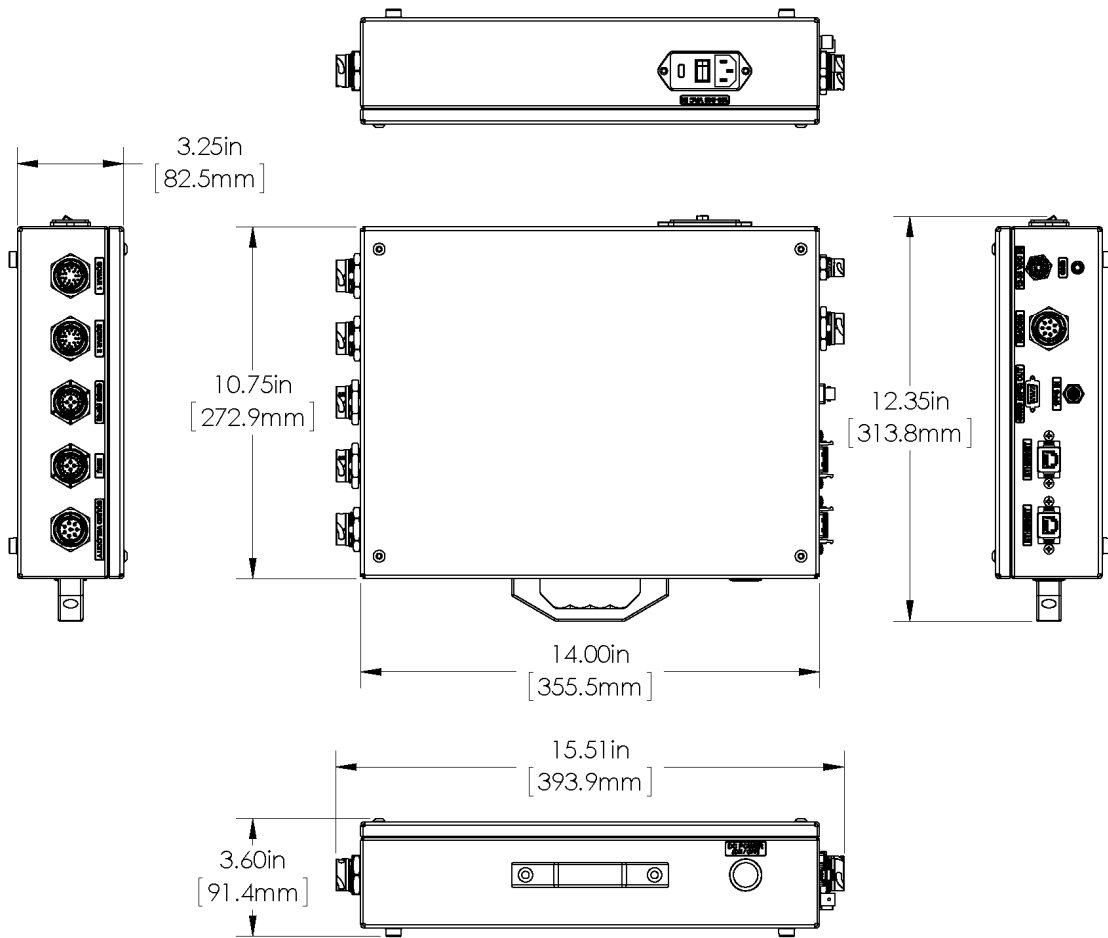


The new DT101 Multibeam Profiling Sonar (i.e. Multibeam Echo Sounder) is a single instrument integrating the sonar, motion reference unit (MRU), and sound velocity sensor into one sleek and compact unit. The DT101 requires only one cable for operating all three sensors and is a portable solution for any survey. Compatible with the DT100 SIR (Sensor Interface Relay) power supply/timing box, simply connecting a dual antenna GNSS/GPS receiver is all that is required to perform bathymetric surveys.

HARDWARE SPECIFICATIONS:	
FREQUENCY	240 kHz
SWATH WIDTH (nominal beam geometry)	Transmit: 120° x 3° Receive: 120° x 3°
EFFECTIVE BEAM WIDTHS	Narrow: 0.75° Medium: 1.5° Wide: 3°
NUMBER OF BEAMS	Default: 480 Selectable: 240, 120
RANGE RESOLUTION	0.02% of range
RANGE	75 m (246') water depth 150 m (492') slant range
MIN. DETECTABLE RANGE	0.5 m (1.6') below transducer
MOTION REFERENCE UNIT Pitch and Roll Accuracy: Heave:	Internally mounted OEM version of CDL MiniSense3 0.04° 5 cm or 5% (whichever is greater)
SOUND VELOCITY SENSOR	Internally mounted OEM version of AML Micro•X 1400 m/s to 1600 m/s +/- 0.025 m/s
MAX. OPERATING DEPTH (Submersion depth)	300 m (984') Contact Imagenex if a greater depth rating is required
INTERFACE TO PC	Ethernet (100 Mbps) using TCP/IP
MAX. CABLE LENGTH	100 m (328') on CAT5-e, longer cable runs possible with additional hardware
CONNECTOR	Underwater wet-mateable 8 conductor
POWER SUPPLY (sonar head only)	22 - 32 VDC at less than 15 Watts
DIMENSIONS	306 mm (12.05") L x 118 mm (4.63") H x 94 mm (3.68") W
WEIGHT: In Air	4.2 kg (9.5 lbs)
In Water	1.9 kg (4.2 lbs)
MATERIALS	Polyoxymethylene (i.e. Delrin), Titanium, PVC, Titanium connector
POWER SUPPLY/ TIMING BOX: DT100 Sensor Interface Relay (DT100 SIR)	2 port Ethernet switch (DT101 PC and Survey PC) Interfaces to: DT101 GNSS (GPS) Gyro / Heading Sensor 100 – 240 VAC or 12 – 36 VDC input range Dimensions: 394 mm (15.5") x 314 mm (12.4") x 92 mm (3.6")
MAX. PING RATE	20 Hz

SOFTWARE SPECIFICATIONS:	DT101_SIR.exe
WINDOWS™ OPERATING SYSTEM	Windows™ XP, Vista, 7, 8
DISPLAY MODES	Sector, Linear, Perspective, Profile, Beam Test
PERSISTENCE (TRAIL)	1 – 300 seconds
RANGE SCALES	5 m, 10 m, 20 m, 30 m, 40 m, 50 m, 60 m, 80 m, 100 m, 150 m, 200 m
SECTOR SIZES	30°, 60°, 90°, 120°
FILE FORMAT: RAW DATA PROFILE POINT	(filename).D1R (filename).D1P
RECOMMENDED MINIMUM COMPUTER REQUIREMENTS:	2 GHz Pentium 4 256 MB RAM 20 GB Hard Disk 1024 x 768 screen resolution





ORDERING INFORMATION:		
300 m UNIT	Standard	837B-000-442
Sensor Interface Relay box (DT100 SIR)	Standard	837-000-007
IP Address*	Option	-020

*Note: Standard IP Address is 192.168.0.2
 A different IP Address may be specified upon ordering.

Product and company names listed are trademarks or trade names of their respective companies.

Appendix B

CARIS Hips brief manual for sea ice draft measurements with DT101

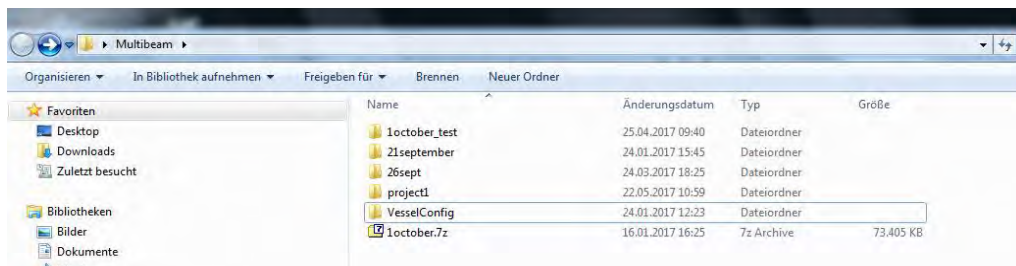
CARIS Hips brief manual
for sea ice draft measurements
with DT101

Veronica Coppolaro - Master student

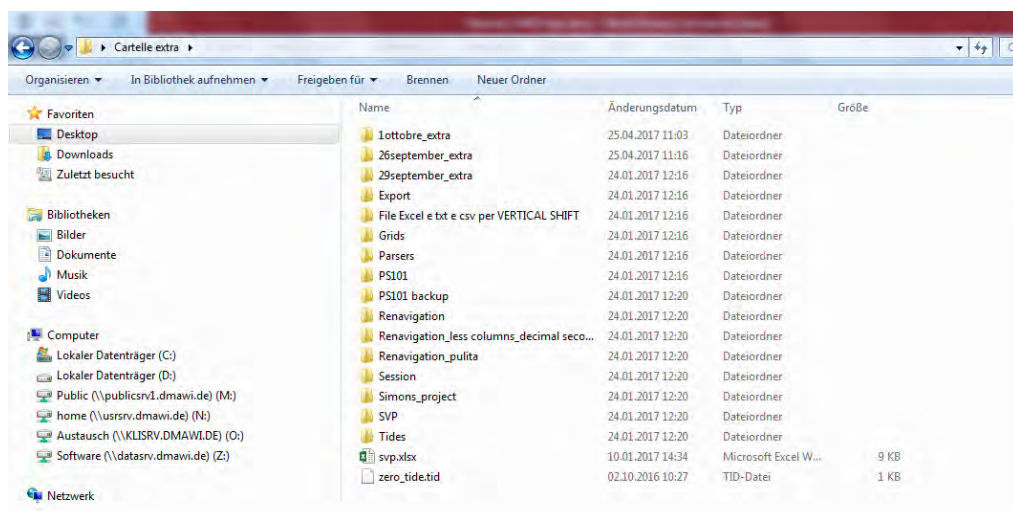
22.05.2017

1. Principal folder structure:

- One **main folder** with the Vessel file and one folder for each project

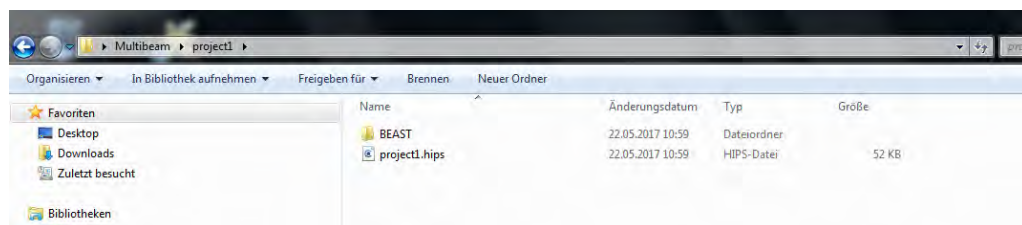


- One **extra folder** where to save Sessions, Surfaces and so on



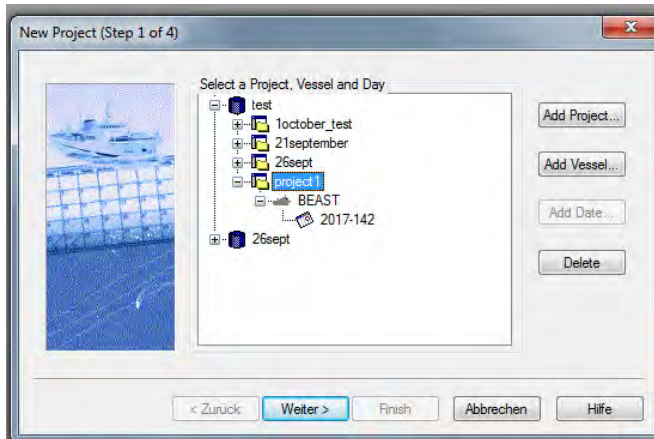
Project folder structure:

Every project must contain **ONLY** the folder with the lines of the project (that will be created during the building up of the project in CARIS) and the CARIS project (.hips file)



2. Create new project:

Open CARIS Hips -> File -> New -> Project



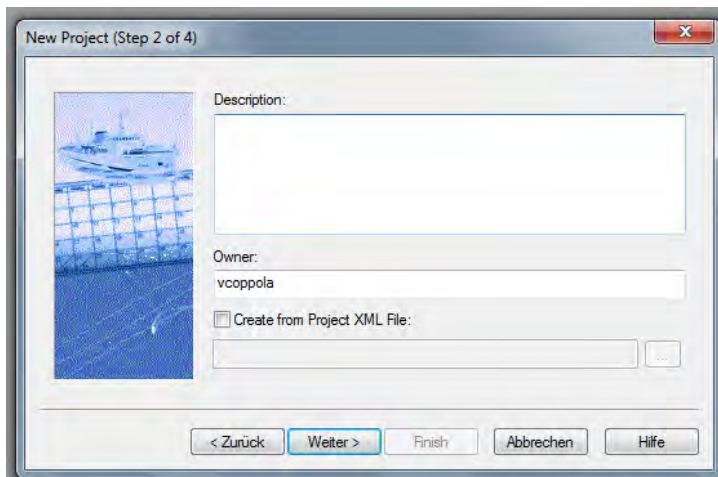
Choose a folder where to save the file

“Add project” -> i. e. “Project1” here

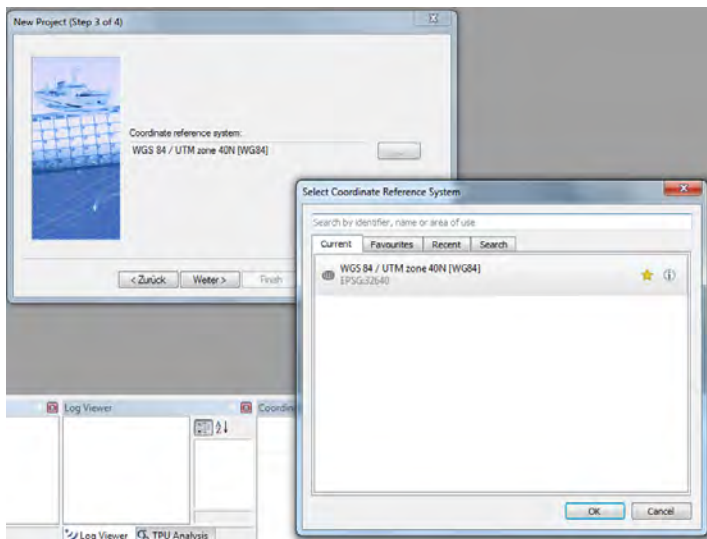
“Add vessel” -> BEAST

“Add date” -> 2017-142

If the project is linked to a set of data or a previous project, right click on the new project to be created and click on “**Connect to**”, then choose the folder with the project lines to be linked to.



Add a description if necessary



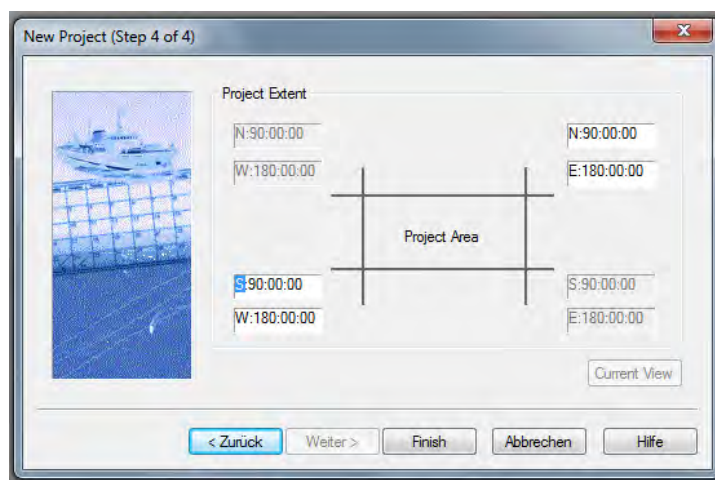
Choose the right **coordinate reference system**:

For PS101 (and probably for PS106 too) the choice is:

WGS 84 / UTM zone 40N

[WG84]

EPSG: 32640



Choose the **project extent** for the area of the survey:

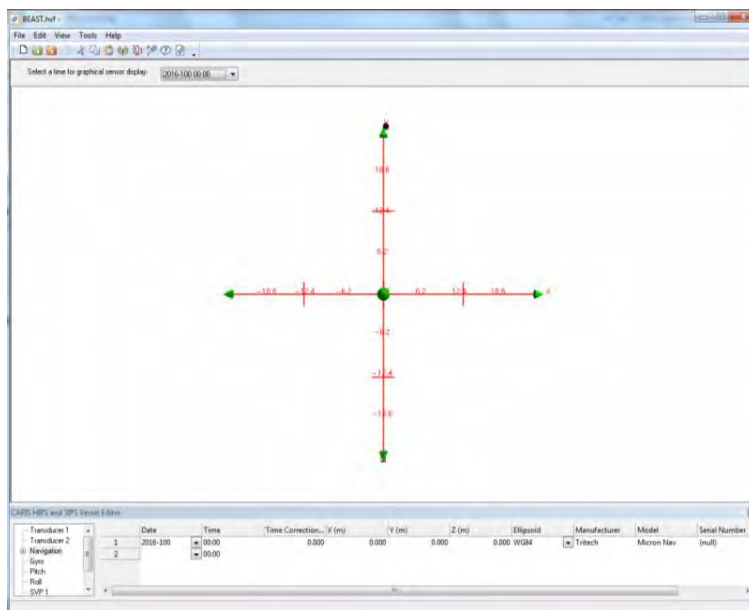
It can be left as it is found (here to the left) for a new project or limited to the area if the coordinates are well known.

If some areas of the survey want to be excluded, the project extent can be changed.

3. Vessel file:

The vessel file must contain all the offsets for the sensors involved in the survey.

To read and modify the Vessel file, open CARIS -> Tools -> Editors -> Vessel editor



Our vessel file contains: gyro, pitch, roll and svp.

Every sensor has to be switched on setting the tab "Apply" -> YES.

In our case the offsets are set as zero.

There is no heave offset, as no heave sensor is used.

For the Navigation the Ellipsoid has to be chosen: i.e. here it is the WG84

If a sound velocity profile is going to be used during PS106 the Vessel file must be modified: the parameters in "SVP1" and "SVP2" must be updated to the new values.

NOTE: At this point the project has been created: it can be opened and the Vessel file can be checked but no data are present.

The project is empty though, only the environment where to insert the data has been created.

4. Import raw data

The project is ready but empty: raw data must be imported to recreate the lines of the survey

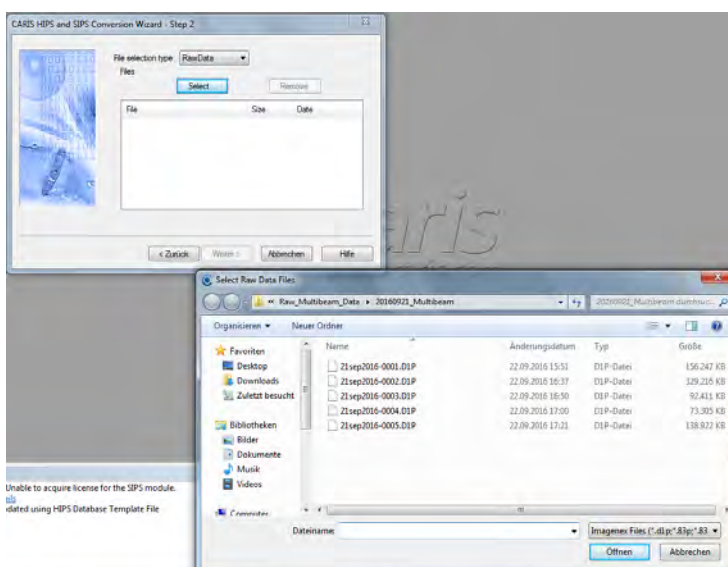


To import the raw data from DT101 first open the project in CARIS, then:

File -> Import -> Conversion Wizard



Set the **Format** for the raw data collected by DT101: Imagenex

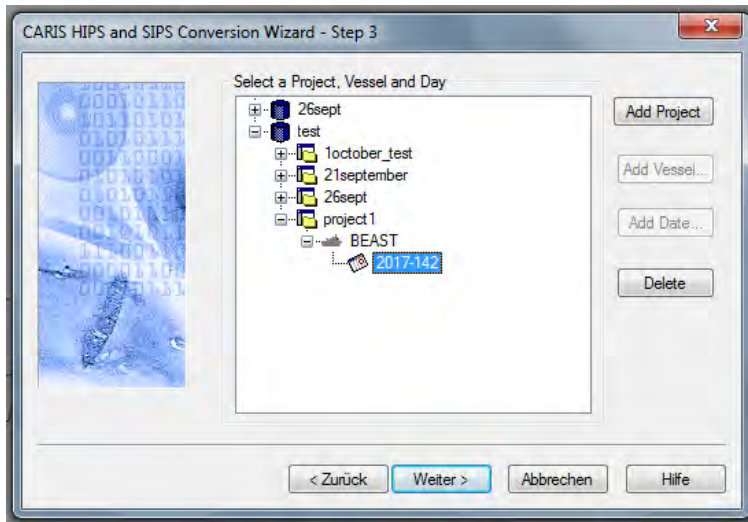


Select the File Type -> **Raw Data**

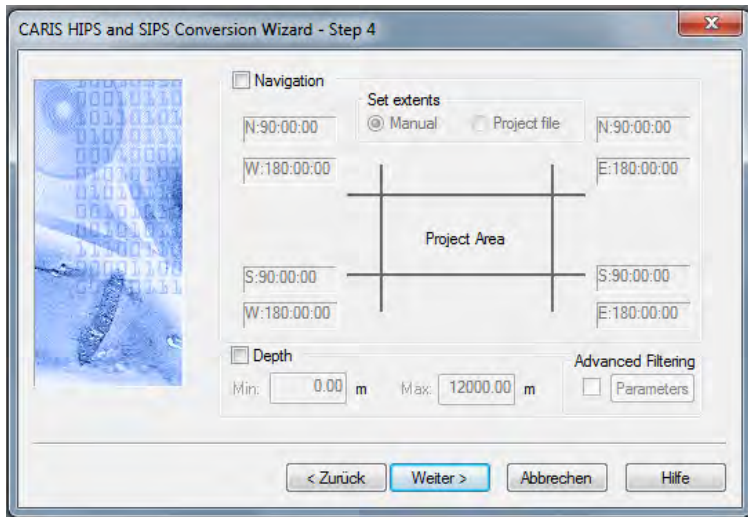
Now select the files to import from the folder where they are stored.

The extension of the files is **.D1P**

I prefer to have a folder that contains all the raw data from the surveys in a handy position, so that it is easier to find the files when importing with the Wizard (i.e. "Raw_Multibeam_Data")



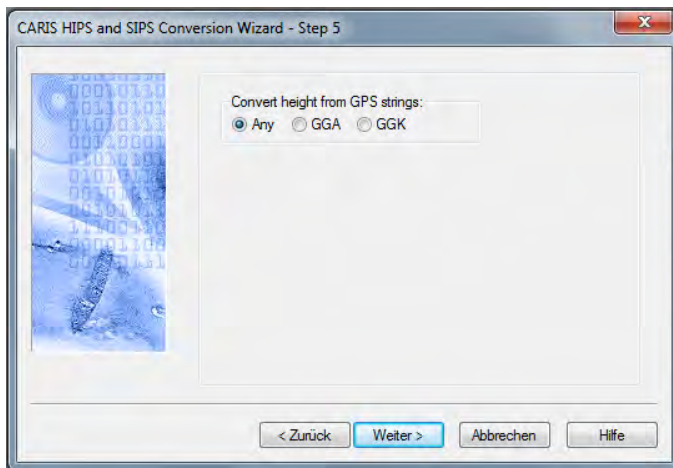
Choose the root: select the Project, Vessel and Day where to add the lines of raw data.



If necessary, add some filters

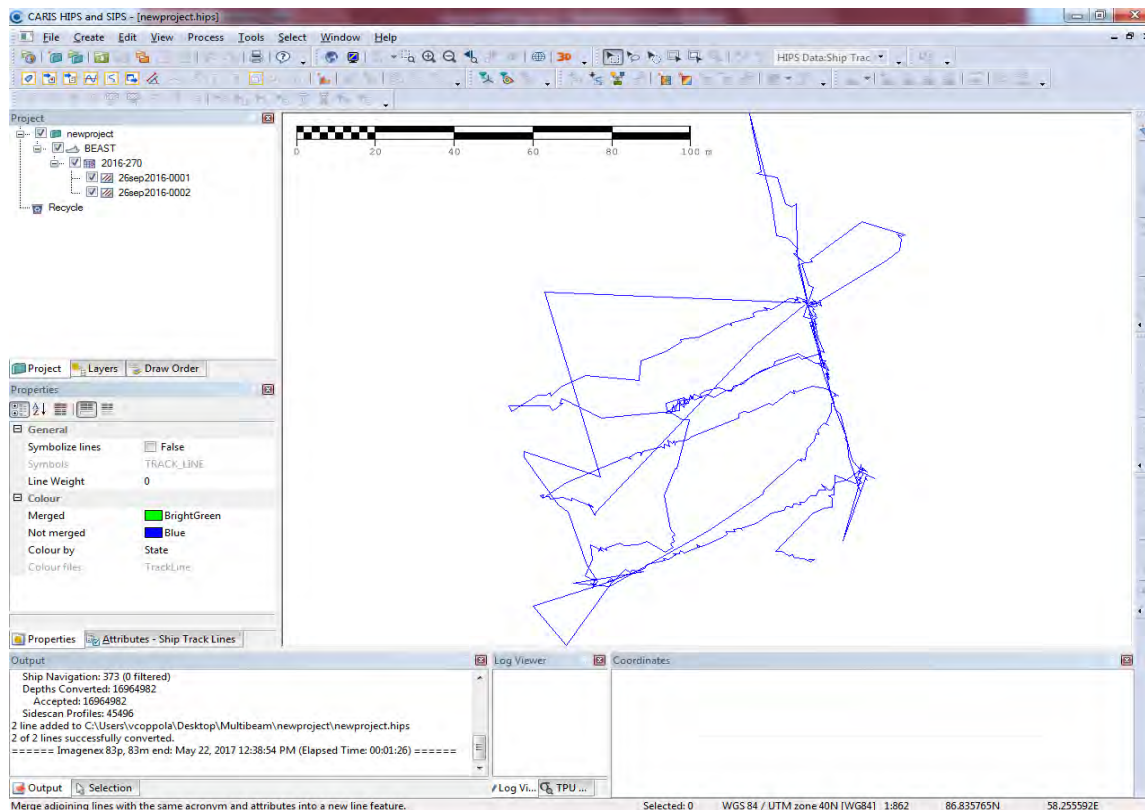
“Navigation” extent filtering is useful if some parts of a line of the survey have to be excluded

“Depth” filtering is also useful to avoid outliers in the surface



GPS should be set to “Any”

Now click on Convert and wait for the lines of the survey to be processed.



Open the project created.

In the left part of the screen the imported raw data will appear as **lines** listed under the day of the project: i.e. **26sep2016-0001**.

Every line can be shown separately simply by unticking the other lines.

When selecting the whole day, all the lines will be automatically selected.

Blue lines are “raw lines”, while green lines are lines that have been modified and the changes have been saved by merging them with the “Merge” tool (see following).

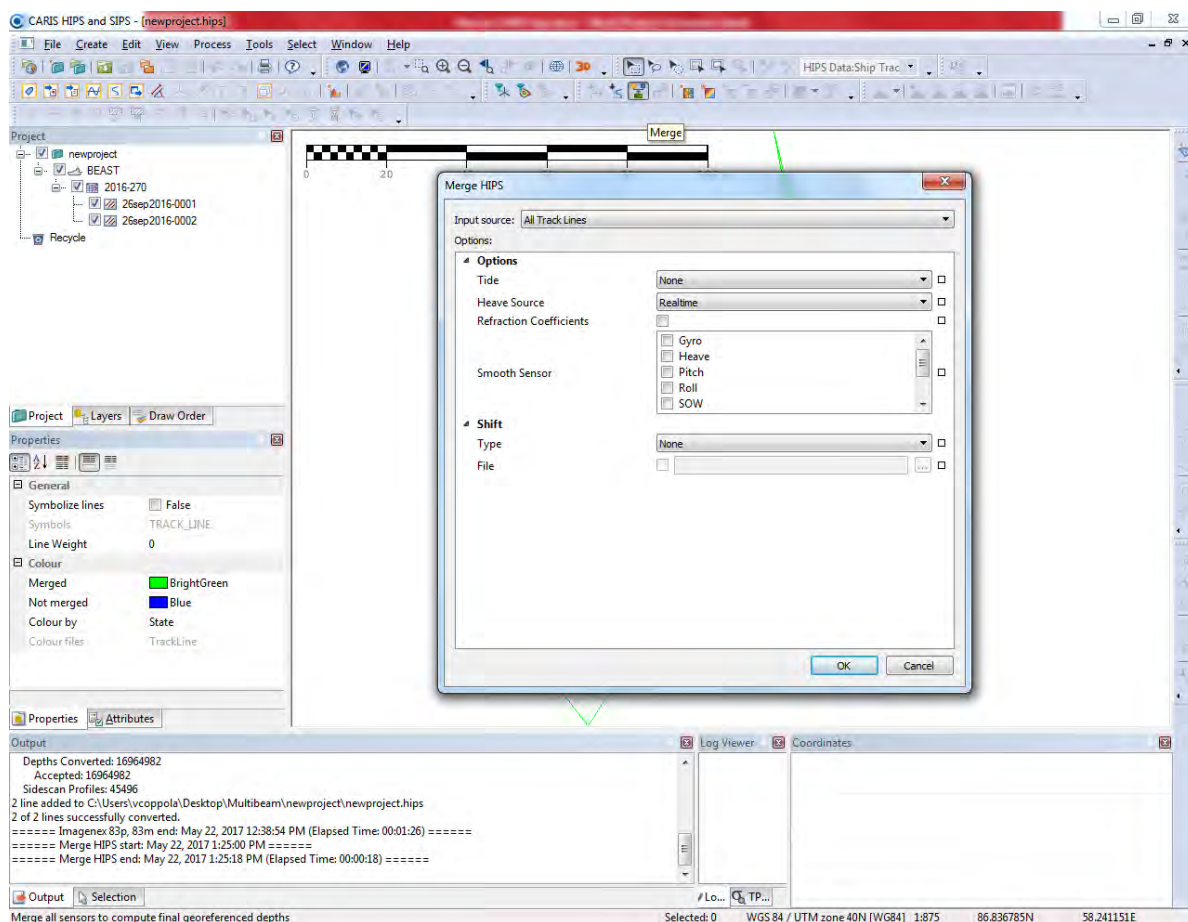
5. Merge

The Merge function in CARIS Hips allows to apply a change to the selected lines and save the change.

Merging must be applied after every modification to the lines, after applying Tide, Sound Velocity Profiles, after cleaning the data with the Editors and so on.

To merge click on the icon shown in figure or click on: Process -> Merge

For the first merge choose no tide: Process -> Merge -> Tide -> None

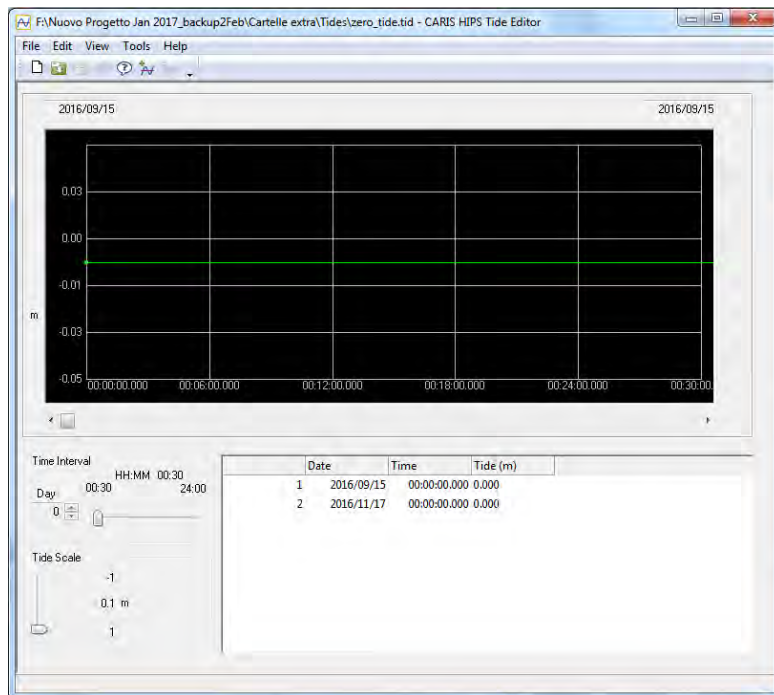


After merging all the previous changes will be saved and there is no direct, easy way to go back.

Merging the same change several times is strongly not recommended.

6. Tide

At the beginning of the data handling, a zero tide should be imported and applied to every line.

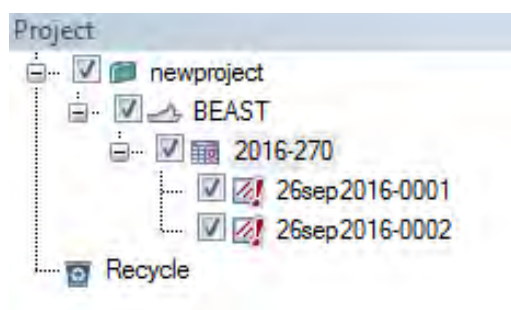


A **zero_tide.tid** file must be created, specifying the temporal extent of this fictional zero tide.

To create a tide file:

Tools -> Editors -> Tide

Apply the tide file or create a new one.



Remember to merge after every tide change.

A red exclamation mark will appear next to the lines on which you are working to remind you of the need for merging.

NOTE: Always empty the Recycle bin. Lines or parts of the project in the bin can disturb the processing.

7. Import Renavigation Data

Renavigation data must be imported in the project to allow for the SPOT.ON software recalculation and interpolation of the raw data.

File -> Import -> Generic Data Parser (GDP)

- Open the survey raw data in the **Renavigation folder**: File -> Open Raw Data
- Create a new (File -> New) or use an old parser (File -> Open) (parsers should be saved in a specific folder inside the “Extra Folder”)
- Run the parser

File Header	SpotOnTime	Latitude[°]	Longitude[°]	X_Position[m]	Y_Position[m]	Depth diff (m)	Roll[°]	Pitch[°]	USBL-COG	Ma	
Time Stamps	2016-09-24T06:1116.608	86.835662	88.242966	0.013702	0.014709	1.12	4.800000	-2.800000	41.955633	14.014830	0.312004
Sound Velocity	2016-09-24T06:1116.974	86.835662	88.242966	0.023957	0.031933	1.12	5.100000	-2.900000	41.818093	13.981213	0.473005
Depth	2016-09-24T06:1117.36	86.835662	88.242971	0.048946	0.050119	1.12	5.400000	-2.800000	41.049281	13.918056	0.556998
Navigation	2016-09-24T06:1118.018	86.835663	88.242978	0.073038	0.088883	1.12	5.400000	-2.900000	40.248317	13.804088	0.096006
Gyro	2016-09-24T06:1118.514	86.835663	88.242978	0.093265	0.104948	1.12	5.700000	-2.900000	39.543355	13.789728	0.586999
Heave	2016-09-24T06:1119.004	86.835663	88.242981	0.105662	0.113140	1.12	5.600000	-2.900000	39.330667	13.842032	0.910003
Pitch	2016-09-24T06:1119.695	86.835663	88.242982	0.112591	0.127445	1.12	5.300000	-2.900000	38.717430	13.802335	1.084999
Roll	2016-09-24T06:1119.987	86.835663	88.242988	0.149252	0.172927	1.12	4.800000	-3.000000	36.932874	14.282355	2.049999
Tide	2016-09-24T06:1120.153	86.835663	88.242989	0.156151	0.181835	1.12	4.600000	-3.000000	36.838907	14.354509	2.236007
Event	2016-09-24T06:1120.41	86.835664	88.242991	0.172880	0.203789	1.12	4.800000	-3.000000	35.765664	14.444998	2.693005
Data Depth	2016-09-24T06:1121.189	86.835664	88.242995	0.193490	0.231846	1.12	4.400000	-2.900000	34.622267	14.274114	2.634003
GPS Height	2016-09-24T06:1121.708	86.835664	88.242998	0.213885	0.251223	1.12	4.300000	-2.700000	33.477474	13.889186	2.116997
GPS Tide	2016-09-24T06:1121.879	86.835664	88.242999	0.217246	0.261649	1.12	4.200000	-2.600000	33.075348	13.749993	1.944005
Speed On Water	2016-09-24T06:1122.183	86.835664	88.243000	0.227471	0.280754	1.12	4.300000	-2.600000	32.351001	13.531704	1.640003
SSS Cable Out	2016-09-24T06:1122.833	86.835665	88.243003	0.241374	0.301944	1.12	4.400000	-2.600000	31.317495	13.310757	1.217998
SSS Gyro	2016-09-24T06:1123.931	86.835665	88.243004	0.251926	0.318604	1.12	4.800000	-2.600000	30.498517	13.189559	0.891999
SSS Navigation	2016-09-24T06:1123.833	86.835665	88.243008	0.246676	0.333450	1.12	4.700000	-2.600000	29.473223	13.076209	0.492001
SSS Sensor Height	2016-09-24T06:1124.257	86.835665	88.243009	0.280343	0.364249	1.12	4.800000	-2.500000	28.179587	12.951008	0.009998
SSS Sensor Depth	2016-09-24T06:1124.839	86.835666	88.243011	0.291371	0.389242	1.12	4.800000	-2.300000	27.138293	12.840290	0.434005
Surface Sound Speed	2016-09-24T06:1125.368	86.835666	88.243014	0.310016	0.421164	1.02	5.000000	-2.100000	25.990583	12.660782	0.337997
	2016-09-24T06:1125.368	86.835666	88.243016	0.324789	0.450745	1.12	5.100000	-2.100000	25.304656	12.461369	0.008992
	2016-09-24T06:1125.546	86.835666	88.243017	0.330100	0.461715	1.02	5.200000	-2.000000	25.179396	12.370763	0.183000
	2016-09-24T06:1125.743	86.835666	88.243018	0.335163	0.472313	1.02	5.300000	-1.900000	25.112259	12.339657	0.364001
	2016-09-24T06:1126.165	86.835666	88.243020	0.346892	0.497237	1.02	5.200000	-1.900000	25.138096	12.203947	0.787000
	2016-09-24T06:1126.626	86.835667	88.243022	0.360184	0.523460	1.02	5.200000	-1.900000	25.346835	12.033212	0.316997
	2016-09-24T06:1126.921	86.835667	88.243023	0.368387	0.543176	1.12	5.100000	-1.900000	25.490006	11.893190	0.031000
	2016-09-24T06:1127.385	86.835667	88.243023	0.381462	0.570746	1.12	4.900000	-1.900000	25.746892	11.663398	0.413003
	2016-09-24T06:1127.859	86.835667	88.243028	0.398302	0.603952	1.12	4.800000	-2.000000	26.446700	11.500818	0.737001
	2016-09-24T06:1128.299	86.835667	88.243030	0.409990	0.630138	1.12	4.700000	-2.100000	27.343993	11.523189	0.297001
	2016-09-24T06:1128.533	86.835668	88.243031	0.417372	0.645178	1.12	4.700000	-2.200000	28.228830	11.589123	0.064997
	2016-09-24T06:1128.97	86.835668	88.243034	0.431825	0.673460	1.12	4.800000	-2.200000	29.463742	11.775006	0.373997
	2016-09-24T06:1129.332	86.835668	88.243036	0.444314	0.696568	1.12	4.800000	-2.300000	30.239997	11.964058	0.736005
	2016-09-24T06:1129.713	86.835668	88.243038	0.457974	0.722704	1.12	4.800000	-2.400000	30.830210	12.132015	1.117003
	2016-09-24T06:1130.03	86.835669	88.243042	0.478800	0.757794	1.12	4.800000	-2.700000	31.852660	12.464007	1.704004
	2016-09-24T06:1130.701	86.835669	88.243044	0.495120	0.781198	1.12	4.800000	-2.800000	32.048978	12.448318	2.104998
	2016-09-24T06:1131.152	86.835669	88.243047	0.512725	0.813812	1.12	4.900000	-2.700000	32.460893	12.739816	2.586001
	2016-09-24T06:1131.588	86.835669	88.243050	0.528910	0.837570	1.12	4.900000	-2.700000	33.061999	12.606975	2.862004
	2016-09-24T06:1131.772	86.835669	88.243051	0.537646	0.851139	1.12	4.900000	-2.700000	33.282215	12.474357	3.060002
	2016-09-24T06:1132.111	86.835670	88.243053	0.551446	0.872462	1.12	4.900000	-2.600000	33.607049	12.230642	2.721007
	2016-09-24T06:1132.52	86.835670	88.243056	0.564948	0.895446	1.12	4.800000	-2.500000	33.938135	11.988443	2.312007
	2016-09-24T06:1132.943	86.835670	88.243059	0.586217	0.922228	1.12	4.800000	-2.500000	34.312227	11.894745	1.891008
	2016-09-24T06:1133.307	86.835670	88.243061	0.601853	0.948430	1.12	4.800000	-2.500000	34.409832	11.892932	1.825007
	2016-09-24T06:1133.715	86.835671	88.243064	0.619453	0.974305	1.12	4.800000	-2.400000	34.602962	11.897883	1.117003
	2016-09-24T06:1134.136	86.835671	88.243068	0.640385	1.004818	1.12	4.800000	-2.300000	34.607211	11.890249	0.636005
	2016-09-24T06:1134.672	86.835671	88.243071	0.661249	1.034985	1.12	4.900000	-2.200000	34.461975	11.802826	0.160007
	2016-09-24T06:1134.918	86.835671	88.243073	0.672076	1.055531	1.12	5.100000	-2.100000	35.014214	11.803014	0.089998
	2016-09-24T06:1135.412	86.835672	88.243074	0.693914	1.081797	1.12	5.300000	-2.100000	35.006631	11.826311	0.880001
	2016-09-24T06:1135.846	86.835672	88.243080	0.713247	1.109351	1.12	5.500000	-2.000000	34.930835	11.762750	0.542996
	2016-09-24T06:1136.136	86.835672	88.243082	0.724262	1.132783	1.02	5.600000	-2.000000	34.776740	11.800716	0.292994

NOTE: The text sheet in the Renavigation folder has to be modified before it can be used in the GDP!

- Delete rows containing NaN.
- Check that the **time stamps** are correct and match between SPOT.ON and HIPS. The data parsers that I have used and that I show below take already into account a time shift for this problem. As the time shift changes from station to station, either this time stamps problem has been solved before PS106 or every station has to be checked individually.
- Add the fix **time offset** between the SPOT.ON and CARIS Hips that varies for every survey.
- Rewrite the time stamps changing the seconds part from milliseconds to **decimal seconds**.
- If negative **time to ping** values occur, check the MatLab script first (it must have an absolute value for the time to ping calculation).
- Delete values of **gyro** that are not in the range between 0° and 360°.
- Delete **negative depth values**.
- Subtract an **offset** of around **20 cm** to the depth values to make up for the distance between the two sensors: multibeam sonar and pressure sensor.

File Header

File Header

File Date

Time Stamps

Sound Velocity

Depth

Navigation

Gyro

Heave

Pitch

Roll

Tide

Event

Delta Draft

GPS Height

GPS Tide

Speed On Water

SSS Cable Out

SSS Gyro

SSS Navigation

SSS Sensor Height

SSS Sensor Depth

Surface Sound Speed

File Header

Number of lines to skip

File date

File Header

File Date

Time Stamps

Sound Velocity

Depth

Navigation

Gyro

Heave

Pitch

Roll

Tide

Event

Delta Draft

GPS Height

GPS Tide

Speed On Water

SSS Cable Out

SSS Gyro

SSS Navigation

SSS Sensor Height

SSS Sensor Depth

Surface Sound Speed

Location

Line

Identifier

Name Start Position

Fields

	Start Position	Length
Year	<input type="text" value="1"/>	<input type="text" value="4"/>
Month	<input type="text" value="6"/>	<input type="text" value="2"/>
Day \.J-Day	<input type="text" value="9"/>	<input type="text" value="2"/>

Time stamps

File Header

File Date

Time Stamps

Sound Velocity

Depth

Navigation

Gyro

Heave

Pitch

Roll

Tide

Event

Delta Draft

GPS Height

GPS Tide

Speed On Water

SSS Cable Out

SSS Gyro

SSS Navigation

SSS Sensor Height

SSS Sensor Depth

Surface Sound Speed

Location

Free Form

Fixed Column Start Position

	Relative Position	Length
<input checked="" type="checkbox"/> Year	<input type="text" value="1"/>	<input type="text" value="4"/>
Month	<input type="text" value="6"/>	<input type="text" value="2"/>
Day \.J-Day	<input type="text" value="9"/>	<input type="text" value="2"/>
<input checked="" type="checkbox"/> Hour	<input type="text" value="12"/>	<input type="text" value="2"/>
<input checked="" type="checkbox"/> Minute	<input type="text" value="15"/>	<input type="text" value="2"/>
Seconds	<input type="text" value="18"/>	<input type="text" value="4"/>
	Multiplier	Offset
Seconds	<input type="text" value="1.000000"/>	<input type="text" value="15.000"/>

Sound Velocity

File Header

File Date

Time Stamps

Sound Velocity

Depth

Navigation

Gyro

Heave

Pitch

Roll

Tide

Event

Delta Draft

GPS Height

GPS Tide

Speed On Water

SSS Cable Out

SSS Gyro

SSS Navigation

SSS Sensor Height

SSS Sensor Depth

Surface Sound Speed

Location

Line

Identifier

Name Start Position

Default Velocity (m/s)

Location

Free Form

Field

Fixed Column

Start Position Length

Other

Multiplier Offset

Navigation- Latitude

File Header

File Date

Time Stamps

Sound Velocity

Depth

Navigation

Gyro

Heave

Pitch

Tide

Event

Delta Draft

GPS Height

GPS Tide

Speed On Water

SSS Cable Out

SSS Gyro

SSS Navigation

SSS Sensor Height

SSS Sensor Depth

Surface Sound Speed

Coordinates

Geographic Ground

Latitude Longitude

Location

Free Form

Fixed Column Start Position

	Relative Position	Length	Multiplier	Offset
Degrees	<input type="text" value="1"/>	<input type="text" value="9"/>	<input type="text" value="1.000000"/>	<input type="text" value="0.000"/>
<input type="checkbox"/> Min	<input type="text" value="0"/>	<input type="text" value="2"/>	<input type="text" value="1.000000"/>	<input type="text" value="0.000"/>
<input type="checkbox"/> Sec	<input type="text" value="0"/>	<input type="text" value="2"/>	<input type="text" value="1.000000"/>	<input type="text" value="0.000"/>
<input type="checkbox"/> Tag	<input type="text" value="0"/>			

Pseudo Time

Start (YYYY-DDD HH:MM:SS.SSS) Increment (sec)

Navigation- Longitude

File Header

File Date

Time Stamps

Sound Velocity

Depth

Navigation

Gyro

Heave

Pitch

Roll

Tide

Event

Delta Draft

GPS Height

GPS Tide

Speed On Water

SSS Cable Out

SSS Gyro

SSS Navigation

SSS Sensor Height

SSS Sensor Depth

Surface Sound Speed

Coordinates

Geographic Ground

Latitude Longitude

Location

Free Form

Fixed Column Start Position

	Relative Position	Length	Multiplier	Offset
Degrees	<input type="text" value="1"/>	<input type="text" value="9"/>	<input type="text" value="1.000000"/>	<input type="text" value="0.000"/>
<input type="checkbox"/> Min	<input type="text" value="0"/>	<input type="text" value="2"/>	<input type="text" value="1.000000"/>	<input type="text" value="0.000"/>
<input type="checkbox"/> Sec	<input type="text" value="0"/>	<input type="text" value="2"/>	<input type="text" value="1.000000"/>	<input type="text" value="0.000"/>
<input type="checkbox"/> Tag	<input type="text" value="0"/>			

Pseudo Time

Start (YYYY-DDD HH:MM:SS.SSS) Increment (sec)

Gyro

File Header
File Date
Time Stamps
Sound Velocity

- Depth
- Navigation
- Gyro
- Heave
- Pitch
- Roll
- Tide
- Event
- Delta Draft
- GPS Height
- GPS Tide
- Speed On Water
- SSS Cable Out
- SSS Gyro
- SSS Navigation
- SSS Sensor Height
- SSS Sensor Depth
- Surface Sound Speed

Identifier
Name Start Position

Location
 Free Form
Field
 Fixed Column
Start Position Length

Other
Multiplier Offset

Pitch

File Header
File Date
Time Stamps
Sound Velocity

- Depth
- Navigation
- Gyro
- Heave
- Pitch
- Roll
- Tide
- Event
- Delta Draft
- GPS Height
- GPS Tide
- Speed On Water
- SSS Cable Out
- SSS Gyro
- SSS Navigation
- SSS Sensor Height
- SSS Sensor Depth
- Surface Sound Speed

Identifier
Name Start Position

Location
 Free Form
Field
 Fixed Column
Start Position Length

Other
Multiplier Offset

Roll

File Edit View Tools Window Help

File Header
File Date
Time Stamps
Sound Velocity

- Depth
- Navigation
- Gyro
- Heave
- Pitch
- Roll
- Tide
- Event
- Delta Draft
- GPS Height
- GPS Tide
- Speed On Water
- SSS Cable Out
- SSS Gyro
- SSS Navigation
- SSS Sensor Height
- SSS Sensor Depth
- Surface Sound Speed

Identifier
Name Start Position

Location
 Free Form
Field
 Fixed Column
Start Position Length

Other
Multiplier Offset

GPS Height

File Edit View Tools Window Help

File Header
File Date
Time Stamps
Sound Velocity

- Depth
- Navigation
- Gyro
- Heave
- Pitch
- Roll
- Tide
- Event
- Delta Draft
- GPS Height
- GPS Tide
- Speed On Water
- SSS Cable Out
- SSS Gyro
- SSS Navigation
- SSS Sensor Height
- SSS Sensor Depth
- Surface Sound Speed

Identifier
Name Start Position

Location
 Free Form
Field
 Fixed Column
Start Position Length

Other
Multiplier Offset

GPS Tide

File Edit View Tools Window Help

File Header
File Date
Time Stamps
Sound Velocity

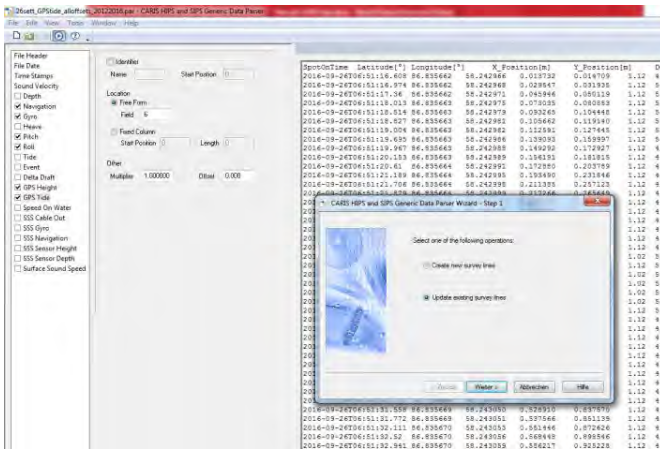
- Depth
- Navigation
- Gyro
- Heave
- Pitch
- Roll
- Tide
- Event
- Delta Draft
- GPS Height
- GPS Tide
- Speed On Water
- SSS Cable Out
- SSS Gyro
- SSS Navigation
- SSS Sensor Height
- SSS Sensor Depth
- Surface Sound Speed

Identifier
Name Start Position

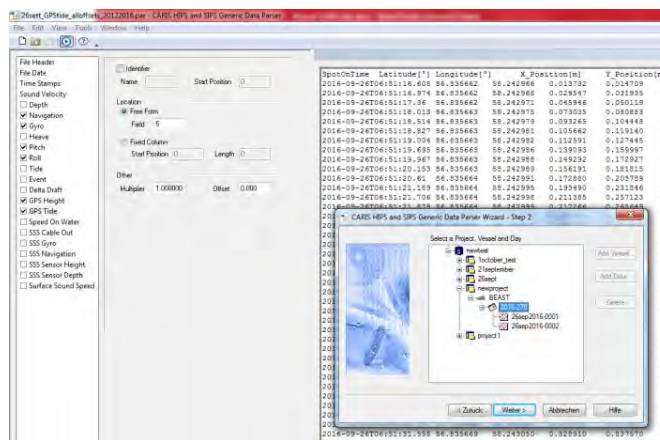
Location
 Free Form
Field
 Fixed Column
Start Position Length

Other
Multiplier Offset

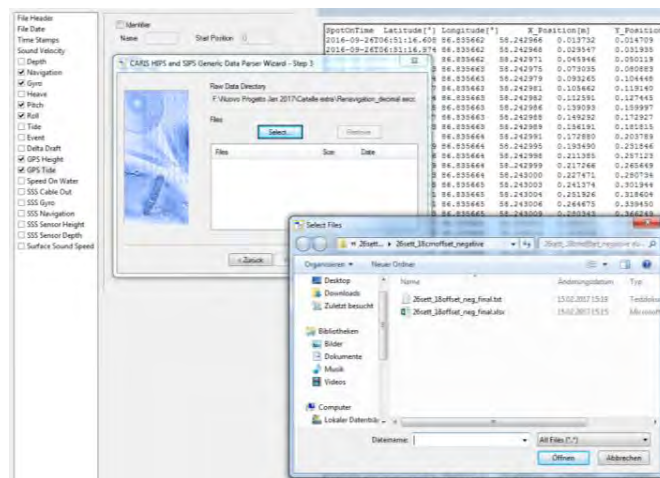
Running the GDP:



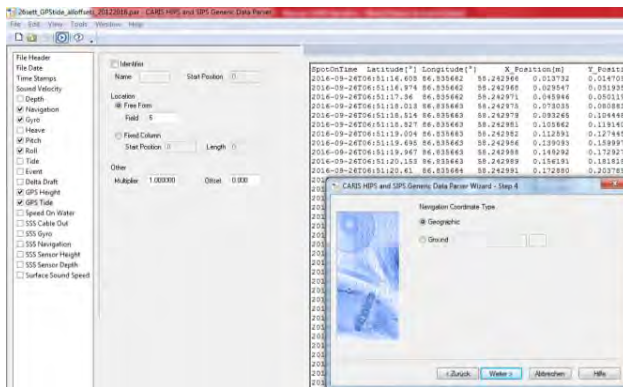
Choose the option: Update existing lines



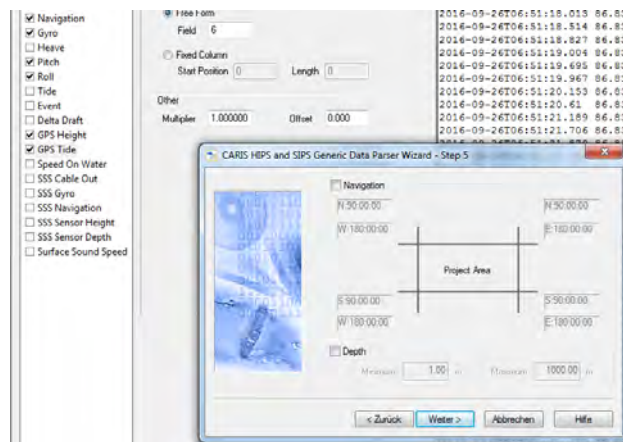
Select the lines to update or the whole day if you want to update every line in the survey



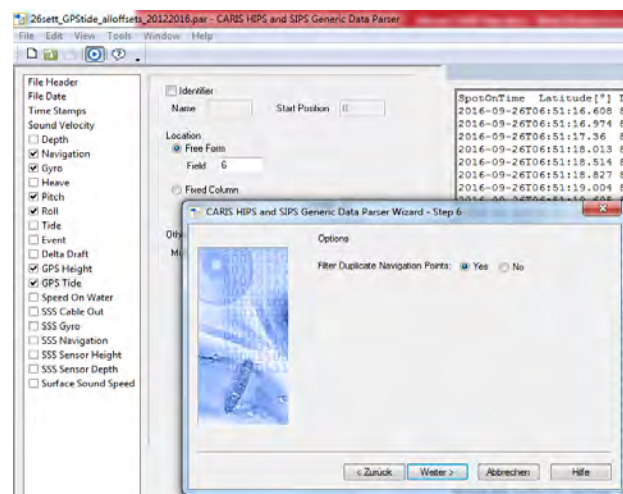
Select the raw data directory and files



Choose the **Navigation Coordinate Type**.
Geographic suits our purpose.



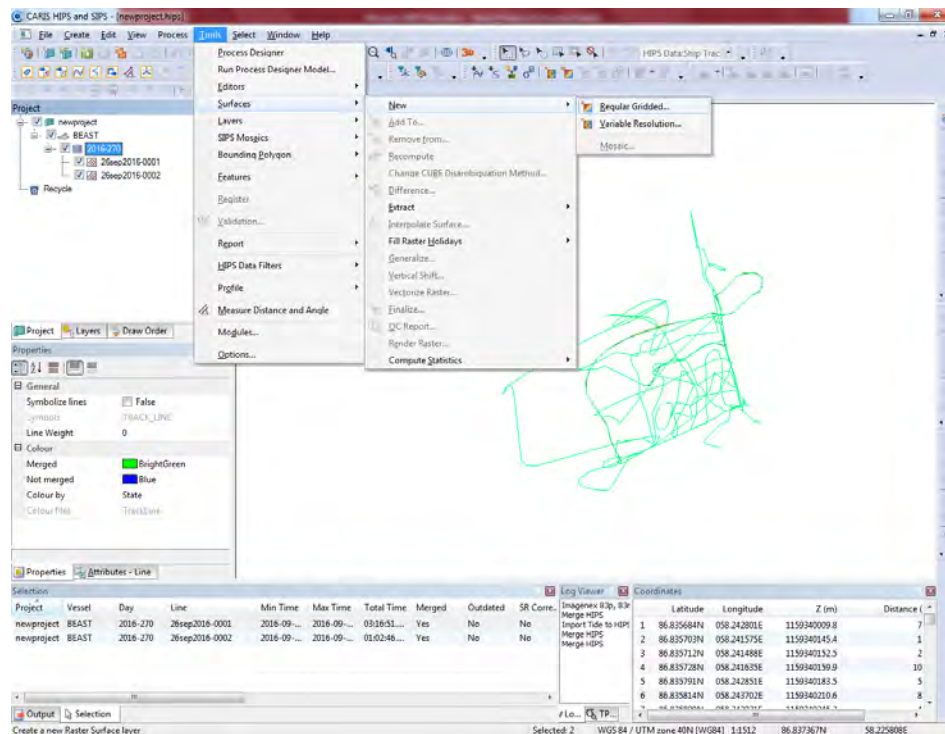
Navigation and Depth filters
can be applied if necessary.



Filter Duplicate Navigation Points: yes

Now **Convert** the data and check the results: a summary of Accepted and Rejected data is given after every conversion. Then simply close the GDP and merge the lines using Tide -> GPS

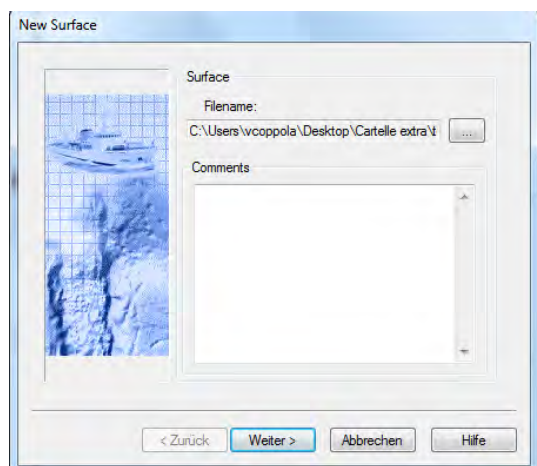
8. Create a surface



At this point the lines of the survey look different: they have been merged taking into account Tide and Renavigation.

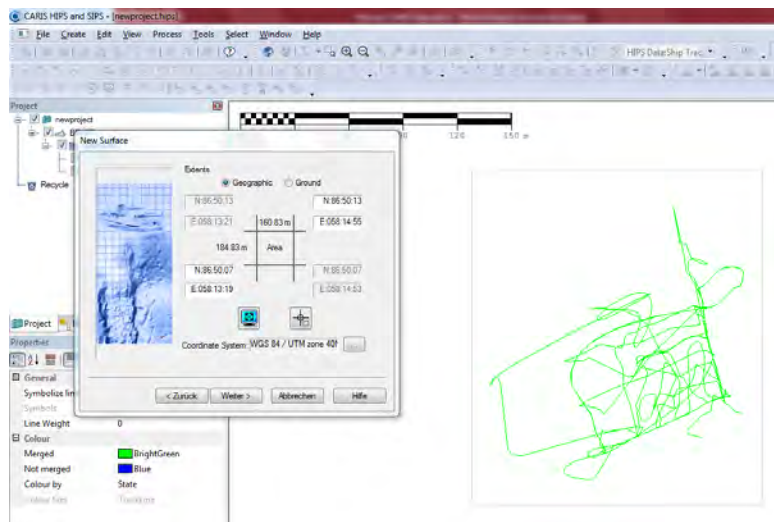
They are ready to be used to create a surface.

- First select the lines that you want to use, or the day in case the surface should cover every line
- Then select: Tools -> Surfaces -> New -> Regular Gridded



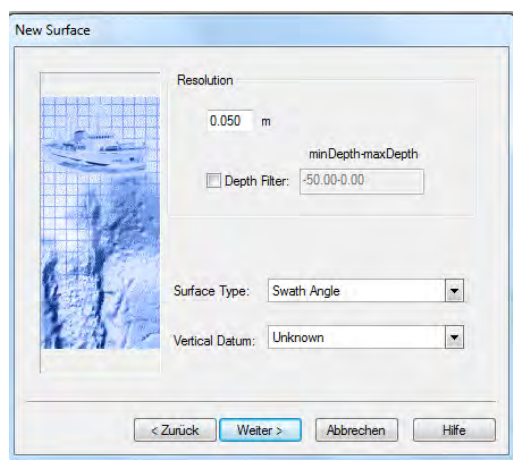
Name the Surface and save it in a folder.

I suggest to have a folder just for Surfaces for every survey. The folder should be collocated in the “Extra folder” and never in the “Main folder”, just like for Sessions, Tides and so on.



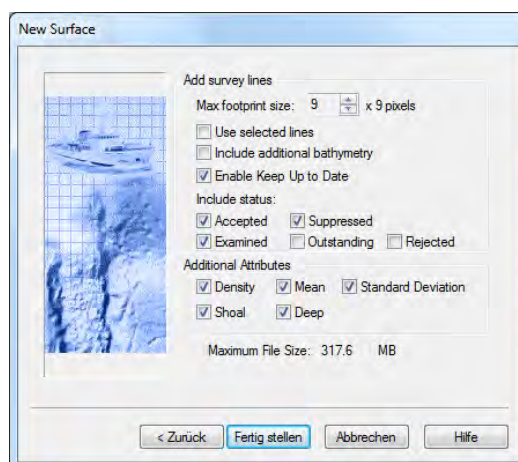
Choose the area **extent** for the surface.

This symbol allows to select a precise area around the survey.



The **resolution** can be set to 0.05 m.

A depth filter can also be used.



Other options can be changed at this stage.

Make sure the **Rejected status** is **not** ticked so that rejected data will not be included in the surface.

Click on Complete. Note that for surveys with a significant number of data this process can take **several minutes**.

9. Editors

Several editors can be used to clean the surface. Their use is well explained in the CARIS Support Guide.

A suggestion to improve the efficiency is to use these editors in temporal order:

- **Navigation editor**
- **Attitude editor**
- **Swath editor**
- **Subset editor**

10. Other suggestions

- ✓ Always save Parsers, Sessions and Surfaces at the end of the day. Make several copies that can be useful to go back to and work on, as some of the changes (i.e. the merge) are permanent.
- ✓ Save Parcels, Sessions and Surfaces in the "Extra Folder", never in the "Main Folder".
- ✓ If CARIS struggles to open a project, just start opening a surface instead.
- ✓ Always check the Log Viewer at the bottom of CARIS window to keep an eye on the processes and of any possible change that has taken place.

For any further doubt check CARIS Hips Documentation:

[Help](#) -> [User guide](#) -> [Reference guide](#)

Or contact me:

vero.coppolaro@gmail.com

Appendix C

Snow depth-sea ice thickness regression plots

